MODELLING OF AN OPERATIONAL TRANSCONDUCTANCE AMPLIFIER AND AN INVESTIGATION OF ITS USE AS AN INDUCTANCE SIMULATOR

Pietro Arella

A Thesis

in

The Faculty

of

Engineering

Presented in Partial Fulfillment of the Requirements
for the Degree of Master of Engineering at
Concordia University
Montreal, Canada

June, 1982

ABSTRACT

MODELLING OF AN OPERATIONAL TRANSCONDUCTANCE AMPLIFIER AND AN INVESTIGATION OF ITS USE AS AN INDUCTANCE SIMULATOR

PIETRO ARELLA

The operational transconductance amplifier (OTA) is an IC chip that has found applications in many analog electronic circuits, including RC-active filters. In fact, an OTA is as versatile as the popular operational amplifier (OA). While a frequency dependent model for the transfer gain of the OA is well-established, no such model exists for the OTA.

This thesis develops a frequency dependent model for the transfer gain of the 3080 OTA which is obtained through experimental data of its terminal-to terminal characteristics. While the model is derived specifically for the 3080 OTA, a similar method of development can be used for other types of OTAs.

The feasibility of simulating a grounded inductor using two OTAs and a single grounded capacitor is investigated by deriving and testing an equivalent circuit which takes into consideration the frequency dependent gains, the input and output impedances of the OTAs as well as the loss of the terminating capacitor. The results of the investigation show that inductances can be simulated over a wide range of values and over a wide frequency range. However, the practical ranges can be severely restricted by the limited dynamic range of the OTAs.

A scheme is proposed and verified experimentally to extend the dynamic range of the OTAs. Finally, an equivalent circuit is also presented for the inductor simulator circuit using the OTAs in the new scheme.

ACKNOWLEDGEMENTS

The author is deeply indebted to Dr. B.B. Bhattacharyya for having suggested this study, for his supervision throughout the preparation of this thesis and for the motivation that he has instilled into the author.

Thanks are due to Irene Christie for her excellent and patient typing of this manuscript.

The author wishes to dedicate this work to all the untold human sorrow, courage and heroism in the face of illnesses.

TABLE OF CONTENTS

PAGE

LIST OF FIGURES

LIST OF SYMBOLS

The following is a list of selected symbols and abbreviations appearing in this text.

Symbol	Definition	Page
OA	Operational Amplifier	1
OTA	Operational Transconductance Amplifier	1
G_m	Transconductance	3
I_{abc}	Bias current of the OTA (I_1, I_2, etc. also indicate bias currents of specific OTA units)	3
R_o	Output resistance of the OTA	4
R_ℓ	Load resistor	4
$A_{vo}(w)$	Open loop voltage gain	4
I_{om}	Maximum peak output current of the OTA	20
V_{om}	Maximum peak output voltage of the OTA	20
CF	Correcting Factor for $G_m(0)$	23
R_p, C_p	Parasitic resistive and capacitative components affecting the load impedance	28
K_o	DC gain of second order system	32
W_n	Natural frequency	33
σ	Damping constant	33
W_r	Critical frequency	34
CT1	Compensating term No. 1	37
CT2	Compensating term No. 2	38
R_i	Input impedance of the OTA	44
C, G_ℓ	Terminating capacitance and admittance of the inductor simulator	45
L_t	Theoretical inductance range	61
L_u	Useful inductance values	62
Q_u	Useful quality factor values	62
ID	Inductance percentage deviation	65

CHAPTER 1

INTRODUCTION

1.1 General

Operational Amplifiers are very common IC chips. Engineers have been using them extensively for innumerable applications and considerable literature is available on their characteristics. They are well known circuit elements.

On the other hand, the Operational Transconductance Amplifier (OTA), which arrived on the market in the early seventies, is somewhat unknown compared to its cousin, the Operational Amplifier (OA).

Little literature is available on the OTA from technical journals and the few textbooks which mention the OTA, basically reproduce in full or in part the technical literature available from the manufacturers [1] [2]. This is not to imply that the OTA has no practical use. The OTA presently finds applications where controllable gain is needed, as is often the case in audio and control engineering. Further fields of applications are modulators, frequency converters, analogue signal multipliers, multiplexers and sample-and-hold techniques, to name a few. However, little attention has been given to the role that the OTA could play in active filter design. Dr. T. Deliyannis [3] is, according to the writer, the most advanced designer in this area. He used the CA3060 OTA array in a number of active filter configurations.

Filters are circuit configurations which are used to obtain at their output a reshaping of the frequency content of an input signal. It is obvious that in order to design a frequency sensitive network, the designer needs to know accurately the frequency dependent characteristics

of each passive and active filter element of the design. Frequency dependent models of the filter elements must be established before a design is attempted. Extensive efforts have been given to the study of the frequency dependent OA models, however virtually no effort has been put in deriving similar models for the OTAs. This is perhaps the main reason which explains the little use of the OTA in active filter design.

For the CA3060 OTA array which Deliyannis [3] used in his work, RCA specifications provide some test data [4] from which, through analytical techniques, a model could be derived. On the other hand, no information is available to the designer who wishes to obtain a frequency dependent model of the 3080 OTA. In fact, neither National Semiconductors (LM3080), nor RCA (CA3080) have provided in their data sheets sufficient information which could allow the designer to find a frequency model of any of the two OTAs.

1.2 The OTA terminal to terminal model

The active filter designer is interested in the input to output characteristics of the active elements. This study which is intended to facilitate his future work will, therefore, concentrate on the terminal to terminal characteristics of the 3080 rather than on its internal circuitry. For a detailed description of the internal circuitry, the interested reader may look into reference [5]. Appendix I presents the circuit configuration of the National Semiconductors unit LM3080N which is the equivalent of the RCA unit CA3080. Pin designations are identical for the two OTAs.

Figure 1, shown below, is the model of the OTA as presented by RCA [1].

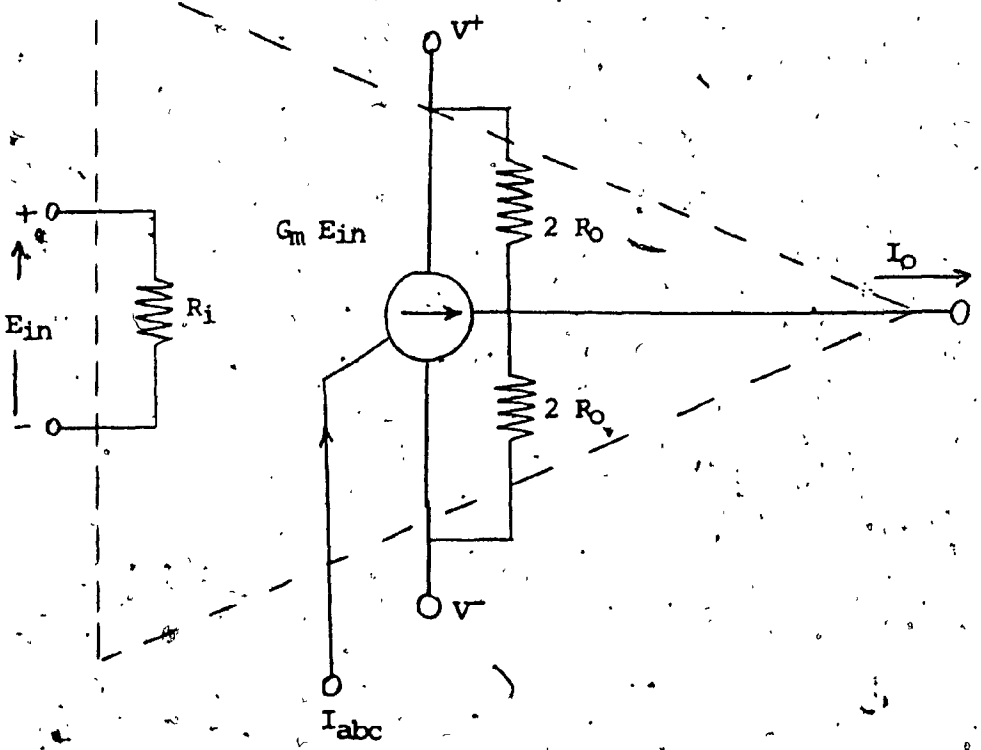

Figure 1: A frequency independent model of the OTA

From the circuit model of Fig. 1, it can be seen that the differential input of an OTA is identical to that of a standard OA, and it operates in a similar fashion. However, the output of an OA is a voltage controlled voltage source with a very low value series resistance, whereas the output of the OTA is a voltage controlled current source (E_{in} G_m), in parallel with the output resistance R_o. R_o is modelled as two resistances of value $2R_o$, connected to V+ or V- since the output current is not referred to ground but may flow to either V+ or V- as well. Furthermore, the transconductance value G_m can be externally controlled through the current I_{abc}.

Consider Fig. 2 which shows an OTA used in an open loop configuration and let A_{vo} be the open loop voltage gain of the circuit.

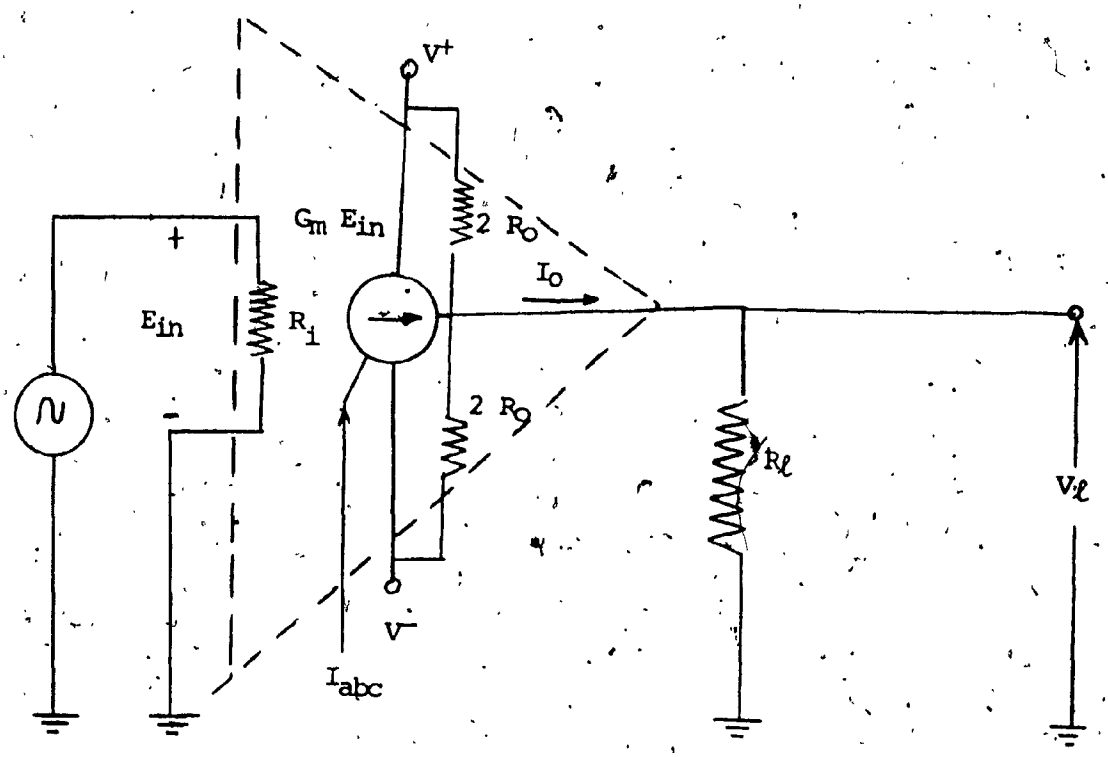

Figure 2: The OTA in open loop configuration

For an ideal OTA, R_0 approaches infinity, therefore we can write:

$$A_{vo} = \frac{V_\ell}{E_{in}} = \frac{I_0 R_\ell}{E_{in}} = \frac{G_m E_{in} R_\ell}{E_{in}} = G_m R_\ell \qquad (1.1)$$

Note that if we remove R_ℓ from the circuit, then:

$$A_{vo} = G_m R_0 \qquad (1.2)$$

Since R_0 is ideally infinite, this would make the gain ideally infinite, as with standard OA (practically in both cases, the output voltages are limited by the power supply voltages). However, equation 1.1

shows that the open loop voltage gain of the OTA can be reduced by external loading unlike the standard OA. In particular, from Fig. 2, we see that the open loop voltage gain of the OTA is directly proportional to the value of the load resistance R_ℓ.

1.3 An OTA frequency dependent model

The model of Fig. 1 is a frequency independent model. In order to make is useful to the filter designer, we must refine this model by taking into consideration the frequency dependence of the open loop gain of the unit.

By selecting a value of $R_\ell << R_0$, equation 1.1 will hold; and, since resistances are frequency independent elements, we conclude that G_m must be the frequency dependent variable which is mostly responsible for generating a frequency dependent open loop gain.

That is to say, if we can find an expression for $G_m(w)$, an expression for $A_{vo}(w)$ can be obtained.

1.4 Inductance Simulation

The properties of passive RLC filters have been extensively studied. The major drawbacks of these filters are due to the use of passive inductors. Some of the several disadvantages that are encountered by the designer making use of passive inductors are the following:

(I) They are not off-the-shelf items.

(II) Inductors using ferromagnetic materials are basically non-linear elements.

(III) They tend to act as small antennas and this property can result in undesirable noise and coupling of signals in the circuit in which they are used.

(IV) They are costly.

(V) They are not suitable for miniaturization.

The major incentive which spurred the development of RC network synthesis was the need to build filters which did not contain inductors.

Many methods of active RC network synthesis have been proposed, mostly using operational amplifiers, fixed gain amplifiers or negative impedance converters as active elements. Most of the configurations, however, are very sensitive to components variations.

The interest in inductance simulation arose when it was shown by Orchard [16] that an LC network matched at either end presents a very low sensitivity of transfer function to the component variations. Thus, a simple way of designing a low-sensitivity active RC filter consists in designing a conventional RLC filter for the prescribed specifications, and then replace the inductances by simulated inductances. Apart from the low-sensitivity property, the other striking advantage of this approach is due to the availability of tabulated data and filter design programs for LC filters.

Inductance simulation consists in using a capacitatively terminated gyrator circuit. Many gyrator configurations have been put forward, one of such configuration is based on an ideal circuit given by Sharpe [17] where two voltage controlled current sources, one with positive and the other with negative transconductance are connected in parallel and back to back. Since the OTA is essentially a voltage controlled current source, it should be possible to make use of it as an inductance simulator.

1.5 Scope of the thesis

The first objective of this study is to find a frequency dependent model of the 3080 OTA. The second objective is to investigate the use of

of the 3080 OTA as the active element for a grounded inductance simulator circuit.

The investigations will show the usefulness of using the OTA as an active element in circuit applications may be limited by its restricted dynamic range. Consequently, the third objective of this thesis is to present a technique for extending the dynamic range of the OTAs. An equivalent circuit of the inductance simulator circuit using the OTA in the proposed technique is also given.

The thesis is divided into five main chapters. In chapter 2, a study of the linear dynamic of the LM3080 OTA is carried out and a frequency dependent model for the transconductance is developed. In chapter 3, an investigation of the use of the OTA as an inductance simulator is presented. The indefinite admittance matrix of the OTA with finite input and output impedances is derived; hence, the Y-parameters of the inductor simulator circuit using two OTAs are obtained. Using network synthesis, a model for the input impedance of the inductor simulator is realized. The model presented shows the effects of the finite input, output resistance as well as the effects of the finite bandwidth of the transconductance on the simulated inductance. Finally, a comparison between experimental and theoretical results is presented. Chapter 4 introduces a new Voltage Controlled Current Source configuration using two OTAs which is shown to exhibit an extended dynamic range in comparison to the single OTA. Hence, a model for an inductance simulation circuit using this new Voltage Controlled Current Source configuration is derived. Possible extensions of this work are indicated in Chapter 5.

CHAPTER 2

A FREQUENCY DEPENDENT MODEL FOR THE TRANSCONDUCTANCE OF THE 3080 OTA

2.1 The need for the linearity of the OTA

If the OTA is to be used in filter design, it will be utilized as a linear element. OUr model for Gm(w) must therefore be obtained over the linear region of the OTA. Our first task will be to define this linear region. We will therefore test the OTA for linearity.

Linearity will certainly be affected by the input differential voltage and may also be affected by the load resistance, and by the bias current. The effects on the output current of the input differential voltage have already been investigated by Kaplan and Wittlinger [6]. However, this investigation does not specify whether the bias current or the load resistance could affect the linearity of the OTA. The test results which will be presented in this thesis will answer these questions and furthermore, will provide the value of Gm(0) [Gm(w)|w = 0] which will be used in the final expression of Gm(w). They will also test the validity of equation 1.1 and the programability of the transconductance of the OTA.

2.2 Experimental measurements of Gm(0) and testing of the linearity range of the OTA

Fig. 3 shows the experimental circuit which was employed to establish the linearity of the transconductance of the OTA. The LM3080N which is the equivalent of the CA3080E (8-lead dual-in-line plastic, MINI-DIP, package) was used.

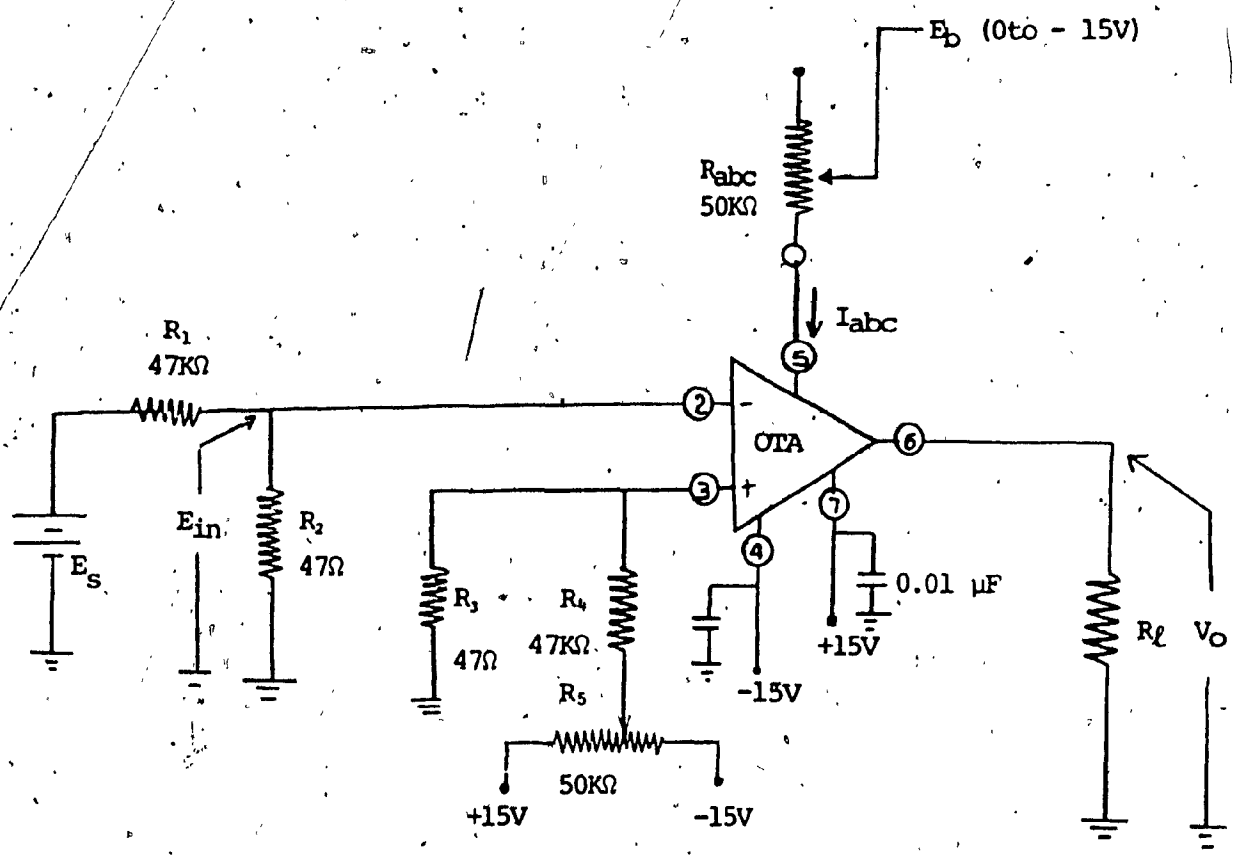

Figure 3: Linearity test circuit

DC voltages were used in order to avoid the effects of the circuit capacitances, measuring probe capacitance and the frequency dependent gain of the OTA.

The two 0.01 μF capacitors were used to eliminate any switch on transients from the power supplier. R_3 was used as the compensating resistor for input bias currents and R_5 was employed to eliminate any DC offset at the output of the OTA. R_1 and R_2 were used to form a ten to one voltage divider in order to facilitate input voltage measurements.

I_{abc} was set using the combination of the R_{abc} pot and the voltage E_b. From Fig. A1 in appendix 1, it can be seen that the bias current can be calculated from the equation:

$$I_{abc} = \frac{|V^-| - V_{54} - |E_b^-|}{R_{abc}} \qquad (2.1)$$

where V_{54} is the voltage drop across pin 5 and pin 4. This voltage drop at normal temperature varies from 0.55 volts for an I_{abc} value of 1 μA to about 0.75 volts for an I_{abc} of 1000 μA. Precise values of I_{abc} were obtained by ammeter readings.

Measurements were taken for input voltages E_{in} ranging from zero to 150 mV, for load resistors of 1 KΩ, 10 KΩ, 100 KΩ, and for bias currents values of 1 μA, 10 μA, 100 μA, 400 μA, 600 μA and 1000 μA.

It should be noticed that for each combination of R_ℓ and I_{abc}, the assumption implied in deriving equation 1.1 holds true. In fact the lowest value of R_0 which occurs at the largest value of bias current is 7.5 MΩ [1]; hence, $R_0 \gg R_\ell$ and $A_{vo} = Gm\ R_\ell$.

For a detailed measurements procedure, the reader should look into appendix II.

It should be noted that in Fig. 3, E_{in} is applied to the inverting terminal, thus positive input voltages resulted in negative output voltages. If terminals 2 and 3 are interchanged the circuit characteristics remain identical, with the exception that positive input generate positive voltage outputs.

Figures 4.1a, b, c, d, e; 4.2a, b, c, d, e; and 4.3a, b, c, d, e display the results of the linearity tests.

Section 2.3 will analyze these results in the light of the objectives laid out in section 2.1.

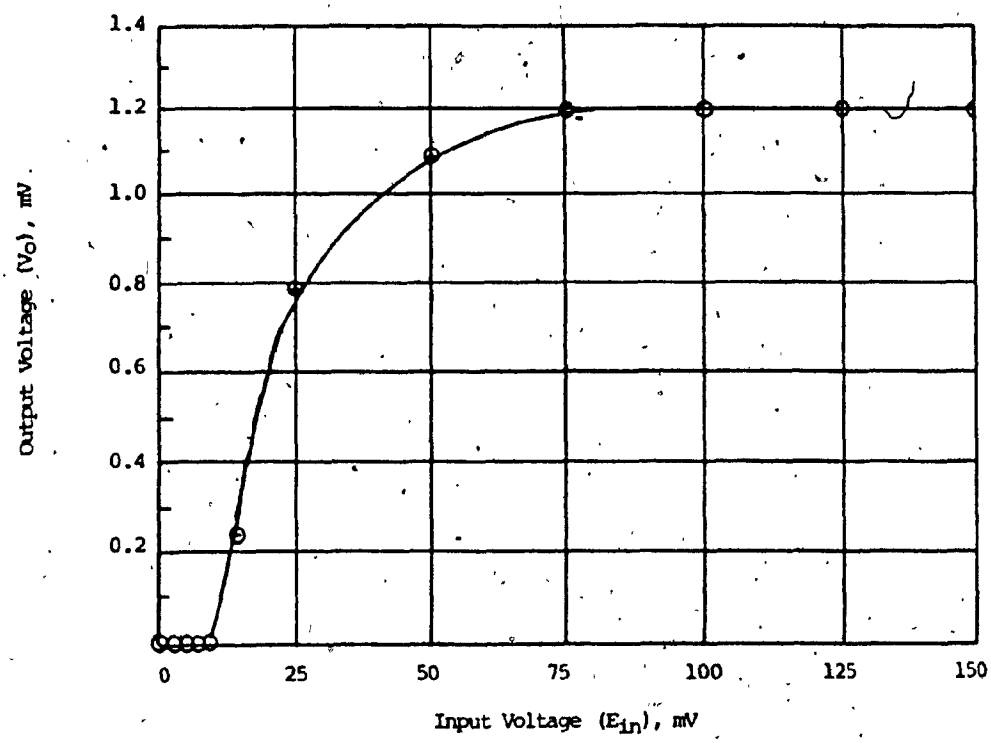

Figure 4.1 a: V_o versus E_{in}

$R_\ell = 1\ K\Omega$, $I_{abc} = 1\ \mu A$

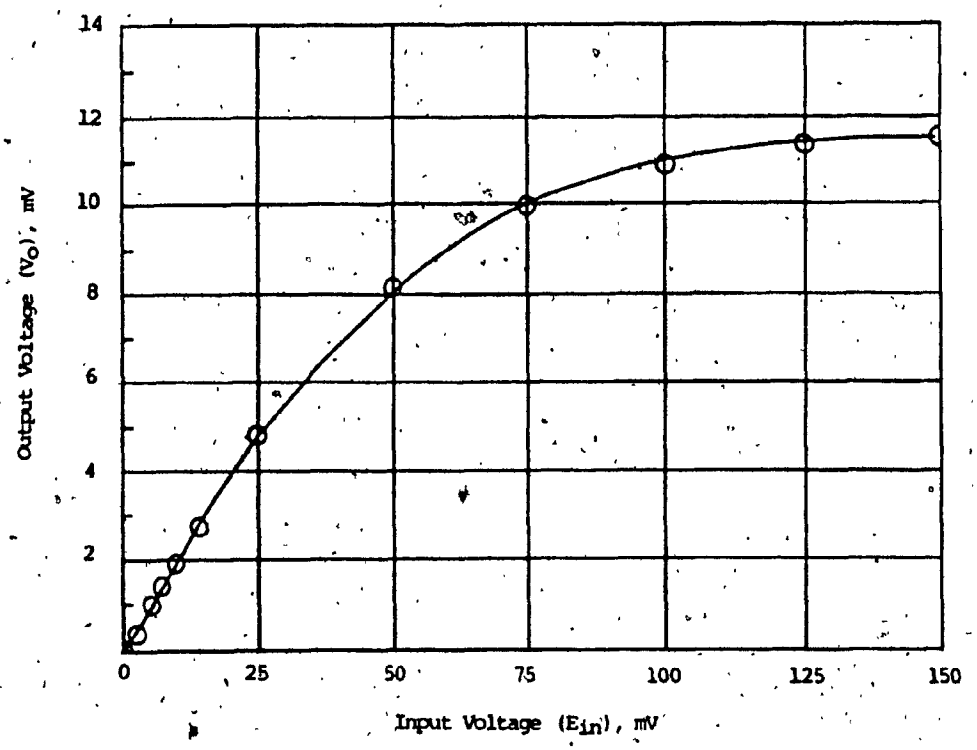

Figure 4.1b: V_o versus E_{in}

$R_\ell = 1\ K\Omega$, $I_{abc} = 10\ \mu A$

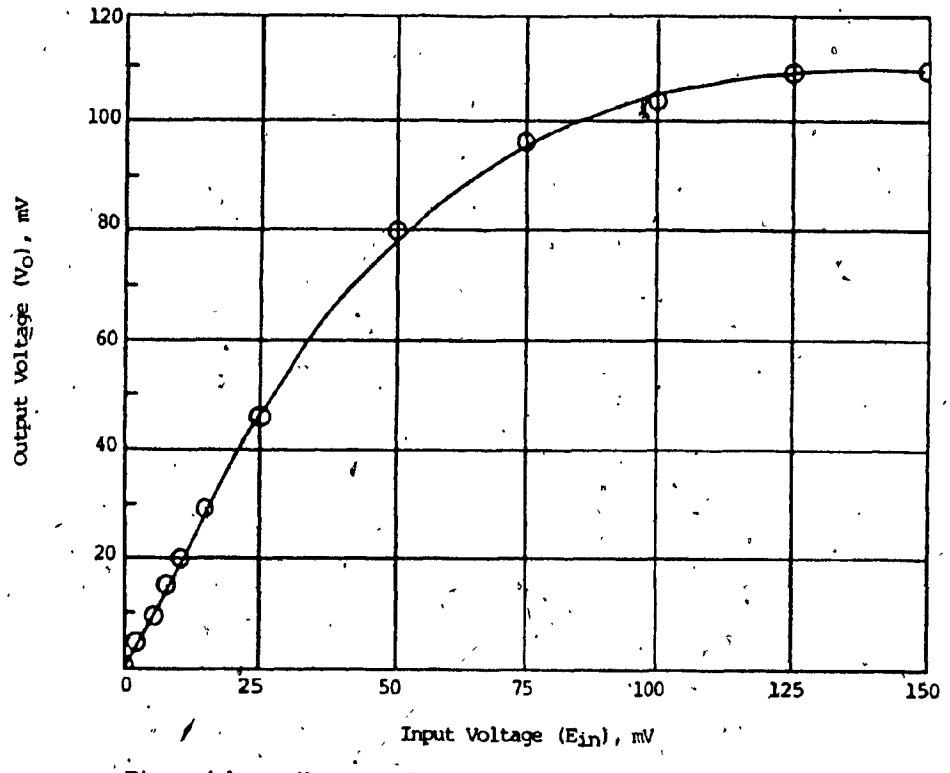

Figure 4.1 c: V_o versus E_{in}

R_ℓ = 1 kΩ, I_{abc} = 100 μA

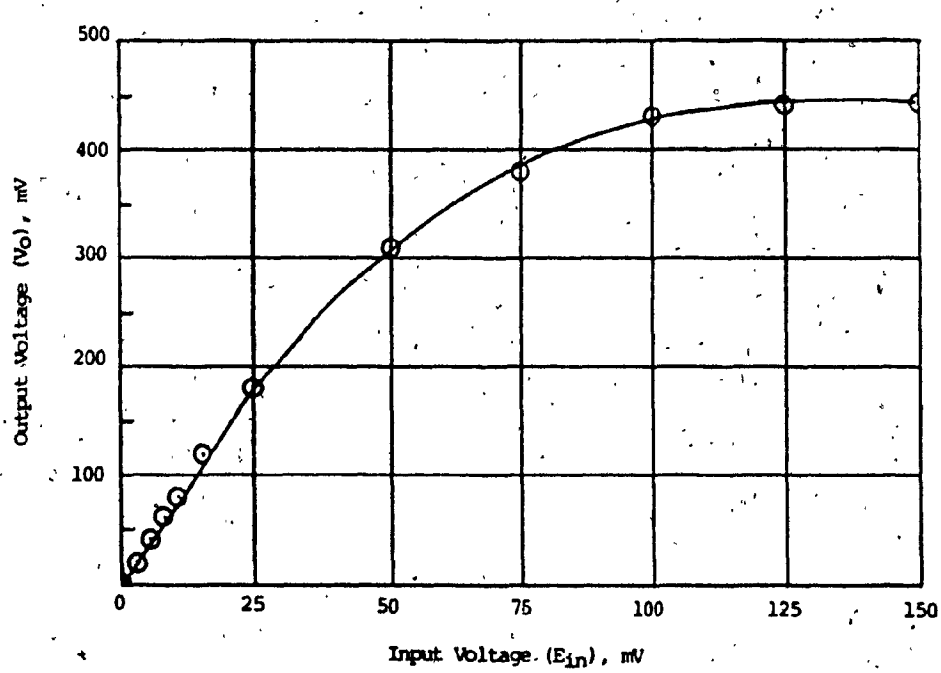

Figure 4.1 d: V_o versus E_{in}

R_ℓ = 1 KΩ, I_{abc} = 400 μA

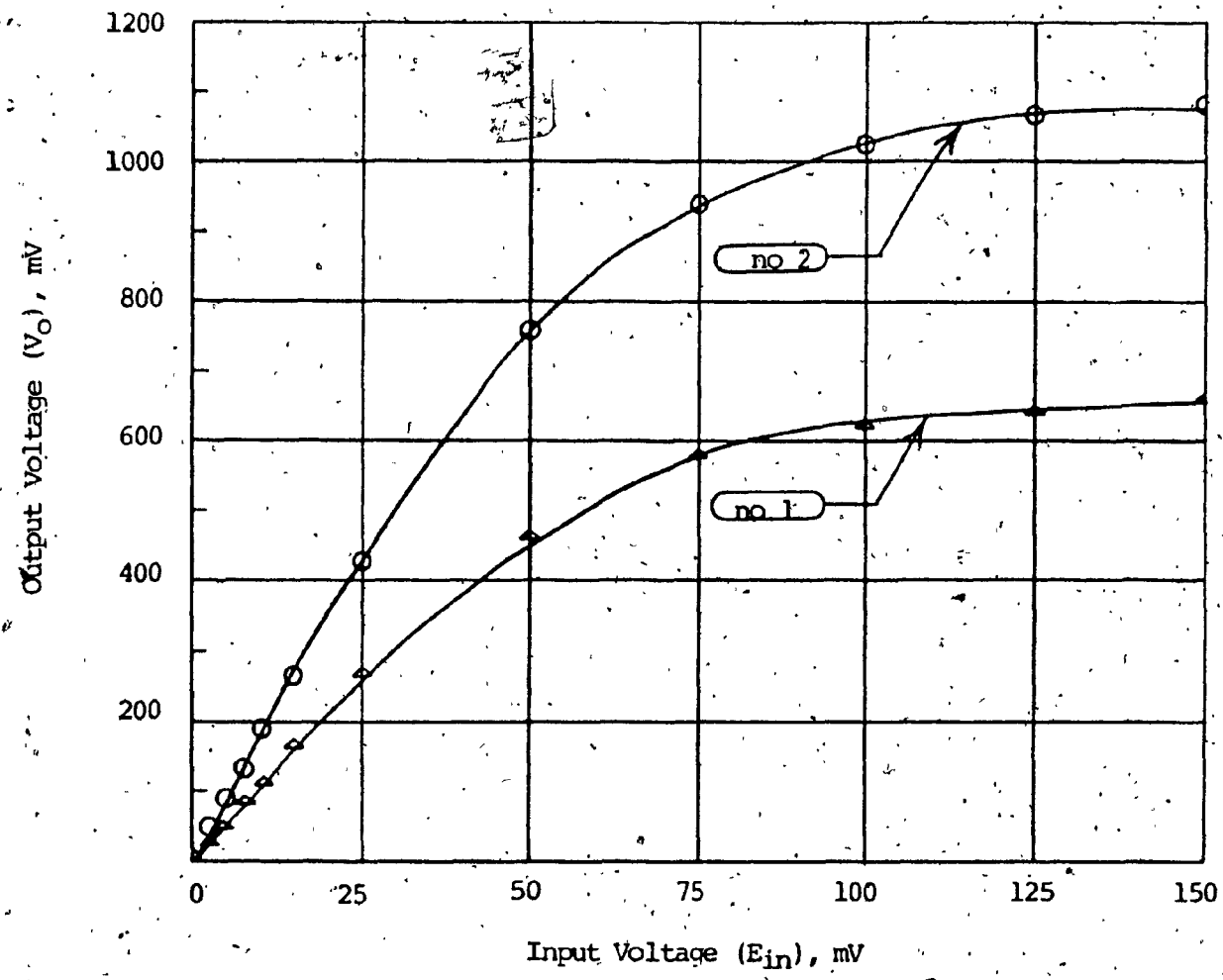

Figure 4.1 e: V_o versus E_{in}

R_ℓ = 1 KΩ, I_{abc} = 600 μA - Curve 1
R_ℓ = 1 KΩ, I_{abc} = 1000 μA - Curve 2

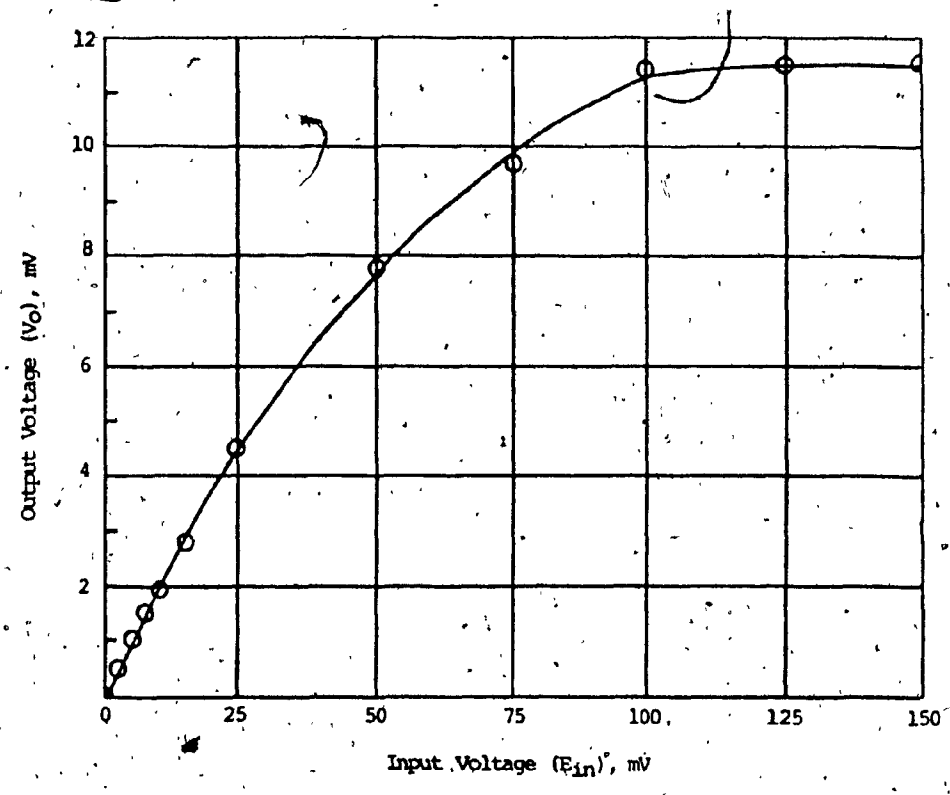

Figure 4.2 a: V_o versus E_{in}

R_ℓ = 10 KΩ, I_{abc} = 1 μA

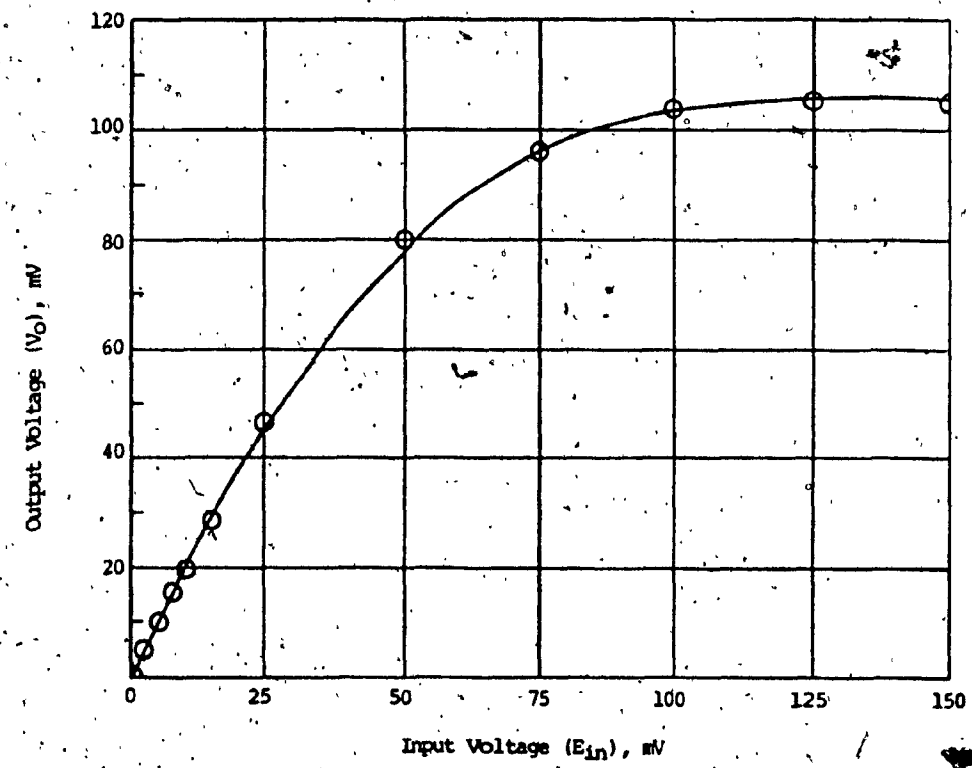

Figure 4.2 b: V_o versus E_{in}

R_ℓ = 10 KΩ, I_{abc} = 10 μA

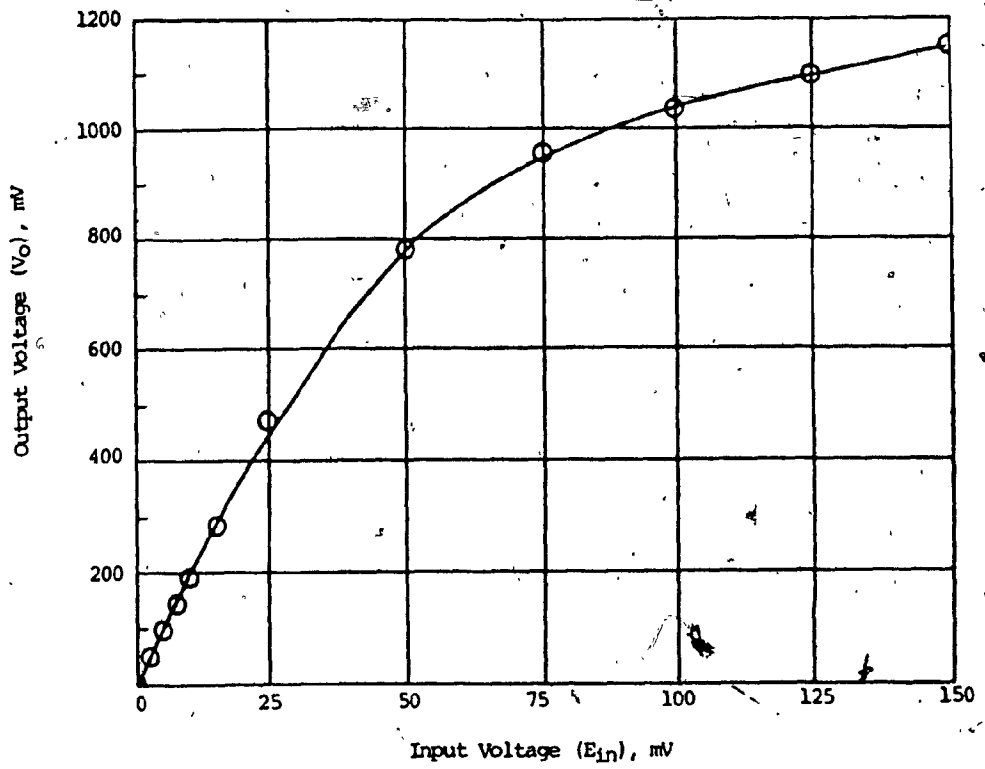

Figure 4.2 c: V_o versus E_{in}

R_ℓ = 10 KΩ, I_{abc} = 100 μA

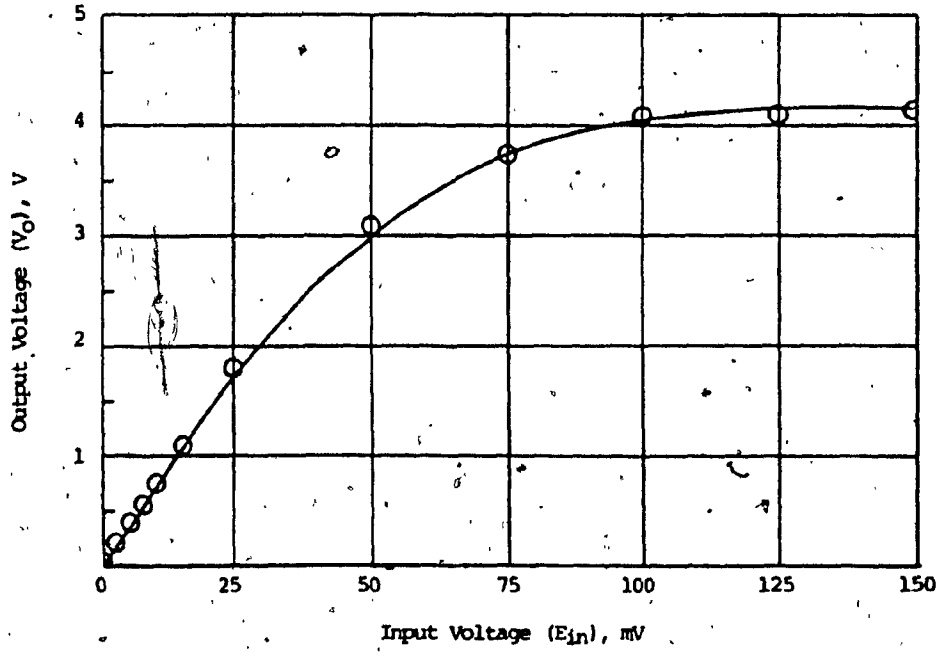

Figure 4.2 d: V_o versus E_{in}

R_ℓ = 10 KΩ, I_{abc} = 400 μA

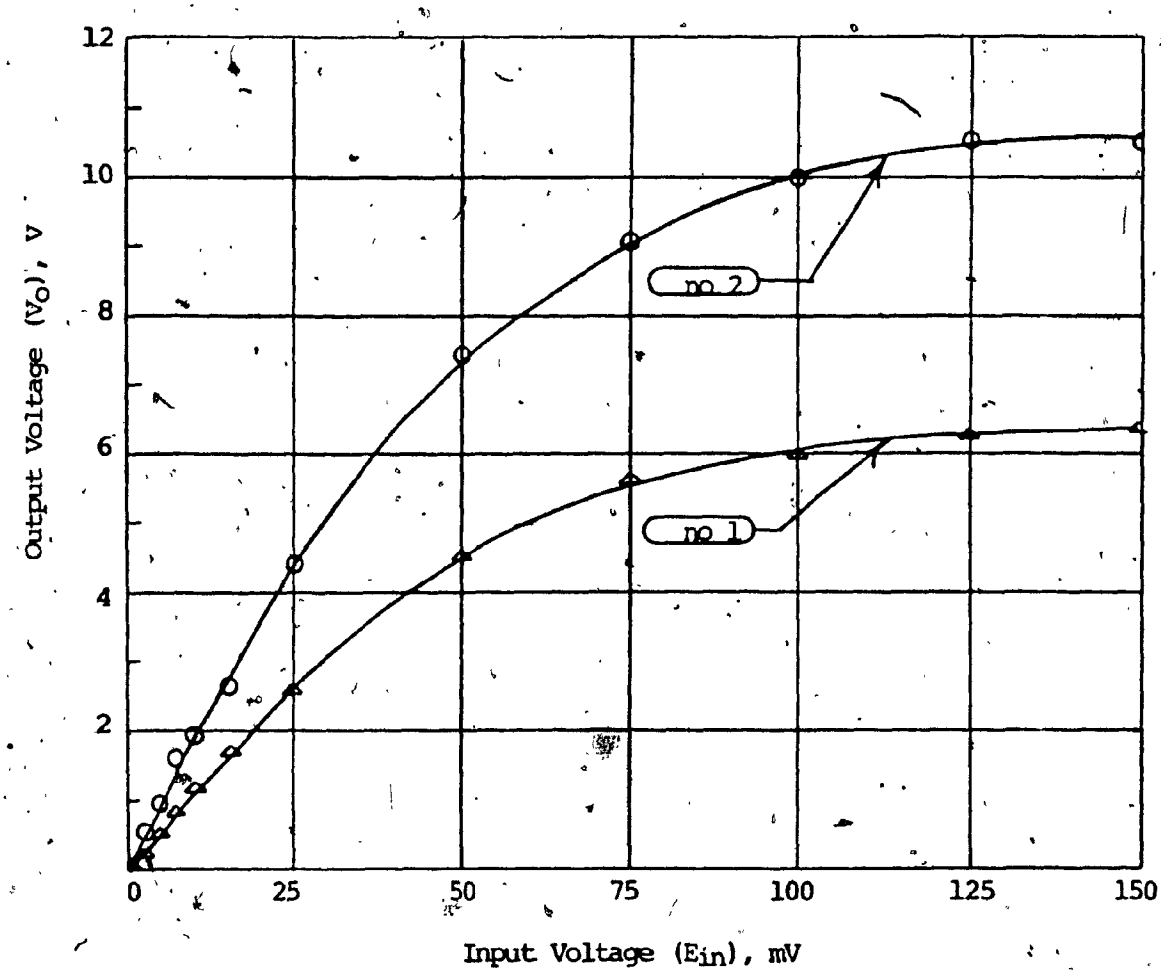

Figure 4.2 e: V_o versus E_{in}

$R\ell_1$ = 10 KΩ, I_{abc} = 600 μA - Curve 1
$R\ell$ = 10 KΩ, I_{abc} = 1000 μA - Curve 2

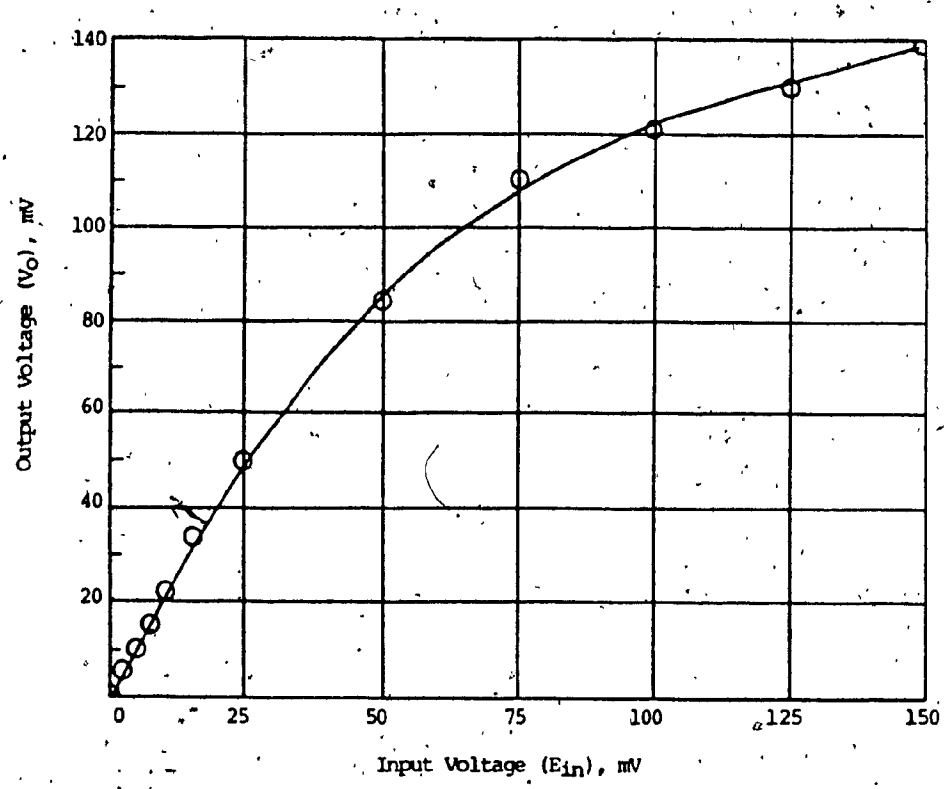

Figure 4.3 a: V_o versus E_{in}

R_ℓ = 100 KΩ, I_{abc} = 1 μA

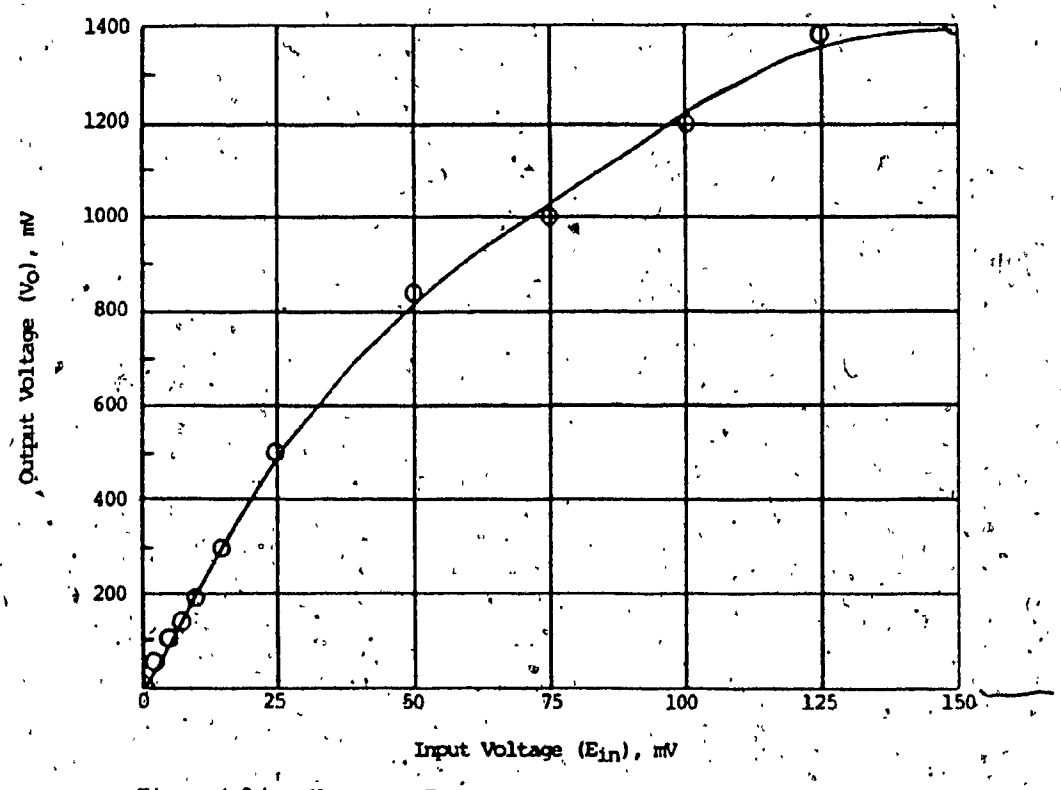

Figure 4.3 b: V_o versus E_{in}

R_ℓ = 100 KΩ, I_{abc} = 10 μA

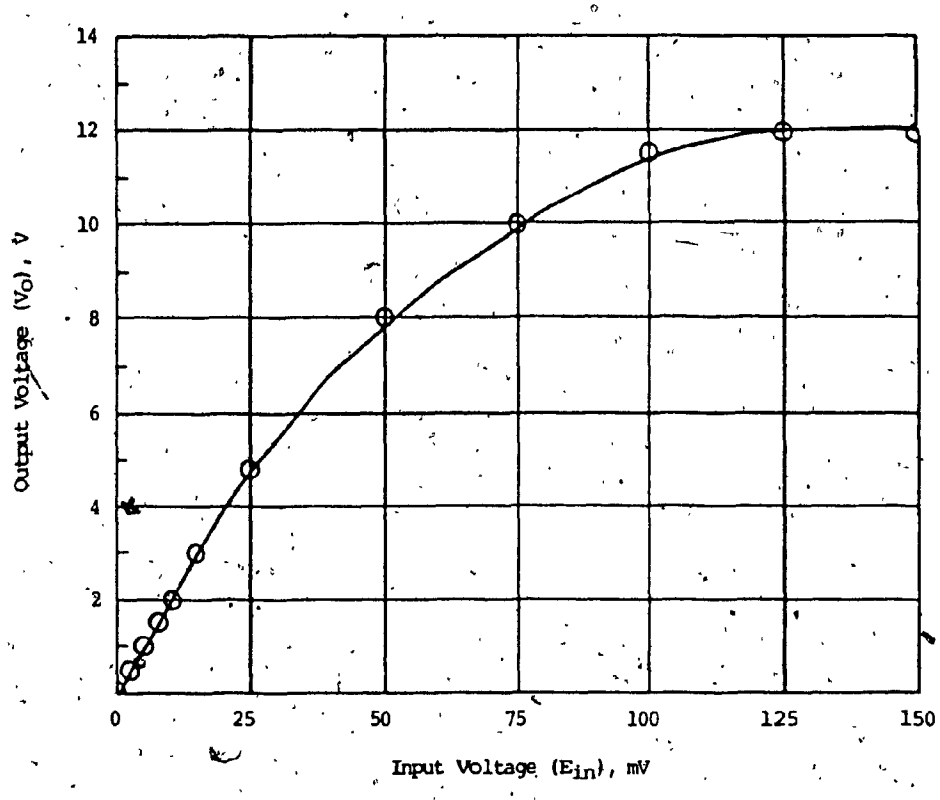

Figure 4.3 c: V_o versus E_{in}

R_ℓ = 100 KΩ, I_{abc} = 100 μA

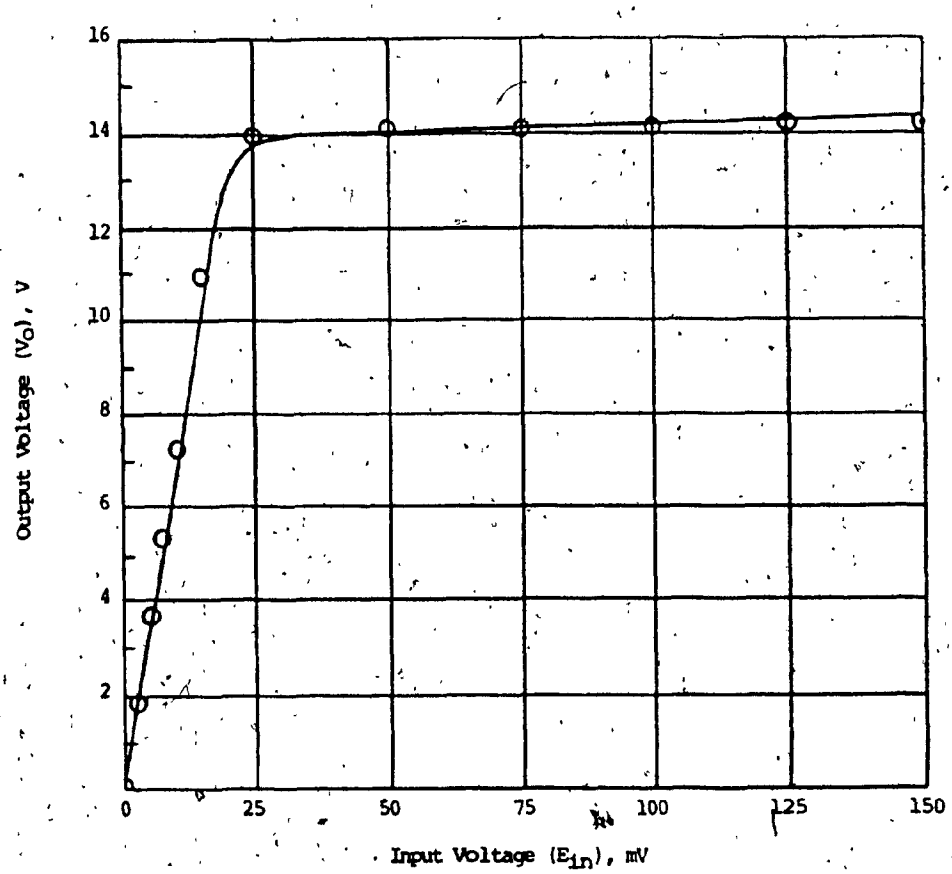

Figure 4.3 d: V_o versus E_{in}

R_ℓ = 100 KΩ, I_{abc} = 400 μA

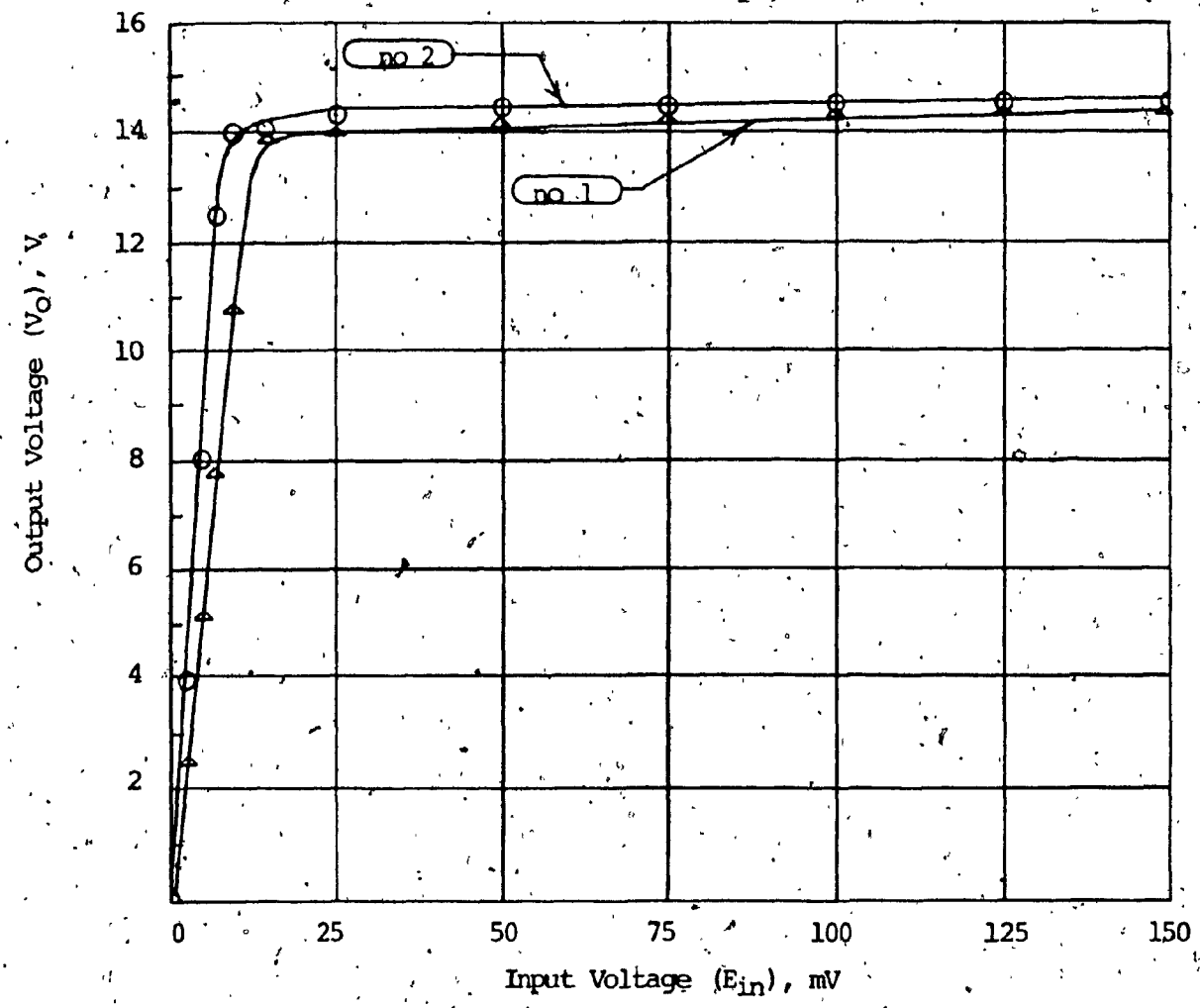

Figure 4.3 e: V_o versus E_{in}

R_ℓ = 100 KΩ, I_{abc} = 600 μA - Curve 1
R_ℓ = 100 KΩ, I_{abc} = 1000 μA - Curve 2

2.3.1 The linear range of the OTA

The linear range of the OTA displayed by the graphs[1] presented in section 2.2 (Fig. 4.1, 4.2, 4.3) is about 25 mV; therefore, a ±25 mV input signal will be linearly amplified [(ex.: Fig. 4.2a)] or attenuated (ex.: Fig. 4.1b) by the OTA. This statement is valid provided we are dealing with outputs voltages which do not exceed V_{OM+} or V_{OM-} (the maximum peak output voltages) [1]. Fig. 4.3, for instance, shows a more limited dynamic range of 10 mV, since in this case V_{OM-} limits the output voltage for input values over 10 mV.

We can, therefore, summarize the linearity characteristics of the OTA by stating that linear range is ±25 mV, provided the output current reaches I_{OM} [The peak output current] [1] before the output voltage reaches V_{OM}. If the output voltage reaches V_{OM} before the output attains I_{OM}, the linear range of the OTA will be less than ±25 mV.

2.3.2 Verification of the Open loop Voltage equation

Equation 1.1 states that the open loop voltage gain of the OTA is directly proportional to the load resistor R_ℓ.

Table 1 which was obtained from the data presented in Fig. 4.1, 4.2, 4.3 proves, within practical limits, the validity of such statement.

Note 1: The data displayed by Fig. 4.1a has been disregarded due to test instrument limitations (details are discussed in Appendix II).

TABLE 1

Open loop voltage gain (A_{vo}) versus load resistance (R_ℓ) for E_{in} = 10 mV

I_{abc} µA	A_{vo} R_ℓ = 1 KΩ	A_{vo} R_ℓ = 10 KΩ	A_{vo} R_ℓ = 100 KΩ
1	0 (1)	0.19	2.2
10	0.2	1.99	19.5
100	2	19.5	195
400	8	75	730
600	11	108	1080
1000	18.5	185	1400 (1600) (note 2)

2.3.3 Programmability and numerical value of $G_m(0)$

Table 2 which follows below, presents the experimental values of $G_m(0)$ calculated from the relation:

$$G_m(0) = \frac{V_0}{E_{in} \cdot R_\ell}.$$

It is understood that these values of $G_m(0)$ are applicable to the linear range of the OTA.

Note 2: A_{vo} = 1400 for E_{in} = 10 mV (limits of linear region)

A_{vo} = 1600 for E_{in} = 2.5 mV

TABLE 2

D.C. value of transconductance in the linear region of the OTA

I_{abc} μA	R_ℓ = 1 KΩ $G_m(0)$ μmho	R_ℓ = 10 KΩ $G_m(0)$ μmho	R_ℓ = 100 KΩ $G_m(0)$ μmho	Manufacturer Spec. $G_m(0)$, μmho, (25°C)
1	16.6	19	22	19
10	200	199	195	190
100	2000	1950	1950	2000
400	8000	7500	7300	8000
600	11000	10800	10800	11000
1000	18500	18500	16000	18000

It is evident from table 2 that the value of R_ℓ does not have a noteworthy effect on the value of $G_m(0)$. Furthermore the transconductance of the OTA can be programmed through its bias current using the relation.

$$G_m(0) \cong 19\ I_{abc} \tag{2.2}$$

Equation (2.2) can be rewritten using equation (2.1) as:

$$G_m(0) \cong 19 \left[\frac{|V^-| - |V_{54}| - |E_b^-|}{R_{abc}} \right] \tag{2.3}$$

Therefore we can program the transconductance by varying voltage Eb^- (refer to Fig. 3).

Outside of the linear region of the OTA, the transconductance value decreases. This behaviour is depicted by Fig. 5 which shows a typical variation of $G_m(0)$ as a function of E_{in} (data is derived from Fig. 4.2a, 4.2b, 4.2c).

In order to describe this characteristic of the OTA unit we will rewrite equation (2.2) in the form:

$$G_m(0) \cong 19 \cdot I_{abc} \cdot CF \tag{2.4}$$

We define:

$$CF \text{ (correcting factor)} = \frac{\text{Actual Value of } G_m}{\text{Nominal Value of } G_m}$$

Nominal Value of $G_m = 19 \cdot I_{abc}$

Actual Value of $G_m(0)$ = Measured value of $G_m(0)$

Therefore, we can state that:

(a) In the linear region of the OTA: $CF \cong 1$

(b) In the non-linear region of the OTA: $CF < 1$

2.3.4 Maximum output current (I_{0M}) as a function of bias current (I_{abc})

Information regarding the relationship between I_{0M} and I_{abc} can also be obtained from fig. 4.1, 4.2, 4.3 using the expression:

$$I_{0M} = \frac{V_{0\ max}}{R_\ell} \tag{2.5}$$

Table 3 presents this information. It is evident that:

$$I_{0M} \cong I_{abc} \tag{2.6}$$

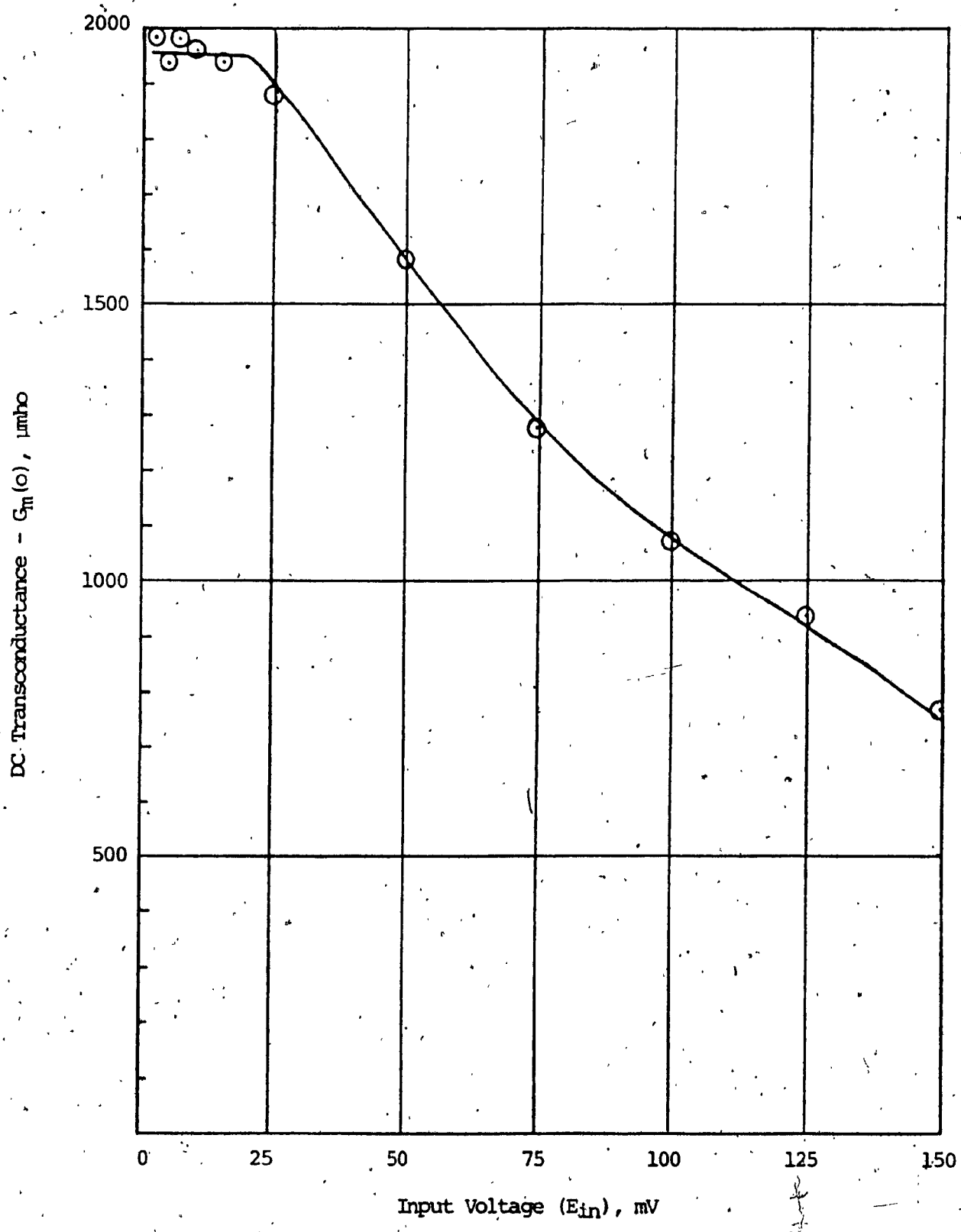

Figure 5: $G_m(o)$ versus E_{in}

I_{abc} = 100 μA
R_ℓ = 1 KΩ; 10 KΩ; 100 KΩ

TABLE 3

I_{OM} versus I_{abc}

I_{abc} μA	R_ℓ = 1 KΩ I_{OM}(μA)	R_ℓ = 10 KΩ I_{OM}(μA)	R_ℓ = 100 KΩ I_{OM}(μA)
1	1.2	1.1	1.4
10	11.5	10.5	14
100	109	115	120
400	440	418	410*
600	660	640	605*
1000	1085	1050	1040*

*In these cases equation (2.5) could not be used to calculate I_{OM} since V+ and V- placed on upper limit on $V_{0(max)}$ before I_0 reached I_{OM}. This data had to be obtained through ammeter measurement.

2.4 Intrinsic Noise

Appendix III presents data regarding intrinsic noise measurements of the circuit of Fig. 3. Two general conclusions have been drawn from these measurements.

(a) For a given value of R_ℓ, the output noise increases as the bias current increases.

(b) For a given value of I_{abc}, the output noise increases as the load resistance increases.

2.5 Measurements of A'_{vo} (w)

Experimental measurements on the value of G_m(w) were conducted on a circuit similar to the one presented in Fig. 3 but with input fed into the non-inverting terminal of the OTA.

In order to obtain meaningful frequency response data, it was found that care had to be taken in minimizing the effects of stray capacitance of the load. Therefore, it was necessary to employ the lowest possible value of load resistor and lowest value of capacitative loading probe.

A value one kiloOhm load resistor and the 10X position of the P6063B probe (Tektronics) were employed. This combination allowed voltage measurements within the oscilloscope sensitivity range while, at the same time, minimizing the capacitative loading effects of the probe, stray capacitances and output noise.

Appendix IV gives details of the measurement technique. Figure 6 presents the experimental data of the open loop voltage gain (A_{vo}) as a function of frequency (d.c. to 15 MHz) for bias currents of 1000 μA, 600 μA, 400 μA and 100 μA. The value of E_{in} was ±25 mV, while the load resistor was R_ℓ = 1 KΩ.

The phase shift between input and output (curve no. 5) was found to be independent of the bias current.

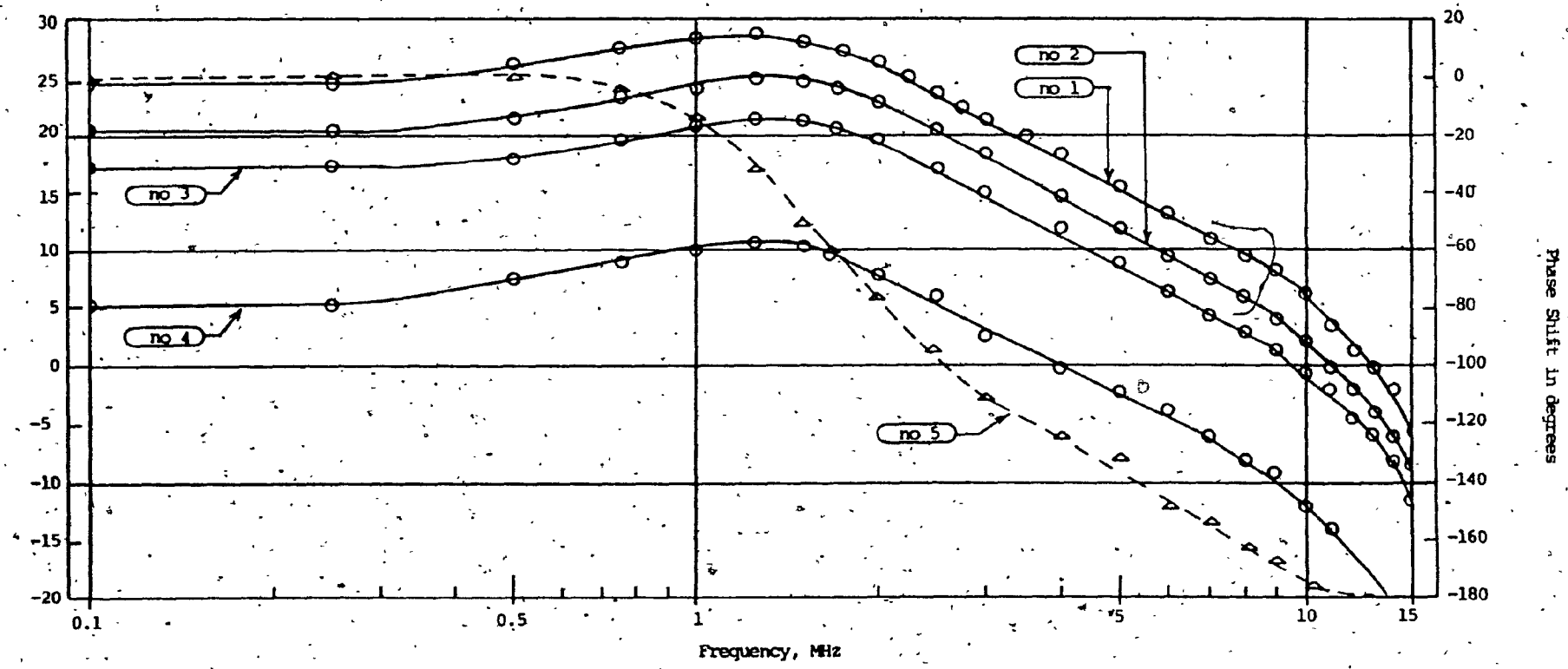

Figure 6: Measurements of A_{vo} (w), R_ℓ = 1 KΩ

Curve 1: A_{vo} versus frequency, I_{abc} = 1000 μA
Curve 2: " " " " = 600 μA
Curve 3: " " " " = 400 μA
Curve 4: " " " " = 100 μA
Curve 5: Phase Shift of V_ℓ versus E_{in}

2.6 Compensation of data for stray capacitances effects

The data for $G_m(w)$ can be derived from the data obtained for $A_{vo}(w)$.

In fact, from equation 1.1, we can write:

$$G_m(w) = \frac{A_{vo}(w)}{R_\ell} \tag{2.7}$$

The theoretical load value presented by the circuit of Fig. 3 which was used to obtain the data of $A_{vo}(w)$ is $R_\ell = 1\ K\Omega$. However, the actual value of the load was the parallel connection of R_ℓ, the probe resistance ($R_p = 10\ M\Omega$) and the probe capacitative component (C_p) which was experimentally calculated to be 20 pF (appendix IV). Hence, the actual load that was presented to the output of the OTA was:

$$Z_\ell = R_\ell // R_p // C_p \cong \left[\frac{R_\ell}{1 + S\,C_p\,R_\ell}\right] \tag{2.8}$$

Therefore, the data displayed by Fig. 6 is for:

$$A_{vo}(s) = G_m(s)\left[\frac{R_\ell}{1 + S\,C_p\,R_\ell}\right] \tag{2.9}$$

In order to be able to find $G_m(w)$ using 2.7, we must correct the data of Fig. 6 by multiplying it by the factor: $(1 + S\,C_p\,R_\ell)$. This compensation is shown in Fig. 7 for the graphs no. 1 and no. 5 of Fig. 6. The numerical value of the compensating factor is: $1 + S\,C_p\,R_\ell = 1 + j\,W\,20 \cdot 10^{-9}$

hence: $f\ 3dB \cong 8\ MHz$

The importance of taking in consideration the stray capacitances which may be present at the output of the OTA is clearly illustrated by Fig. 8. In this case, the data was obtained when the value of load resistance was increased to 100 KΩ and bias current values of 100 μA, 10 μA, and 1 μA were used. From Fig. 6 we know that the bandwidth of the OTA is well over 80 KHz; however, in Fig. 8 the effect of the $(1 + S\,C_p\,R_\ell)$ term drastically reduces it to about 80 KHz.

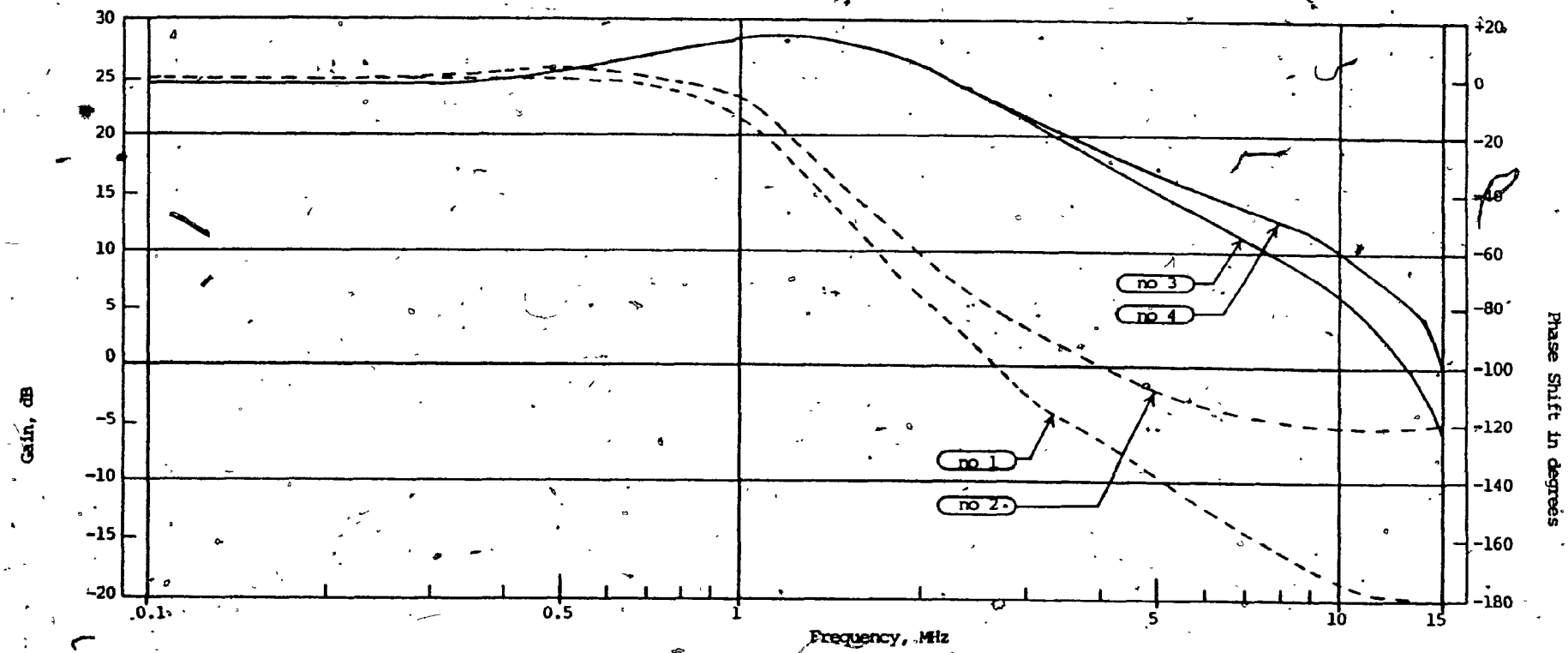

Figure 7: Compensation of measurements for A_{vo} (w) (Fig. 6)

Curve 1: Phase Shift of V_ℓ versus E_{in} from Fig. 6
Curve 2: Compensated Phast Shift Measurement
Curve 3: $|A_{vo}|$ versus frequency, I_{abc} = 1000 A, (from Fig. 6)
Curve 4: Compensated $|A_{vo}|$ versus frequency measurement

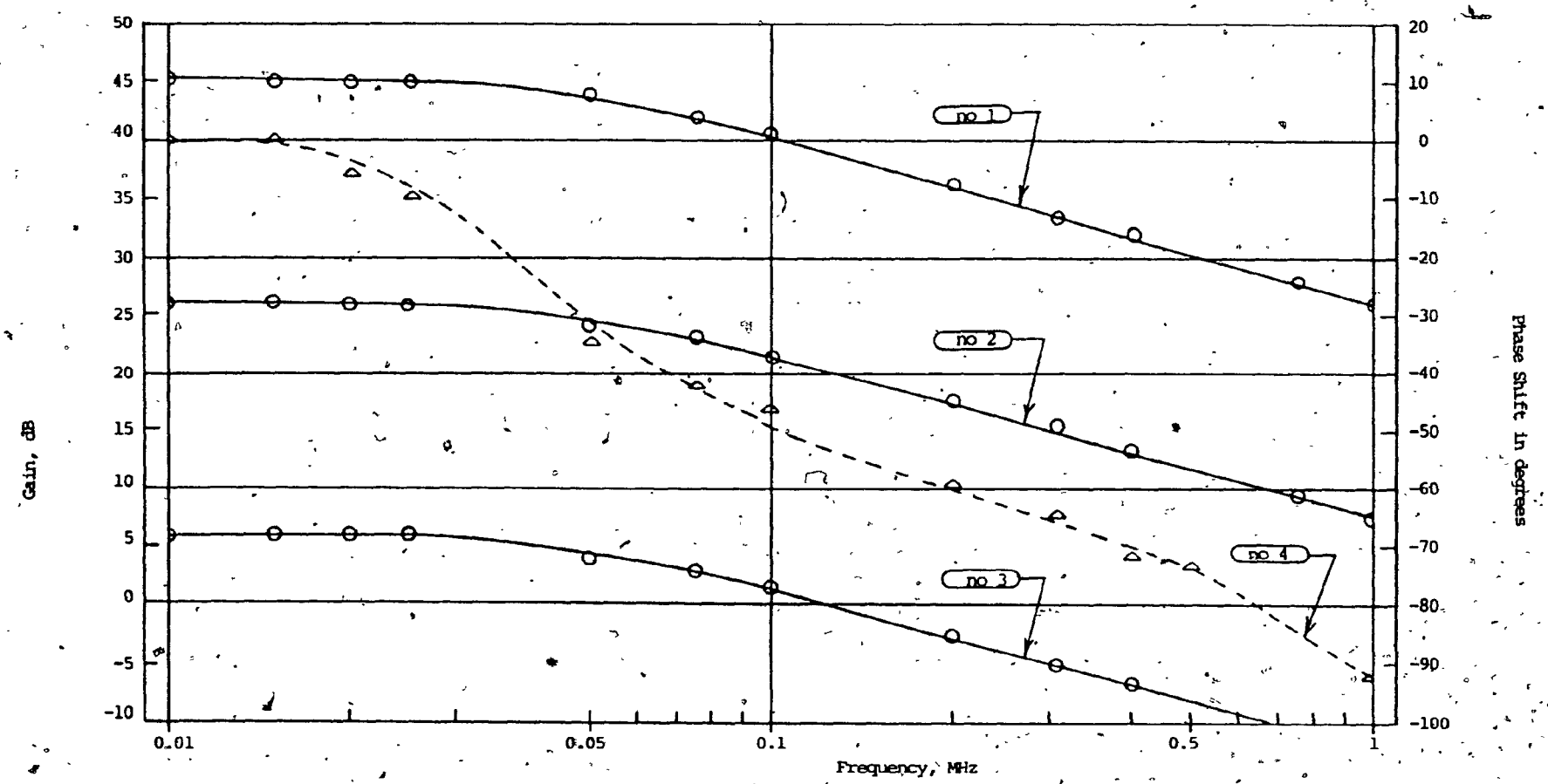

Figure 8: Uncompensated measurements of A_{vo} (w), R_ℓ = 100 KΩ

Curve 1: Uncompensated measurement of A_{vo} (w), I_{abc} = 100 μA
Curve 2: " " " " " = 10 μA
Curve 3: " " " " " = 1 μA
Curve 4: Uncompensated Phase Shift measurement

2.7 Additional experimental data

Additional experimental data was obtained to find out whether the length of lead wires and physical layout of the test circuit had any substantial effect on the results of the test and whether the data obtained for the particular unit was an exceptional or a typical one.

Test results on the same unit were obtained using a different physical layout of the circuit and different length of interconnecting wire. It was concluded that physical circuit layout was not a determinant factor for the characteristics of the unit presented in Fig. 6.

Two additional units were tested for bias current values of 400 μA, under the same conditions employed for first unit. A comparison of the data obtained for the three different units is presented in Appendix V. From this comparison, we conclude that it is reasonable to assume that the data presented in section 2.6 represents a typical response of the 3080 OTA unit.

2.8 A model for $G_m(w)$

Considering equation (2.7) and the data obtained for $A_{vo}(w)$ two general conclusions can be drawn about $G_m(w)$.

(a) The bias currents do vary the value of $G_m(0)$; however, they do not vary the shape of the $|G_m(w)|$ curve.

(b) The phase of $G_m(w)$ is independent of bias current.

The shape of the $|A_{vo}(w)|$ curve suggests that we could try fitting a second order system of the form:

$$A_{vo}(w) = \frac{K_0}{a(jw)^2 + b(jw) + 1} \qquad (2.10)$$

where $K_0 = G_m(0)\ R_\ell$ (2.11)

Values of $G_m(0)$ for E_{in} = ±25 mV are available from Fig. 4.1c, d, e. Thus a comparison of our model for K_0 and the data of Fig. 6 is possible.

TABLE 4

Model for K_0 versus actual value of K_0

I_{abc} μA	Model Value of K_0 (dB)	Actual Value of K_0 (dB) (Fig. 6)
100	5.3	5.3
400	17.14	17.2
1600	20.6	20.6
1000	24.4	24.5

The comparison shows that our model for K_0 is valid.

We can write the denomination of equation 2.10 as:

$$D(s) = a\ (jw)^2 + b\ (jw) + 1 = \left(\frac{jw}{W_n}\right)^2 + \left(\frac{2\ \sigma}{W_n}\right) jw + 1 \qquad (2.12)$$

where: W_n = natural frequency of the complex poles

σ = damping constant

$$\text{hence: } a = \frac{1}{W_{n^2}} \quad \text{and} \quad b = \frac{2\sigma}{W_n} \qquad (2.13)$$

A normalized second order system is of the form:

$$H(w) = \frac{1}{\left(\frac{jw}{W_n}\right)^2 + \left(\frac{2\sigma}{W_n}\right) jw + 1}$$

$$|H(w)| = \frac{1}{\left[\left(\frac{2\sigma W}{W_n}\right)^2 + \left(1 - \frac{W^2}{W_n^2}\right)^2\right]^{\frac{1}{2}}}$$

We can find the maximum value of $|H(w)|$ by taking the derivative and setting its value equal to zero and solving for w.

The maximum value occurs at the resonant frequency (W_r). For $\sigma < 0.707$ (which is our case) this value of W_r is given by:

$$W_r = W_n \sqrt{1 - 2\sigma^2} \tag{2.14}$$

and the maximum value of $|H_{(w)}|_{max} = [2\sigma\sqrt{1-\sigma^2}]^{-1}$ (2.15)

From our data we can obtain W_r and the normalized $|H_{(w)}|_{max}$; thus we can solve for σ and W_n.

$$W_r = 1.23 \cdot 10^6 \cdot 6.28 \text{ rad/sec} \tag{2.16}$$

$$|H_{(w)}|_{max}(dB) = |A_{vo}(w)|_{max}(dB) - |A_{vo}(0)|(dB) = 4dB$$

Hence $|H_{(w)}|_{max} = 1.58$ (2.17)

Using (2.16) and (2.17) we can solve for W_n and σ in (2.14) and (2.15). These are standard equations whose graphical solution can be found in technical literature [8] (see also Fig. A 4.2).

We obtain: $W_n = 8.54 \cdot 10^6$ rad/sec; fn = 1.36 MHz (2.18a)

$\sigma = 0.33$ (2.18b)

Therefore: $a = \frac{1}{W_n^2} = 13.7 \cdot 10^{-15}$ (2.19)

$b = \frac{2\sigma}{W_n} = 7.25 \cdot 10^{-8}$

and our first approximation model is:

$$A_{vo}(w) = \frac{G_m(0)\ R_\ell}{13.7 \cdot 10^{-15}\ (jw)^2 + 7.25 \cdot 10^{-8}\ (jw) + 1} \qquad \text{(Preliminary Model)} \qquad (2.20)$$

A comparison of the measured phase characteristics of the OTA (curve no. 1) and the phase characteristics predicted by the model of equation (2.20) (curve no. 2) is shown in Fig. 9. It is apparent that a discrepancy exist between the two. This discrepancy can be corrected if we add a phase connecting term to our second order model of the form:

$$\theta = \tan^{-1} \frac{W}{W_n} \qquad (2.21)$$

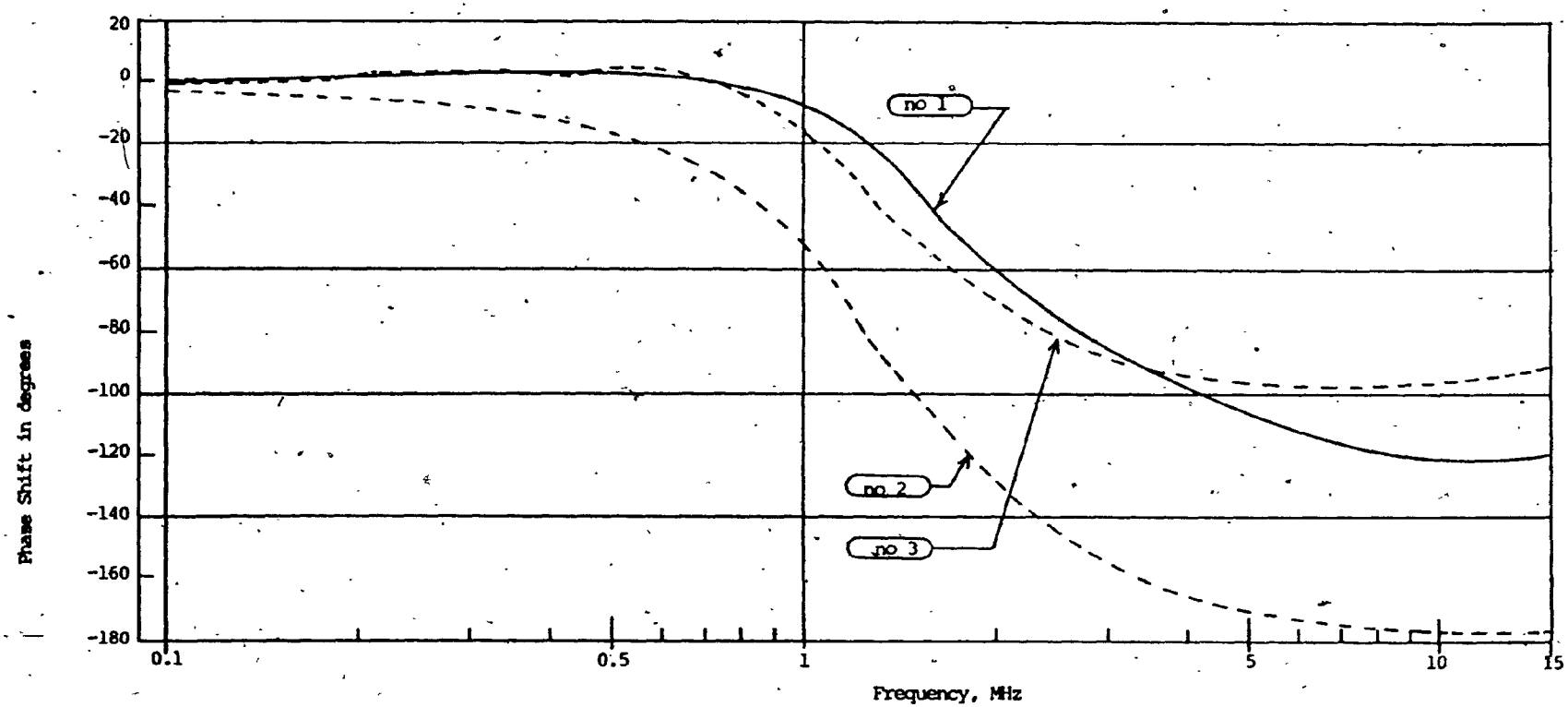

Figure 9: Comparison of the model and experimental data of the input to output Phase Shift of the 3080 OTA

Curve 1: measured input to output phase shift of the OTA
Curve 2: phase shift predicted by equation 2.20
Curve 3: phase shift predicted by the final OTA model

This results in a model described by curve no. 3 which is a close approximation of the measured phase characteristics of the OTA.

Equation (2.20) must therefore contain, in order to provide a better approximation of the OTA, the phase correcting term of equation 2.21. Network synthesis literature describes procedures which allow the magnitude to be found with an arbitrary multiplying constant from a given phase function [9]. This procedure is applied below:

$$\theta = \tan^{-1} \frac{W}{W_n}$$

let $M = W_n$ and $N = W$

$$M + j\,N = W_n + jw$$

$$Z(jw) = (W_n + jw)\,K$$

$$|Z(jw)| = \sqrt{W_n^2 + w^2} \cdot K \qquad (2.22)$$

Since, at the moment, we wish to change only the phase predicted by equation (2.20) and keep the magnitude unaltered we must use a value of

$$K = \frac{1}{\sqrt{W_n^2 + w^2}} \qquad (2.23)$$

Therefore, the term to be included in equation 2.20 is:

$$\text{CT 1 (Compensation Term no. 1)} = \frac{W_n + jw}{\sqrt{W_n^2 + w^2}} \qquad (2.24)$$

Our model no. 1 for the open loop gain of the OTA is:

$$A_{vo_1}(w) = \left[\frac{G_m(0)\,R_\ell}{\left(\frac{jw}{W_n}\right)^2 + \left(\frac{2\sigma}{W_n}\right) jw + 1}\right] \cdot \left[\frac{W_n + jw}{\sqrt{W_n^2 + w^2}}\right] \quad \text{Model no. 1} \qquad (2.25)$$

Fig. 10 compares the measured $|A_{vo}|$ (curve no. 1) with the $|A_{vo}(w)|$ predicted by model no. 1 (equation 2.25) shown as curve no. 2. It is apparent that model no. 1 is an excellent approximation of the actual characteristics of the OTA for frequencies below 2 MHz. Above this frequency the model predicts a steeper attenuation rate compared to the measured one.

A more accurate approximation model for frequencies above 2 MHz can be obtained by selecting a value of $K = \frac{1}{W_n}$ in equation 2.22. This value of K will yield compensating term no. 2.

$$CT\ 2 = \frac{W_n + jw}{W_n} = 1 + \frac{jw}{W_n} \tag{2.26}$$

Therefore our model no. 2 for the open loop gain of the OTA is:

$$A_{vo}(w) = \left[\frac{G_m(0)\ R_\ell}{\left(\frac{jw}{W_n}\right)^2 + \left(\frac{2\sigma}{W_n}\right) jw + 1}\right] \cdot \left[\frac{W_n + jw}{W_n}\right] \qquad \text{Model no. 2} \quad (2,27)$$

The $|A_{vo}(w)|$ is also shown in Fig. 3 as curve no. 3. It is apparent that for frequencies below 2 MHz, model no. 1 is a more accurate model; whereas over 2 MHz, model no. 2 offers a better approximation of the OTA magnitude characteristics.

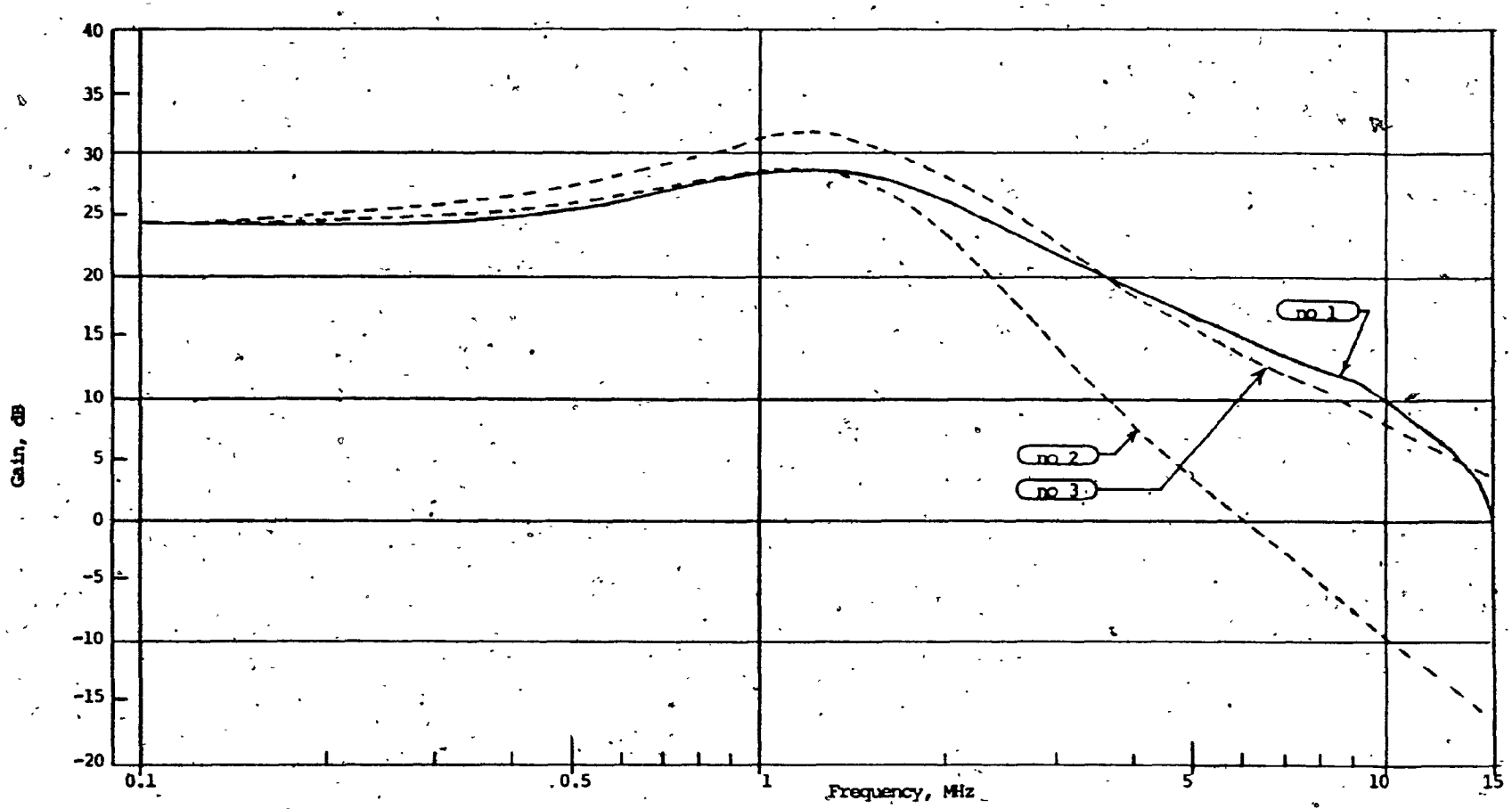

Figure 10: Comparison of the models and measured open loop gain of the 3080 OTA

Curve 1: measured open loop gain of the OTA
Curve 2: open loop gain predicted by model no 1 (equation 2.25)
Curve 3: open loop gain predicted by model no 2 (equation 2.27)

Finally, equations (2.25), (2.27), (2.18), (2.19), (2.7) and (2.4), give us the information to write a model for $G_m(w)$.

Model no. 1

$$G_m(w) = \left[\frac{19 \cdot I_{abc} \cdot CF}{\left(\frac{jw}{W_n}\right)^2 + \left(\frac{2\sigma}{W_n}\right) jw + 1}\right] \cdot \left[\frac{w_n + jw}{\sqrt{w_n^2 + w^2}}\right] \tag{2.28}$$

Model no. 2

$$G_m(w) = \left[\frac{19 \cdot I_{abc} \cdot CF}{\left(\frac{jw}{W_n}\right)^2 + \left(\frac{2\sigma}{W_n}\right) jw + 1}\right] \cdot \left[\frac{w_n + jw}{W_n}\right] \tag{2.29}$$

where: $w_n = 8.54 \cdot 10^6$ rad/sec; $\sigma = 0.33$

CHAPTER 3

INVESTIGATING THE USE OF THE 3080 OTA AS AN INDUCTANCE SIMULATOR

3.1 General

Gyrators are two port devices whose terminals characteristics are described by the admittance matrix:

$$[y] = \begin{bmatrix} 0 & G_1 \\ -G_2 & 0 \end{bmatrix} \tag{3.1}$$

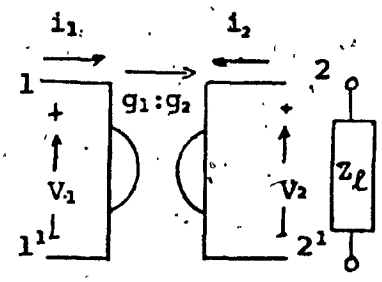

Figure 11: Gyrator

If the load applied to the second port of the gyrator is a capacitor (ie: $Z_\ell = \frac{1}{SC}$), then from eq. 3.1, we can write:

$$I_1 = -G_1 V_2 = -G_1 \left(\frac{-I_2}{SC}\right) = \frac{G_1 G_2 V_1}{SC}$$

hence: $$Z_i = \frac{V_1}{I_1} = \frac{SC}{G_1 G_2} \tag{3.2}$$

Therefore, a gyrator which is terminated with a capacitative load exhibits an inductive load at the other port.

The admittance matrix of eq. 3.1 can be rewritten as follows:

$$[y] = \begin{bmatrix} 0 & +G_1 \\ -G_2 & 0 \end{bmatrix} = \begin{bmatrix} 0 & +G_1 \\ 0 & 0 \end{bmatrix} + \begin{bmatrix} 0 & 0 \\ -G_2 & 0 \end{bmatrix} \qquad (3.3)$$

The two right-hand side matrices represent two ideal voltage controlled current sources (VCVS). The first VCCS having a positive transconductance and the second a negative transconductance. Thus, from eq. 3.3 we can see that a gyrator can be realized as a parallel and back-to-back connections of two voltage controlled current sources. This type of configuration is depicted in Fig. 12.

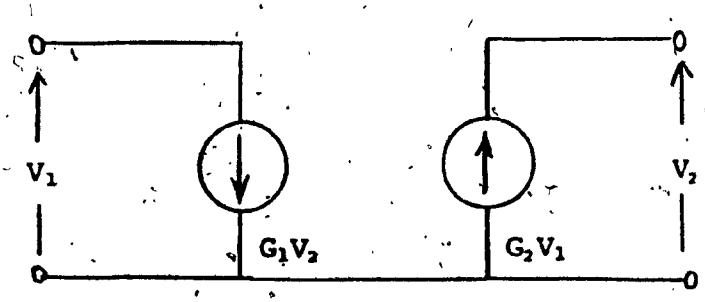

Figure 12: VCCS configurations for gyrator realization

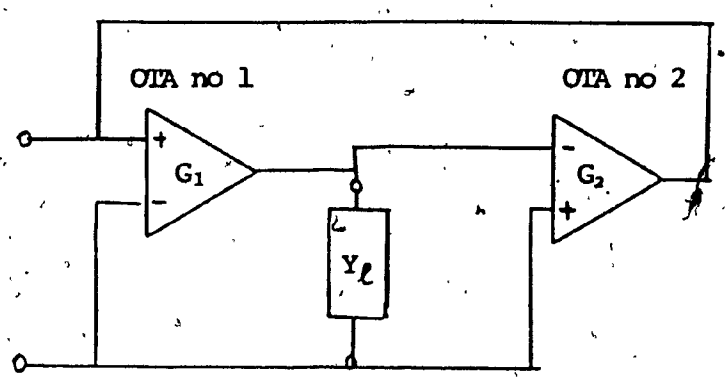

Figure 13: A gyrator realization using two OTAs

Since the OTA is basically a VCCS, using two OTA units in a similar configuration, as shown in Fig. 13, we should be able to construct a gyrator circuit. By terminating this gyrator with a capacitor, we can then obtain an inductance simulator.

3.2 Objectives

The objectives of this chapter are:

(a) To derive a model for the gyrator circuit of Fig. no. 13, taking into consideration the finite input and output resistance of the OTA and the transconductance model derived in chapter 2. This derivation is to focus on the use of the circuit as an inductance simulator.

(b) To test the model.

3.3 The indefinite admittance matrix of the OTA $[y_{iam}]$

The indefinite admittance matrix of the OTA of Fig. no. 14 can be derived using standard network analysis techniques [10].

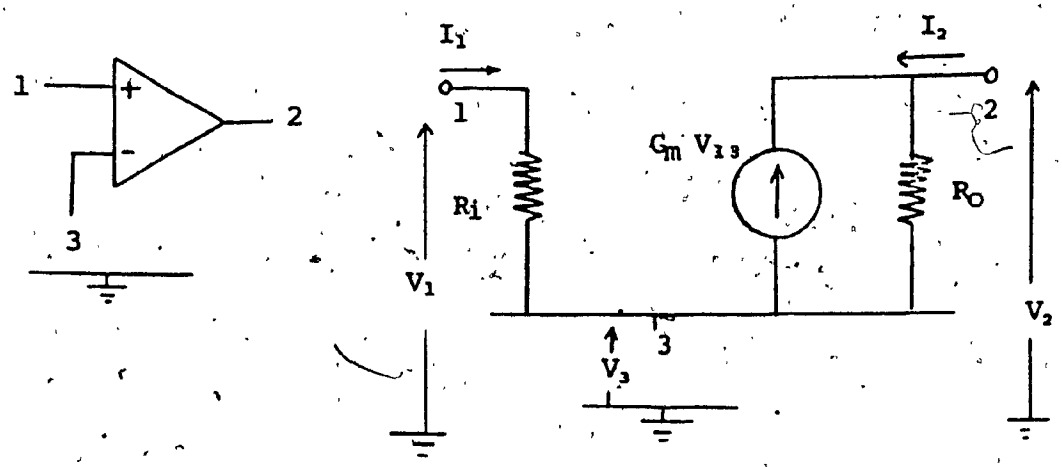

Figure 14: OTA model with finite input and output resistances

$$[y_{iam}] = \begin{bmatrix} 1/R_i & 0 & -1/R_i \\ -G_m & 1/R_0 & G_m - 1/R_0 \\ +G_m - 1/R_i & -1/R_0 & 1/R_i - G_m + 1/R_0 \end{bmatrix} \tag{3.4}$$

If terminal no. 1 were connected to the inverting input and terminal no. 3 to the non-inverting input, the resultant indefinite admittance matrix would be similar to equation 3.4 with the exception of having opposite signs in front of the transconductance. If the OTA were to be an ideal VCCS, R_i and R_0 would have to be infinite and G_m would have to be frequency independent.

3.4 A circuit for inductance simulation

Fig. 13 is redrawn for convenience into Fig. 15, in which Y_ℓ (the terminating load for the gyrator) is given by the parallel combination of a capacitor (C) and admittance (G_ℓ). I_1, G_{m_1}, R_{i_1}, R_{O_1} and I_2, G_{m_2}, R_{i_2}, R_{O_2} represent respectively the bias current, transconductance, input resistance, output resistance of OTA no. 1 and OTA no. 2.

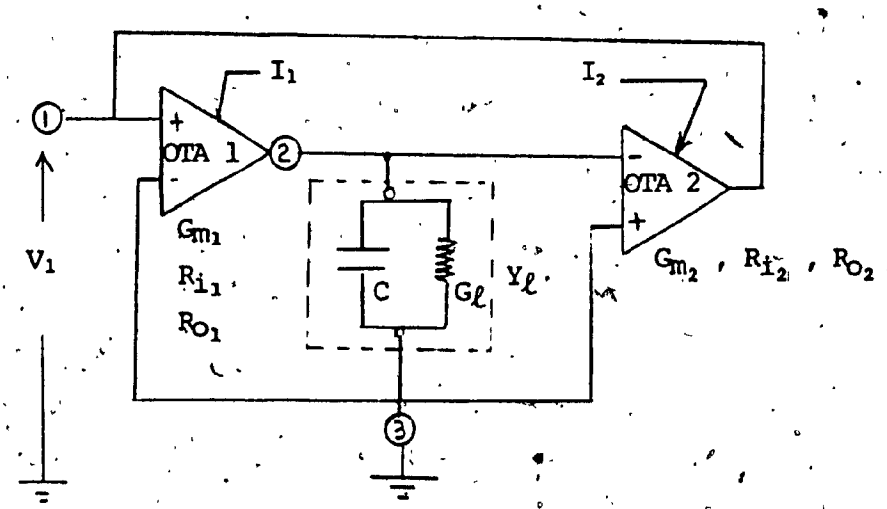

Figure 15: A circuit for inductance simulation

After having derived the combined indefinite admittance matrix for the circuit of Fig. no. 15 and having grounded node no. 3, we obtain the following nodal admittance matrix.

$$[y] = \begin{bmatrix} 1/R_{i_1} + 1/R_{O_2} & G_{m_2} \\ -G_{m_1} & y_\ell + 1/R_{O_1} + 1/R_{i_2} \end{bmatrix} \tag{3.5}$$

Hence: $y_{11} = 1/R_{i_1} + 1/R_{0_2}$ (3.6)

$y_{12} = G_{m_2}$ (3.7)

$y_{21} = -G_{m_1}$ (3.8)

$y_{22} = y_\ell + 1/R_{0_1} + 1/R_{i_2}$ (3.9)

The input impedance Z_i can be expressed in terms of equations 3.6, 3.7, 3.8 and 3.9.

$$Z_i = \left[\frac{y_{22}}{y_{11}\, y_{22} - y_{12}\, y_{21}}\right] \tag{3.10}$$

$$= \left[\frac{1}{y_{11} - \frac{y_{12}\, y_{21}}{y_{22}}}\right] = \frac{1}{y_A + y_B} \tag{3.11}$$

where $y_A = y_{11}$ (3.12)

and $y_B = \left[\frac{-y_{12}\, y_{21}}{y_{22}}\right]$ (3.13)

$y_A = y_{11} = 1/R_{i_1} + 1/R_{0_2}$ (3.14)

From 3.11 and 3.14 we can see that Z_i can be represented by a parallel combination of y_A and y_B. y_A can be represented by a parallel combination of R_{i_1} and R_{O_2}. This is shown in Fig. 16.

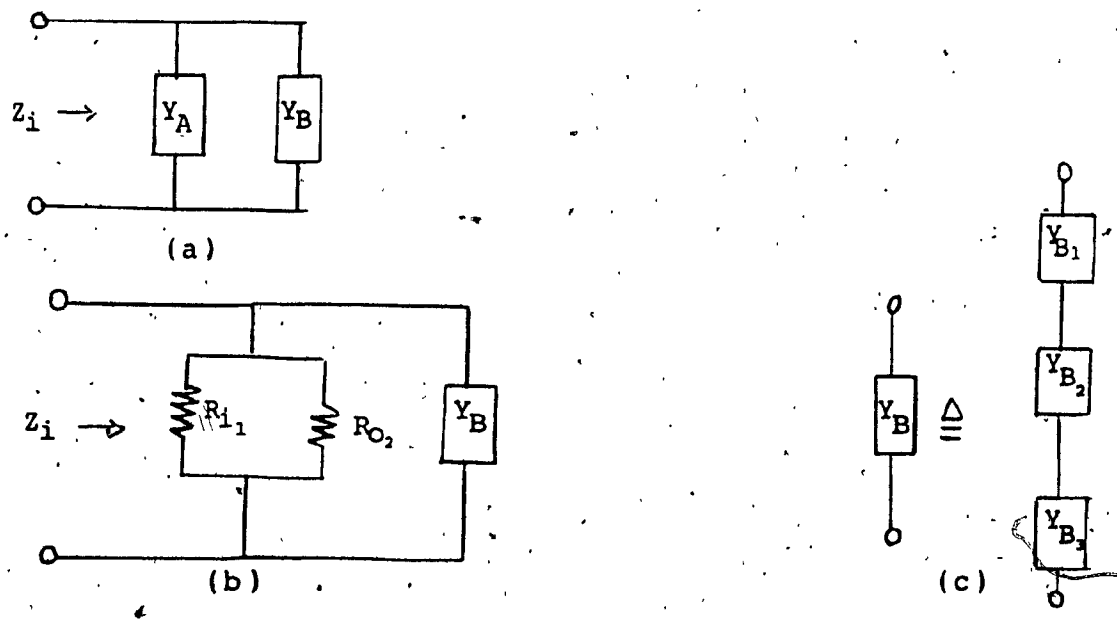

Figure 16: Equivalent circuits for equation 3.11

From 3.13, 3.7, 3.8 and 3.9 we have:

$$y_B = -\frac{y_{12}y_{21}}{y_{22}} \doteq \left[\frac{G_{m_1}\ G_{m_2}}{y_\ell + 1/R_{O_1} + 1/R_{i_2}}\right] \tag{3.15}$$

$$\frac{1}{y_B} = \frac{y_\ell}{G_{m_1}\ G_{m_2}} + \frac{1}{R_{O_1}\ G_{m_1}\ G_{m_2}} + \frac{1}{R_{i_2}\ G_{m_1}\ G_{m_2}} \tag{3.16}$$

We define:

$$y_{B_1} = \frac{G_{m_1} \; G_{m_2}}{Y_\ell} \tag{3.17}$$

$$yB_2 = G_{m_1} \; G_{m_2} \; R_{0_1} \tag{3.18}$$

$$yB_3 = G_{m_1} \; G_{m_2} \; R_{i_2} \tag{3.19}$$

Hence, $1/yB = 1/yB_1 + 1/yB_2 + 1/yB_3$ (3.20)

We can therefore represent yB in Fig. 16 as a series connection of yB_1, yB_2 and yB_3.

Our next task will be to synthesize these three admittances. We will assume in our derivation that the frequencies of operation of the inductor simulator will be much less than the cut off (natural) frequency of the OTAs. (ie: Assume $W_n >> w$).

Therefore, equation 2.24 and 2.27 (CT1 and CT2) reduce to:

$$CT1 = CT2 \simeq \left[\frac{W_n + jw}{W_n}\right] \tag{3.21}$$

Hence equation 2.28 and 2.29 (model 1 and 2) for $G_m(w)$ are identical and equal to:

$$G_m(w) \simeq \left[\frac{G_m(0)}{\frac{2\sigma}{W_n}(jw) + 1}\right] \cdot \left[\frac{W_n + jw}{W_n}\right] \tag{3.22}$$

and

$$G_{m_1}(w) \; G_{m_2}(w) \cong G_{m_1}(0) \; G_{m_2}(0) \left[\frac{jw + w_n}{2\sigma \; jw + w_n}\right]^2$$

$$\cong G_{m_1}(0) \; G_{m_2}(0) \left[\frac{w_n + 2jw}{w_n + 4\sigma \; jw}\right] \tag{3.23}$$

Thus

$$yB_2(s) = R_{0_1}\ G_{m_1}(0)\ G_{m_2}(0) \left[\frac{W_n + 2s}{W_n + 4\sigma\ s}\right] \tag{3.24}$$

$$\text{let } K_2 = R_{0_1}\ G_{m_1}(0)\ G_{m_2}(0) \tag{3.25}$$

From 3.24 we can write

$$y_{B_2}(s) = \left[\frac{K_2}{1 + \frac{4\sigma}{W_n} s}\right] + \left[\frac{\frac{2}{W_n} K_2\ s}{1 + \frac{4\sigma}{W_n} s}\right] \tag{3.26}$$

$$yB_2(s) = yB_2x(s) + yB_2y(s) \tag{3.27}$$

$yB_2(s)$ can be synthesized using a parallel connection of $yB_2x(s)$ and $yB_2y(s)$.

$yB_2x(s)$ can be synthesized using a series RL circuit (R_2x, L_2x) in which:

$$R_2x = \frac{1}{K_2} \tag{3.28}$$

$$L_2x = \frac{4\sigma}{W_n\ K_2} \tag{3.29}$$

$yB_2y(s)$ can be synthesized using a series RC (R_2y, C_2y) in which:

$$R_2y = \frac{2\sigma}{K_2} \tag{3.30}$$

$$C_2y = \frac{2\ K_2}{W_n} \tag{3.31}$$

Let us define: $K_3 = G_{m_1}(0)\ G_{m_2}(0)\ R_{i_2}$ (3.32)

Using the same procedure outline above for the realization of $yB_2(s)$, we can also realize $yB_3(s)$ which will have the same circuit configuration of $yB_2(s)$.

The equivalent expressions for equations 3.28, 3.29, 3.30 and 3.31 will contain, in the case of $yB_3(s)$, the term K_3 in place of K_2.

Thus, $yB_3(s)$ can be realized by a parallel combination of a series RL circuit (R_3x, L_3x) and series RC circuit (R_3y, C_3y) for which:

$$R_3x = \frac{1}{K_3} \tag{3.33}$$

$$L_3x = \frac{4\sigma}{W_n K_3} \tag{3.34}$$

$$R_3y = \frac{2\sigma}{K_3} \tag{3.35}$$

$$C_3y = \frac{2 K_3}{W_n} \tag{3.36}$$

We can now redraw Fig. 16, taking into consideration the realization of $yB_2(s)$ and $yB_3(s)$. This is done in Fig. 17. $yB_1(s)$ is still to be synthesized.

$$\text{Let } ZB_1(s) = \frac{1}{yB_1(s)} \tag{3.37}$$

then, from (3.17) and (3.23) we can write:

$$ZB_1(s) = \frac{y_\ell}{G_{m_1}(0)\ G_{m_2}(0)} \cdot \left[\frac{W_n + 4\sigma s}{W_n + 2 s}\right] \tag{3.38}$$

y_ℓ shown in Fig. 15 is given by the parallel combination of C and G_ℓ;

$$\text{thus } y_\ell = SC + G_\ell \tag{3.39}$$

let, $K_1 = G_{m_1}(0)\ G_{m_2}(0)$ (3.40)

Using 3.39 and 3.40 in 3.38 and performing the algebraic division we arrive at:

$$ZB_1(s) = S\ \frac{2\sigma\ C}{K_1} + \frac{S\ [C\ w_n\ (1-2\ \sigma) + 4\sigma\ G_\ell] + G_\ell\ W_n}{2\ K_1\ S + K_1\ W_n} \qquad (3.41)$$

3.41 can be rewritten as a summation of three terms.

$$ZB_1(s) = S\ (2\sigma\ C\ K_0) + K_0\ \frac{S\left[C\ (1-2\ \sigma) + \frac{4\sigma\ G_\ell}{W_n}\right]}{\frac{2}{W_n}\ S + 1} + \frac{K_0\ G_\ell}{\frac{2}{W_n}\ S + 1} \qquad (3.42)$$

where $K_0 = \frac{1}{K_1}$ (3.43)

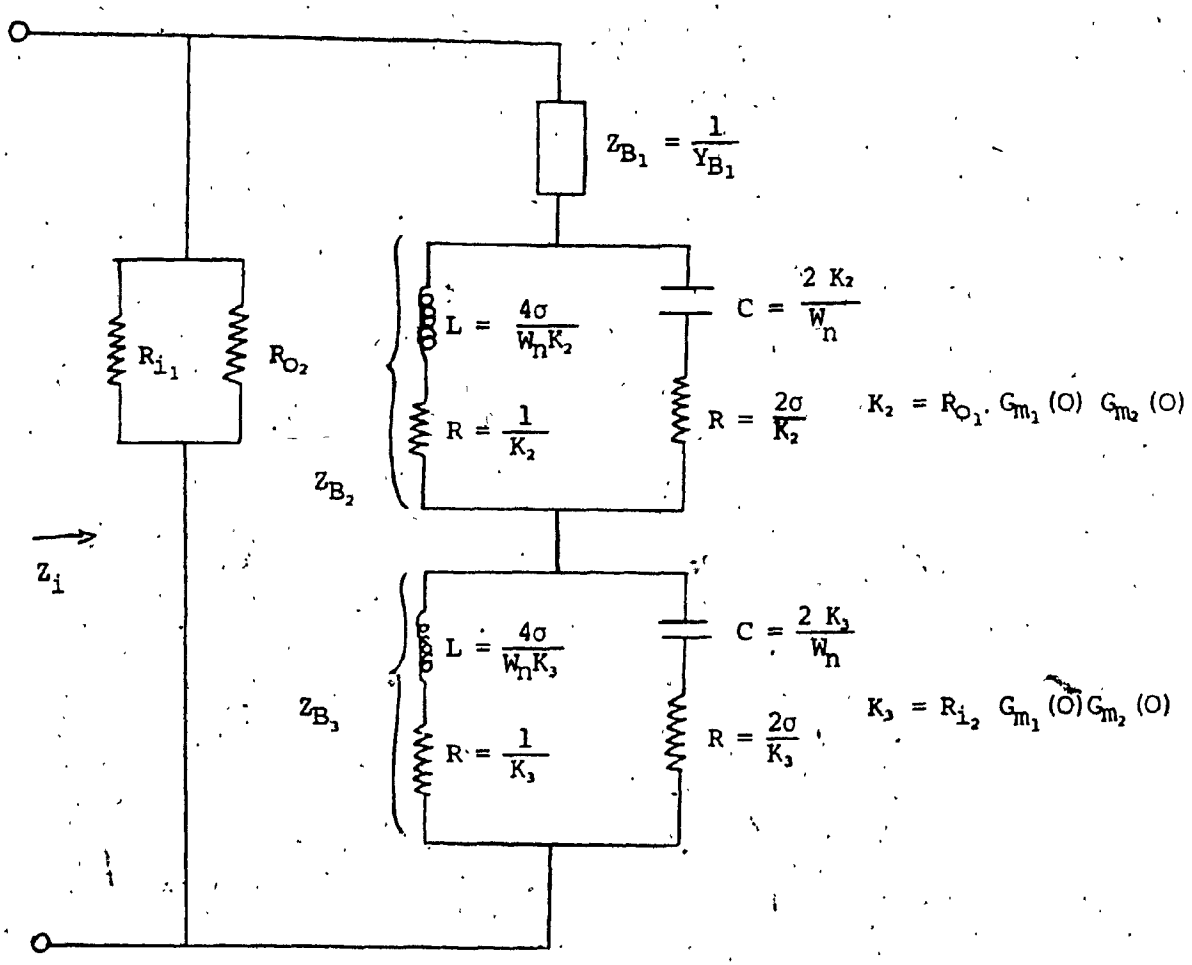

Figure 17: A model for the inductance simulator circuit

From 3.42, we see that $ZB_1(s)$ can be realized as a series combination of:

(a) an inductance: $L_0 = 2\sigma C K_0$ (3.44)

(b) a parallel RL combination $(R_0^1 L_0^1)$ in which:

$$L_0^1 = \left[C(1-2\sigma) + \frac{4\sigma G_\ell}{W_n}\right] K_0 \tag{3.45}$$

$$R_0^1 = L_0^1 \frac{W_n}{2} \frac{W_n}{2} \tag{3.46}$$

(c) a parallel RC combination $(R_0^{11} C_0^{11})$ in which

$$R_0^{11} = K_0 G_\ell \tag{3.47}$$

$$C_0^{11} = \frac{2}{W_n K_0 G_\ell} \tag{3.48}$$

The entire realization for yB_1 is shown in Fig. no. 18.

A final model can now be obtained by adding the realization for yB_1 into Fig. 17. However a simpler model will result if ZB_2 and ZB_3 of Fig. 17 are combined. This simplification is detailed in Appendix VI. The resultant impedance (Z_E) can be written as:

$$Z_E = Z_{B_2} + Z_{B_3} \simeq \frac{K_T \frac{8\sigma}{W_n} s}{\left[\frac{2+4\sigma}{W_n}\right] S + 1} + \frac{K_T}{\left[\frac{2+4\sigma}{W_n}\right] S + 1} \tag{3.49}$$

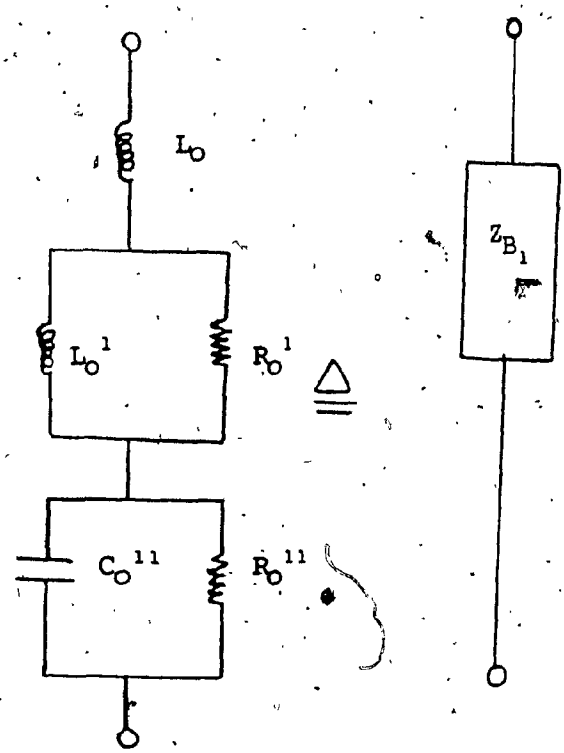

Figure 18: A realization for Z_{B_1}

$$Z_{B_1} = \frac{1}{yB_1}$$

$$K_0 = \frac{1}{K_1} = \frac{1}{G_{m_1}(0)\, G_{m_2}(0)}$$

$$L_0 = 2\sigma\, C\, K_0$$

$$L_0^1 = \left[C(1-2\,\sigma) + \frac{4\sigma\, G_\ell}{W_n}\right] K_0$$

$$R_0^1 = L_0^1 \cdot \frac{W_n}{2}$$

$$R_0^{11} = K_0 \cdot G_\ell$$

$$C_0^{11} = \frac{2}{W_n\, K_0\, G_\ell}$$

where $K_T = \frac{1}{K_2} + \frac{1}{K_3}$ (3.50)

Equation 3.49 can be realized by a series connection of:

(a) a parallel RC combination (R_{ec} C_e) with:

$$R_{ec} = K_T \tag{3.51}$$

$$C_e = \left[\frac{2 + 4\sigma}{W_n}\right] \frac{1}{K_T} \tag{3.52}$$

(b) a parallel RL combination (R_{el}, L_e) with:

$$R_{e\ell} = K_T \left[\frac{8\sigma}{2 + 4\sigma}\right] \tag{3.53}$$

$$L_e = K_T \frac{8\sigma}{W_n} \tag{3.54}$$

Fig. 19 shows the realization of Z_E.

Fig. 20 shows the final model of the inductor simulator circuit.

3.5 Numerical Values for the Components of the Model

In order to obtain the values of all components of the model, it is necessary to have also values for the input and output resistances of the OTAs. These can be obtained from the manufacturers' specifications [1] and they are reported in Fig. 21.

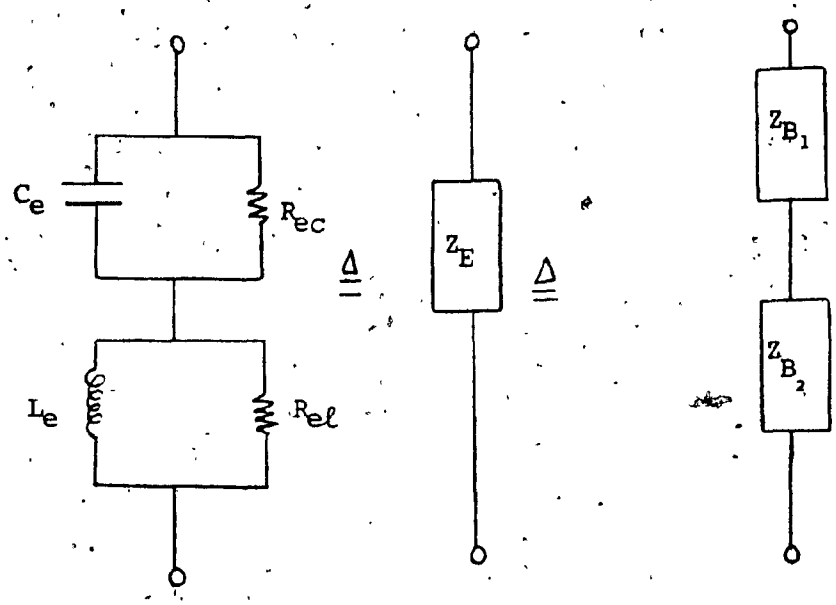

Figure 19: Combining Z_{B_1} and Z_{B_2} (Figure 17)

$$R_{ec} = K_T$$

$$C_e = \left[\frac{2 + 4\sigma}{W_n}\right] \frac{1}{K_T}$$

$$R_{e\ell} = K_T \left[\frac{8\sigma}{2 + 4\sigma}\right]$$

$$L_e = K_T \frac{8\sigma}{W_n}$$

$$K_T = \frac{1}{K_1} + \frac{1}{K_2}$$

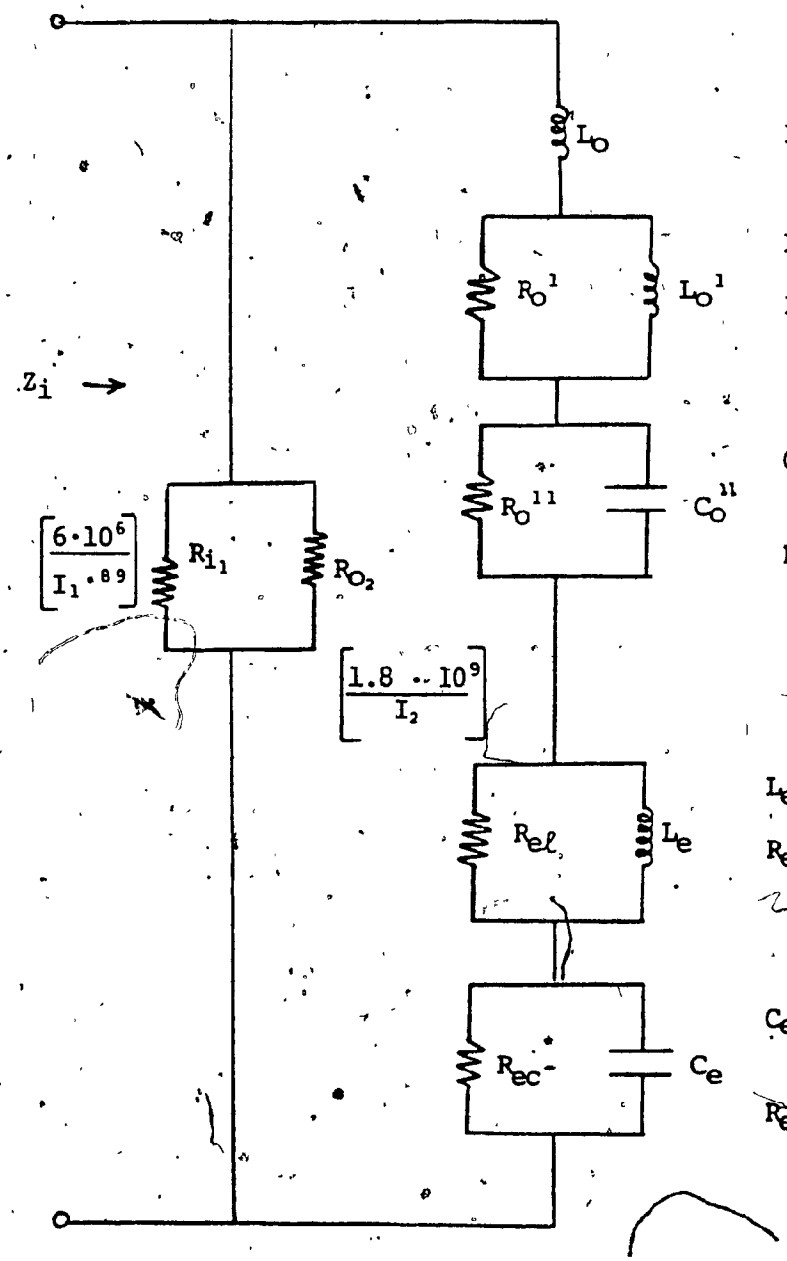

$L_o = 0.62\ K_o C$

$L_o^1 = (0.38C + 0.14 \cdot 10^{-6} G\ell) K_o$

$R_o^1 = (1.6 \cdot 10^6 C + 0.6 G\ell) K_o$

$C_o^{11} = \frac{2.3 \cdot 10^{-7}}{K_o\ G\ell}$

$R_o^{11} = K_o\ G\ell$

$L_e = 3 \cdot 10^{-7}\ K_T$

$R_{e\ell} = 0.76\ K_T$

$C_e = \frac{3.8 \cdot 10^{-7}}{K_T}$

$R_{ec} = K_T$

$$K_T = \left[\frac{1.53}{I_2} + \frac{461}{I_1 I_2 \cdot 11}\right] \frac{1}{(CF1)\ (CF2)}$$

$$K_o = \left[\frac{2770 \cdot 10^6}{I_1 I_2 (CF1)\ (CF2)}\right]$$

I_1, I_2 are expressed in μA

Figure 20: The final model of the inductance simulator circuit

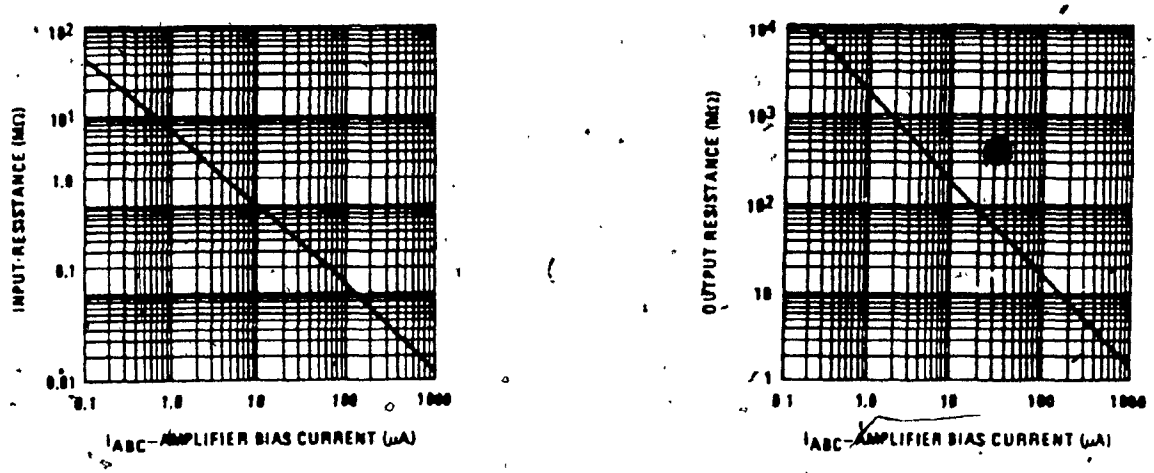

Figure 21: Input and output resistances of the OTA

As can be seen from Fig. 21, values of input and output resistances are dependent on the bias current. In the log-log graph both (R_0 And R_i, vs. I_{abc}) exhibit a straight line characteristics. Therefore, they will have the form $R = BI^{\beta}$, with B and β as constant. B can be found from the value of the ordinate when the abscissa is equal to one, and β can be determined from the slope of the line. β is given by the ratio of the total linear length along the ordinate axis for a decade change in the bias current, divided by the linear length of one decade change in resistance.

We obtain:

$$R_{i_1} = \frac{6 \cdot 10^6}{(I_1)^{.89}} \tag{3.55}$$

$$R_{i_2} = \frac{6 \cdot 10^6}{(I_2)^{.89}} \tag{3.56}$$

$$R_{0_1} = \frac{1.8 \cdot 10^9}{I_1} \tag{3.57}$$

$$R_{0_2} = \frac{1.8 \cdot 10^9}{I_2} \tag{3.58}$$

Using numerical values for W_n, σ (2.18a and 2.18b); $G_{m_1}(0)$, $G_{m_2}(0)$ (2.4); R_{i_1}, R_{i_2}, R_{0_1}, R_{0_2} (3.55, 3.56, 3.57, 3.58) we can find values for all the components of the model.

Fig. 20 lists all the components values. Notice that each component can be expressed in terms of the bias current of OTA no. 1 or OTA no. 2, the terminating capacitor (C) and its parallel connected conductance (G_ℓ).

3.6 An Approximation of the Model of Fig. 20

A further simplification of the model presented in Fig. 20 can be obtained by recognizing the validity of the following approximations which are based on the numerical values of the components for frequencies of operation within 100 KHz.

(a) $R_0^1 // L_0^1 \cong L_0^1$

(b) $R_0^{11} // C_0^{11} \cong R_0^{11}$

(c) $R_{e\ell} // L_e \cong L_e$ and $L_0 + L_e \cong L_0$

(d) $R_{ec} // C_e \cong R_{ec}$

Using these approximations, we can simplify the model of Fig. 20, as shown in Fig. 22.

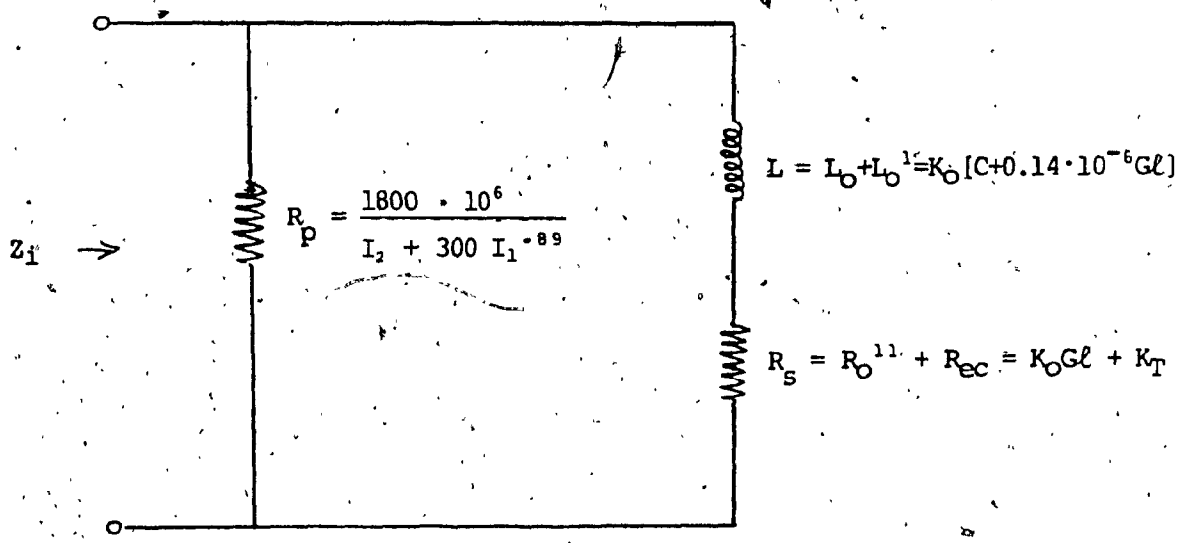

Figure 22: A simplified model of the inductance simulator circuit

3.7.1 Dynamic Range of the Model

The dynamic range of the model is the range of voltages over which the inductor simulator circuit (Fig. 15) behaves linearly. This is related to the dynamic range over which the two OTAs are linear. Specifically, whenever one of the two OTAs begins to operate with a non-linear transconductance value, the circuit starts to operate outside of the dynamic range.

For the circuit to operate within the dynamic range the following equations must be satisfied:

(a) $V_1 \leq \pm 25$ mV (3.59)

(b) $V_2 \leq \pm 25$ mV (3.60)

For circuit operation within the linear region the model of Fig. 20 applies.

For circuit operation outside of the linear region, the model can predict qualitatively the behaviour of the circuit by examining the effects that the two correcting factors (CF_1, CF_2) will have on the value of the simulated inductance and its quality factor.

3.7.2 Limitations of Realizable Simulations

A better insight into the limitations imposed by equations (3.59) and (3.60) can be obtained by introducing the definition of three terms: the theoretical inductance (L_t) range, the useful inductance (L_u) range, the useful quality factor (Q_u) range.

Theoretical Inductance (L_t) Range

The simulated inductance is proportional to the value of K_0. Within the linear region:

$$K_0 = \frac{2770 \cdot 10^6}{I_1 \quad I_2}$$

Since I_1 and I_2 can each be varied over a range of 1 to 1000, the value of K_0 and hence the value of simulated inductance, can be programmed over a range of 1 to 1,000,000. Thus the theoretical range of values of simulated inductances for a given terminating capacitance and admittance is:

Theoretical range of L is: $L_{min} \leq L_t \leq L_{max}$ where

$$L_{max} = 2770 \cdot 10^6 \; [C + 0.14 \cdot 10^{-6} \; G_\ell]$$

$$L_{min} = 2770 \quad [C + 0.14 \cdot 10^{-6} \; G_\ell]$$

Useful Inductance (L_u) Range

We define the useful range of L (L_u) as those simulated inductance values which are within the programmable range and which also comply with the limitations set by R_p and the linear dynamic range of the circuit. Values of inductances which are within the useful range satisfy the following equations.

$$[W_h^2 L_u^2 + (R_s)^2]^{\frac{1}{2}} << R_p \tag{3.61}$$

where: $W_h = 6.28 \cdot$(highest frequency of interest)

$$\frac{(G_{m_1}) V_1}{[(W_\ell C)^2 + (G_\ell + 1/R_{O_1} + R_{i_2})^2]^{\frac{1}{2}}} \leq 50 \cdot 10^{-3} (V_{pp}) \tag{3.62}$$

$W_\ell = 6.28 \cdot$(lowest frequency of interest)

Useful Quality Factor (Q_u) Range

We define the useful quality factors (Q_u) as the range of quality factors which are obtainable using L_u and which allow operation within the linear range of the gyrator circuit.

$$Q_u = \frac{W L_u}{R_s} \tag{3.63}$$

At the input part of the gyrator simulating a quality factor Q_u, we can write:

$$V_1 = I (R_s + jw L_u) \tag{3.64}$$

where:

V_1 = voltage at input port

I = current into input port

Equation 3.64 can be rewritten as follows:

$$\frac{V_1}{I R_s} = 1 + j Q_u \tag{3.65}$$

From 3.59, we know that for linear operation $|V_1| \leq 50 \cdot 10^{-3} (V_{pp})$; thus, using 3.65 we have:

$$\frac{50 \cdot 10^{-3} (V_{pp})}{|I| \; R_s} \geq [1 + (Q_u)^2]^{\frac{1}{2}} \tag{3.66}$$

Let V_t and Z_t represent respectively the Thévenin's equivalent voltage and impedance of the circuitry present at the input port of the gyrator. Thus:

$$I = \frac{V_t}{Z_t + R_s + jWL_u} \tag{3.67}$$

For a given set of bias currents, the LHS of 3.65 reaches its minimum when $|I|$ attains a maximum value which occurs when: $X_t = -jWL_u$.

$$|I|_{max.} = \frac{V_t}{R_t + R_s} \tag{3.67}$$

Furthermore, the RHS of 3.66 reaches its maximum when:

$$Q_u = \frac{W_h L_u}{R_s} \tag{3.68}$$

Thus, the most stringent test for the inequality of 3.66 is given by:

$$\left| \frac{(50 \cdot 10^{-3})}{V_t} \cdot \frac{(R_t + R_s)}{R_s} \right| \geq \sqrt{1 + \frac{(W_h L_u)^2}{R_s}} \tag{3.69}$$

Realizable Inductance Simulations

All inductance values that are within the range of L_u, which is defined by equations 3.61, 3.62 and 3.69, are realizable simulations. It can be noticed from these equations that:

(a) larger values of V_t and higher values of W_h tend to decrease the range of L_u whereas,

(b) larger values of R_t, and higher values of W_ℓ tend to increase

the range of L_u. Furthermore, since large values of bias currents of OTA no. 1 tend to decrease the value of R_p and increase the LHS of (3.62) much more drastically than equally large values of bias currents of OTA no. 2; it is wiser to start the design of L_u with low values of I_1 and large values of I_2, rather than vice versa.

3.8 Testing the Inductance Simulator Model

A series of tests were conducted on the inductor simulator circuit, in order to assess its performance. They are listed below and their results are presented in the following pages. Detailed measurement procedures are outlined in appendix VII.

Test no. 1: Variation of simulated inductance as a function of the bias current of OTA no. 1 (L vs. I_1)

A series resonance circuit was used. I_2, $R_\ell = G_\ell^{-1}$, C, and the Q and f_0 of the circuit were kept constant. All voltages were within the linear dynamic range of the circuit.

Fig. 23.1 shows the results of this test. A close agreement between the theoretical inductance and the measured inductance is observed.

Test no. 2: Variation of simulated inductance as a function of the bias current of OTA no. 2 (L vs. I_2)

A series resonance circuit was used. I_1, R_ℓ, C and the Q and f_0 of the circuit were kept constant. All voltages were within the linear dynamic range of the circuit.

Fig. 23.2 shows the results of this test. A close agreement between the model inductance and the measured inductance was found.

Test no. 3: Variation of simulated inductance as a function of the terminating capacitance (L vs. C)

A series resonance circuit was used. I_1, I_2, R_ℓ, were kept constant; variation of Q were kept in the range 3 to 7; variation in resonance frequencies were within the range of 3.5 to 10.5 KHz. All voltages were within the linear dynamic range of the circuit.

Fig. 23.3 shows the result of this test. The agreement between the model and the measured inductance is apparent.

Test. no. 4: Simulated inductance versus frequency

A series resonance circuit was used. I_1 and I_2 were kept constant. Different values of C and R_ℓ were selected in order to produce resonance in the range 83 Hz to 107 KHz and generated quality factors which allowed linear operation of the circuit.

We defined Inductance Deviation (ID) as:

$$ID = \frac{L_{measured} - L_{model}}{L_{model}} \times 100$$

Fig. 23.4 shows the results of this test.

Most measurements showed on ID of less than 5 percent.

Test no. 5: Variation of Q with variations in G_ℓ

A series resonance circuit was used. I_1, I_2 C and the resonance frequency were kept constant. A series resistor was added to the resonance circuit in order to decrease the voltage present to the input of OTA no. 1 at the resonant frequency. This resistor allowed linear operation of the inductance simulator at values of Q for which linear operation would not, otherwise, have been possible.

Fig. 23.5 displays the results of this test. A reasonable agreement between the model and experimental data can be observed.

Test no. 6: Input resistance as a function of bias currents

The gyrator was terminated with a resistor of 100 Ω, and the capacitor C was removed. The input resistance of the circuit was then measured for various values of bias currents.

Fig. 23.6a and b present the results of this test. Model and experimental results are in close agreement.

Test no. 7: Circuit behaviour in the non-linear region

In order to assess whether the model could predict from a qualitative point of view, the circuit behaviour in the non-linear region the following test was conducted.

The gyrator was terminated with a parallel combination of a capacitor (C) a resistor (R_ℓ). Using a series resonance circuit, the resonance frequency (f_0) and the Q of the circuit were measured for different values of input voltage which exceeded the linear dynamic range of the circuit. For this circuit the model predicts the following characteristics (refer to Fig. 20, 22 and 23.7).

$$L \simeq \frac{0.066}{(CF_1)(CF_2)} \quad (H)$$

$$R_s \simeq \left[\frac{55.4}{(CF_1)(CF_2)} + 2.32\right] \quad (\Omega)$$

$$R_p >> \sqrt{(R_s)^2 + (wL)^2}$$

$$f_0 = \frac{1}{2\pi\sqrt{LC_T}}$$

$$Q_0 \simeq W_0 \frac{L}{R_s}$$

Operation outside of the linear range implies a decrease in the values of CF_1 or CF_2 (equation 2.4), thus we expect an increase in L, hence a decrease in f_0 (the series capacitor remains obviously constant throughout the test). Furthermore, since the ratio of L to R_s remains approximately constant, Q_0 should decrease due to the decrease in f_0.

The model therefore predicts that larger voltage values will produce a decrease in the resonance frequency and the Q of the circuit. Measurements confirmed this behaviour (Fig. 26.7a)

3.9 Conclusion

Two OTAs were used in our open loop mode as VCCS, in the circuit configuration shown in Fig. 13, to form a gyrator circuit.

The model for this gyrator circuit, terminated with a grounded parallel capacitor/resistor combination, was obtained and tested. Experimental measurements confirmed the validity of the model.

The simulated inductance presented at the input ports of the circuit is potentially programmable over a range of 1 to 1,000,000 and over a bandwidth of at least 100 KHz; however, these ranges are mainly limited by the restricted dynamic ranges of the two OTA, and their finite input and output impedances. The Thevenin's equivalent voltages and resistances seen by the input ports of the gyrator can also affect the realizable ranges of simulated inductances that can be obtained in practice.

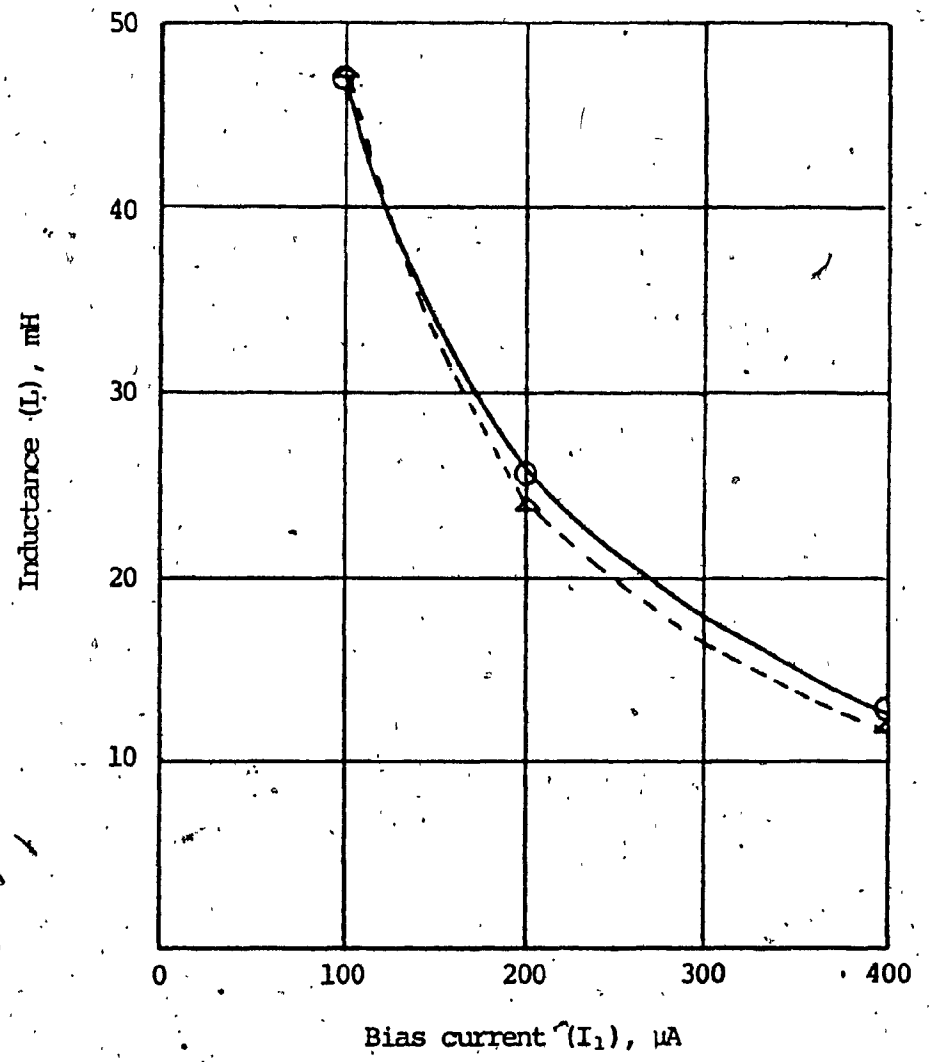

Figure 23.1: L versus I_1

measured inductance ————————
model inductance - - - - - - - - -

Test conditions: I_2 = 500
R_ℓ = 100Ω
C = 1 μF
Q_o ≃ 2.5
f_o ≃ 3.7 kHz
V_i = 10 mV_{pp}

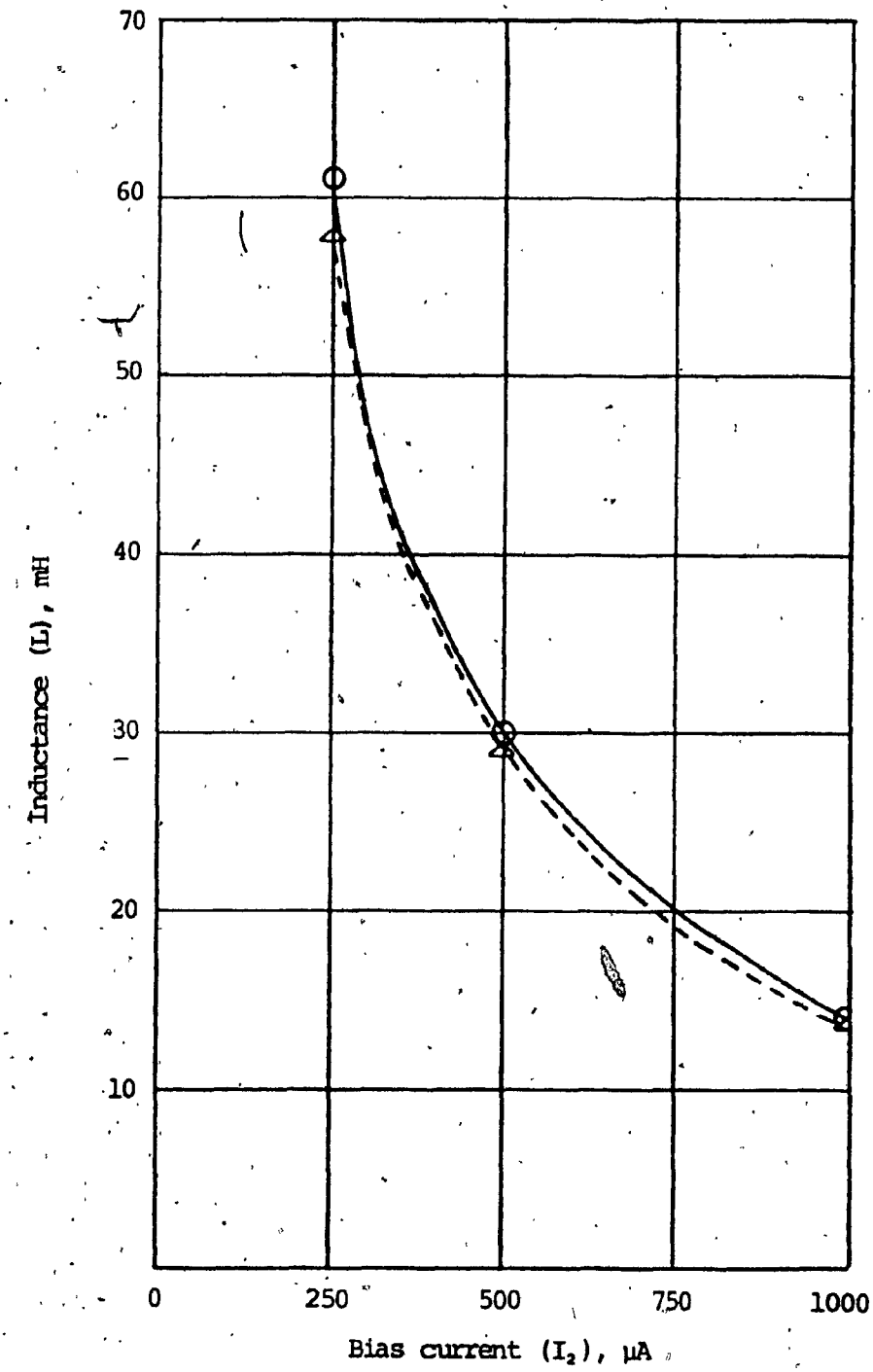

Figure 23.2: L versus I_2

measured inductance ————————
model inductance - - - - - - - - -

Test conditions: I_1 = 200 μA
R_ℓ = 100Ω
C = 1 μF
Q_o ≃ 2.5
f_o ≃ 3.5 KHz
V_i = 10 mV_{pp}

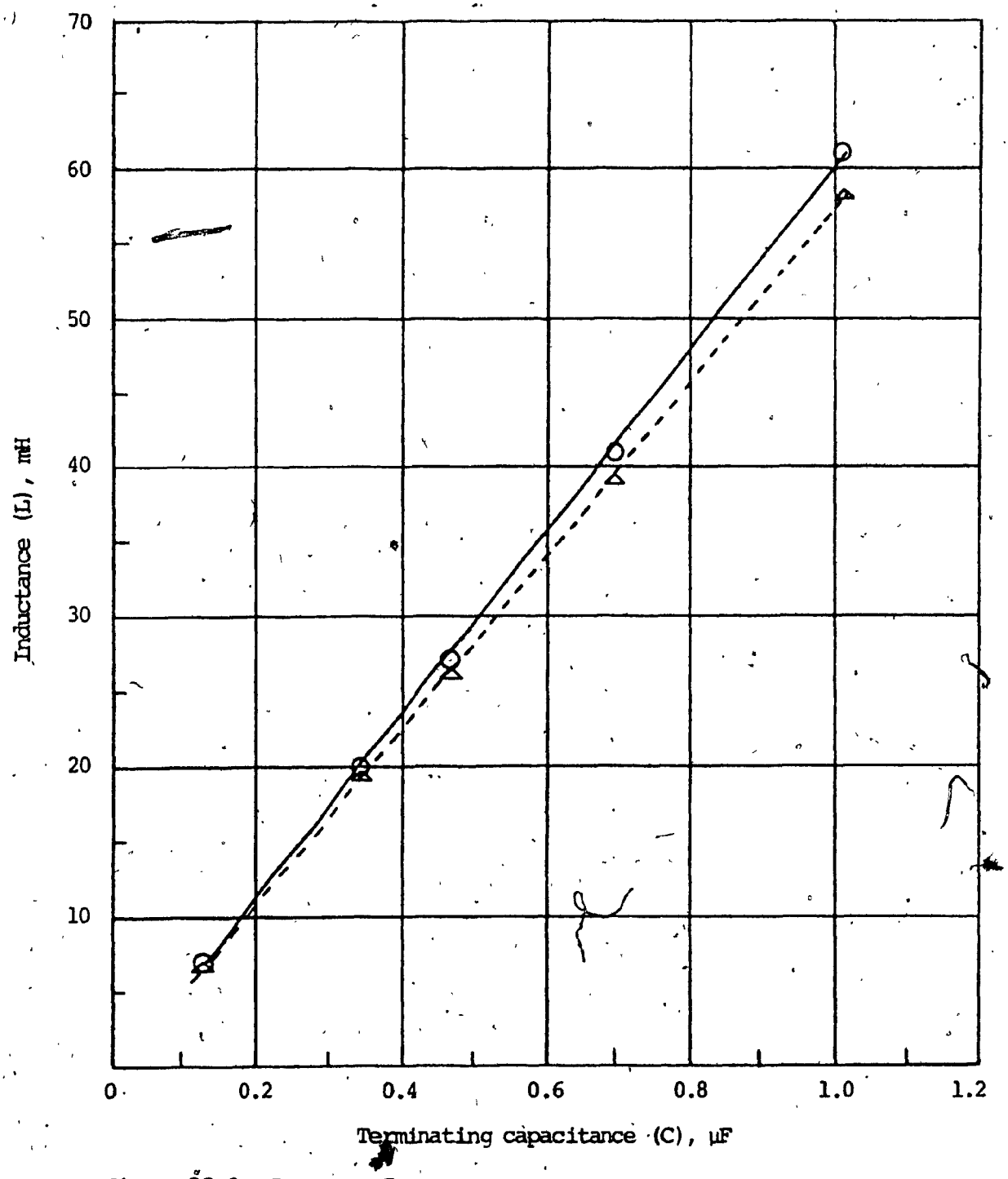

Figure 23.3: L versus C

measured inductance ————————
model inductance - - - - - - - - -

Test conditions: I_1 = 100 μA
I_2 = 500 μA
R_ℓ = 470Ω
V_i = 5 mV_{pp}

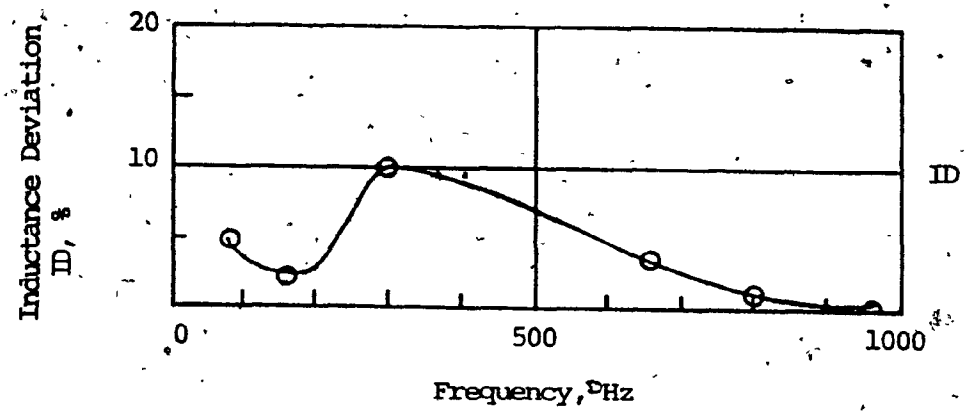

$$ID = \frac{L\ measured - L\ model}{L\ model} \times 100$$

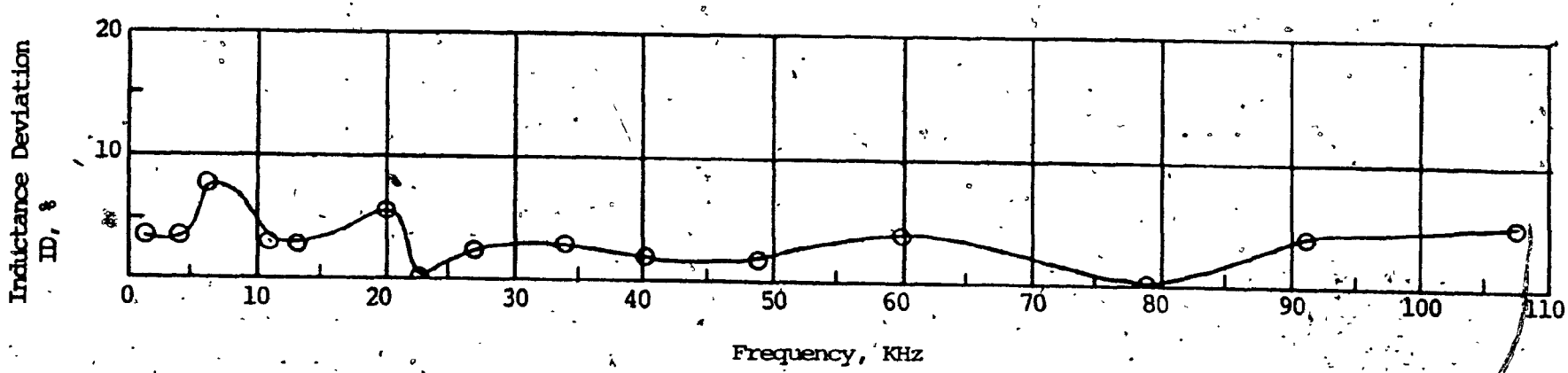

Figure 23.4: L versus f (82 Hz - 107 KHz)

Test conditions: I_1 = 100 μA
I_2 = 500 μA
R_ℓ = 470Ω; 2.7 KΩ; 10 KΩ
C = 0.01 μF; 0.1 μF; 0.33 μF; 1 μF
L = 49 mH; 6.6 mH; 19.4 mH; 58 mH

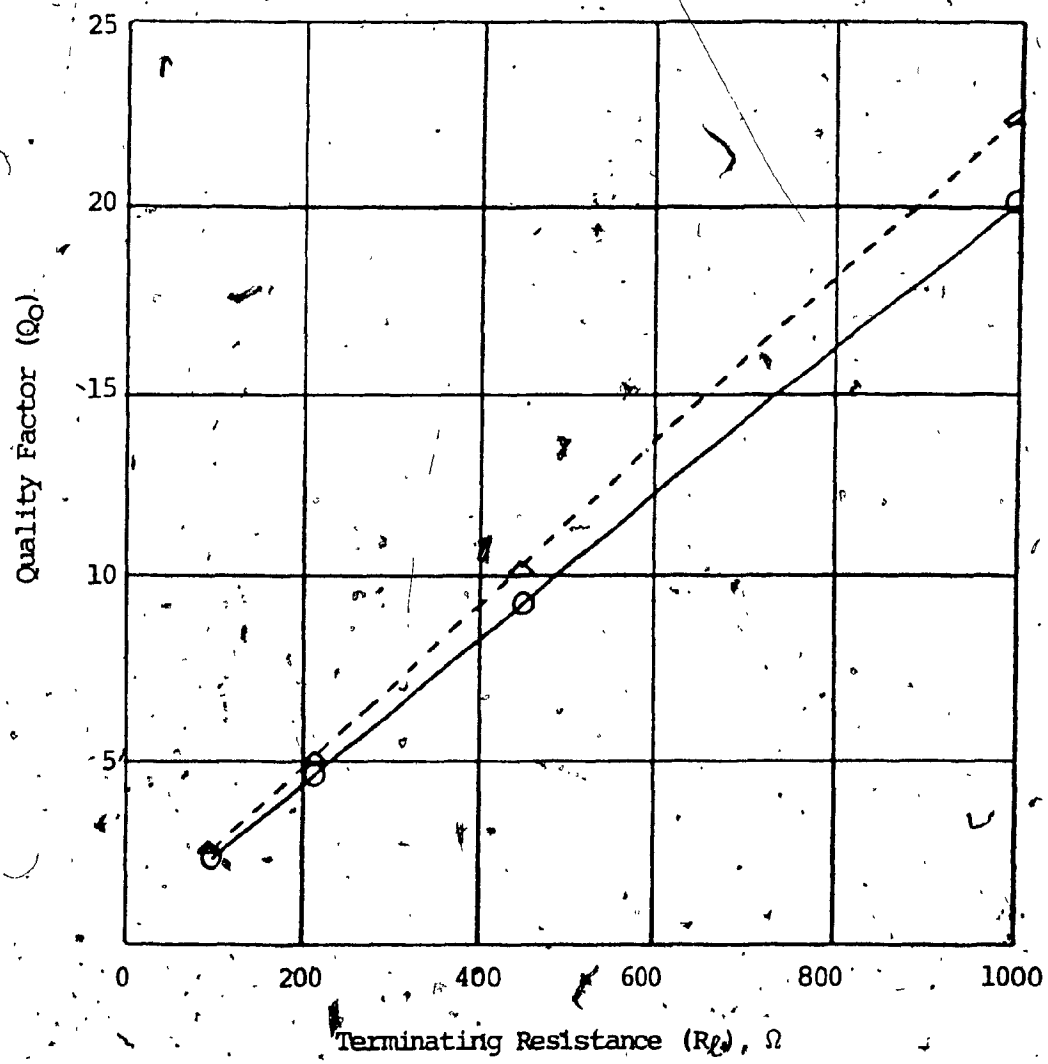

Figure 23.5: Q_o versus R_ℓ (G_ℓ^{-1})

measured Q_o ————————————

calculated Q_o (model) - - - - - - - - - -

Test conditions: I_1 = 400 μA
I_2 = 500 μA
C = 1 μF
f_o = 3.4 KHz
C_T = 0.15 μF; D.F. = $5 \cdot 10^{-3}$
V_i = 10 mV_{pp}

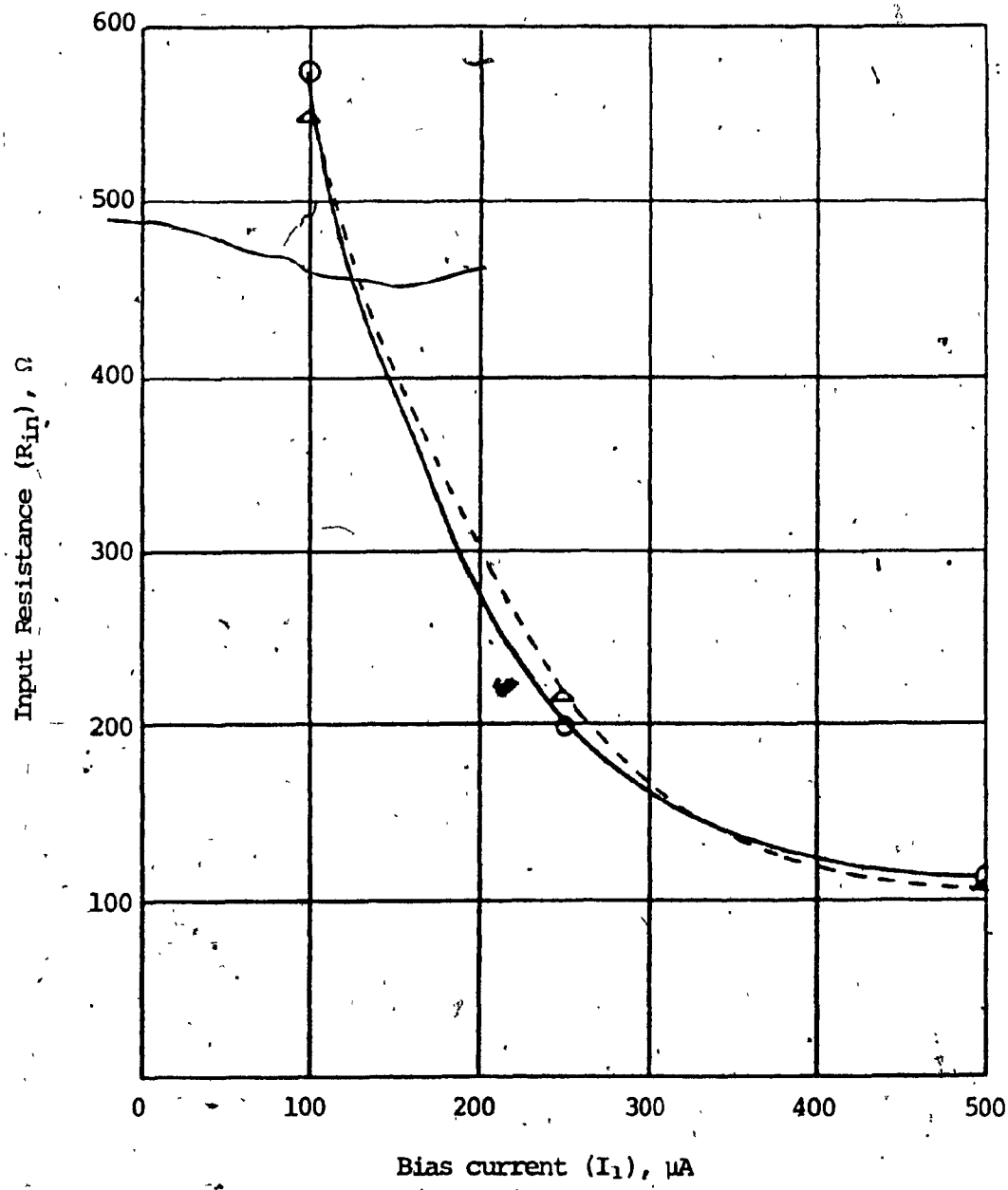

Figure 23.6 a: R_{in} versus I_1

measured R_{in} ————————

model R_{in} - - - - - - - - - -

Test conditions: I_2 = 500 μA
R_ℓ = 100Ω
V_i = 50 mV_{pp}

Tests were conducted at a frequency of 10 KHz. For the combination of I_1 = 500 μA, I_2 = 500 μA, R_ℓ = 100Ω, measurements were taken in the frequency range of 10 Hz to 100 KHz. R_{in} was found to be independent of the test frequency.

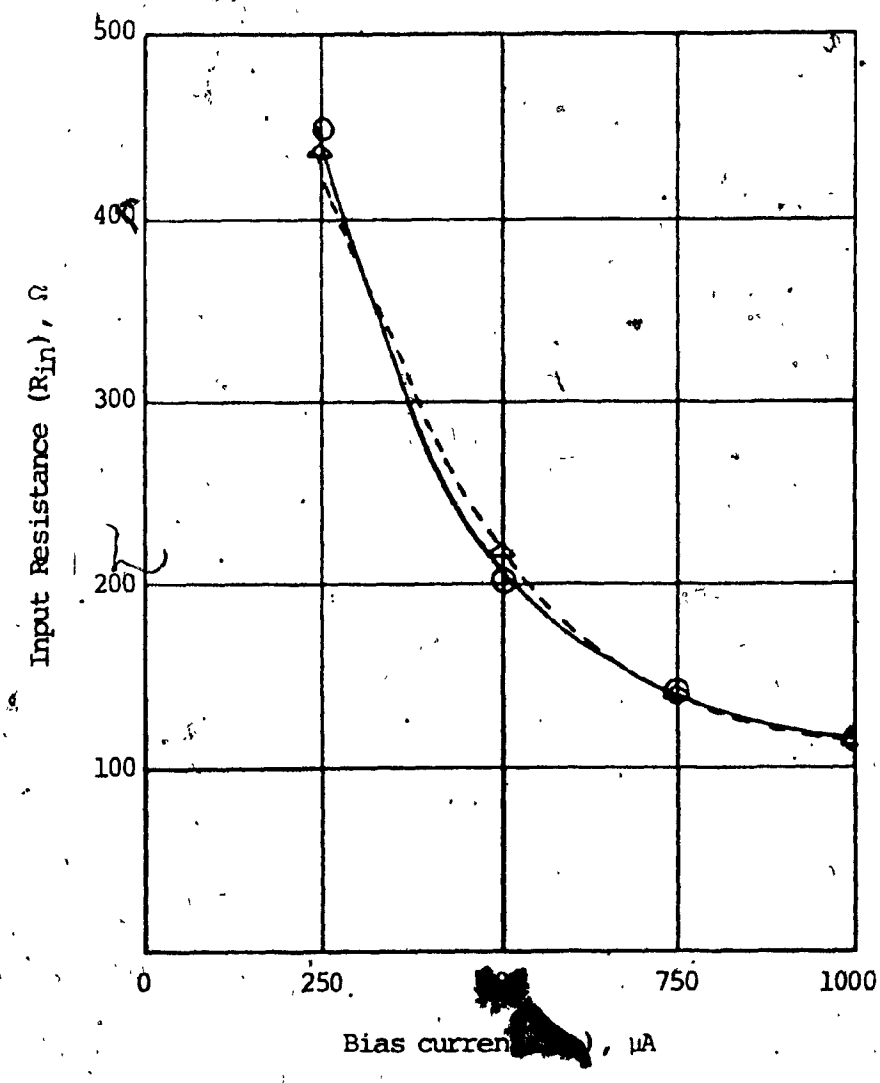

Figure 23.6 b: R_{in} versus I_2

measured R_{in} ————————

model R_{in} - - - - - - - - - -

Test conditions: I_1 = 250 μA
R_ℓ = 100Ω
V_i = 50 mV_{pp}

Tests were conducted at a frequency of 10 KHz. For the combination of I_1 = 250 μA, I_2 = 500 μA, R_ℓ = 100Ω, measurements were taken in the frequency range of 10 Hz to 100 KHz. R_{in} was found to be independent of the test frequency.

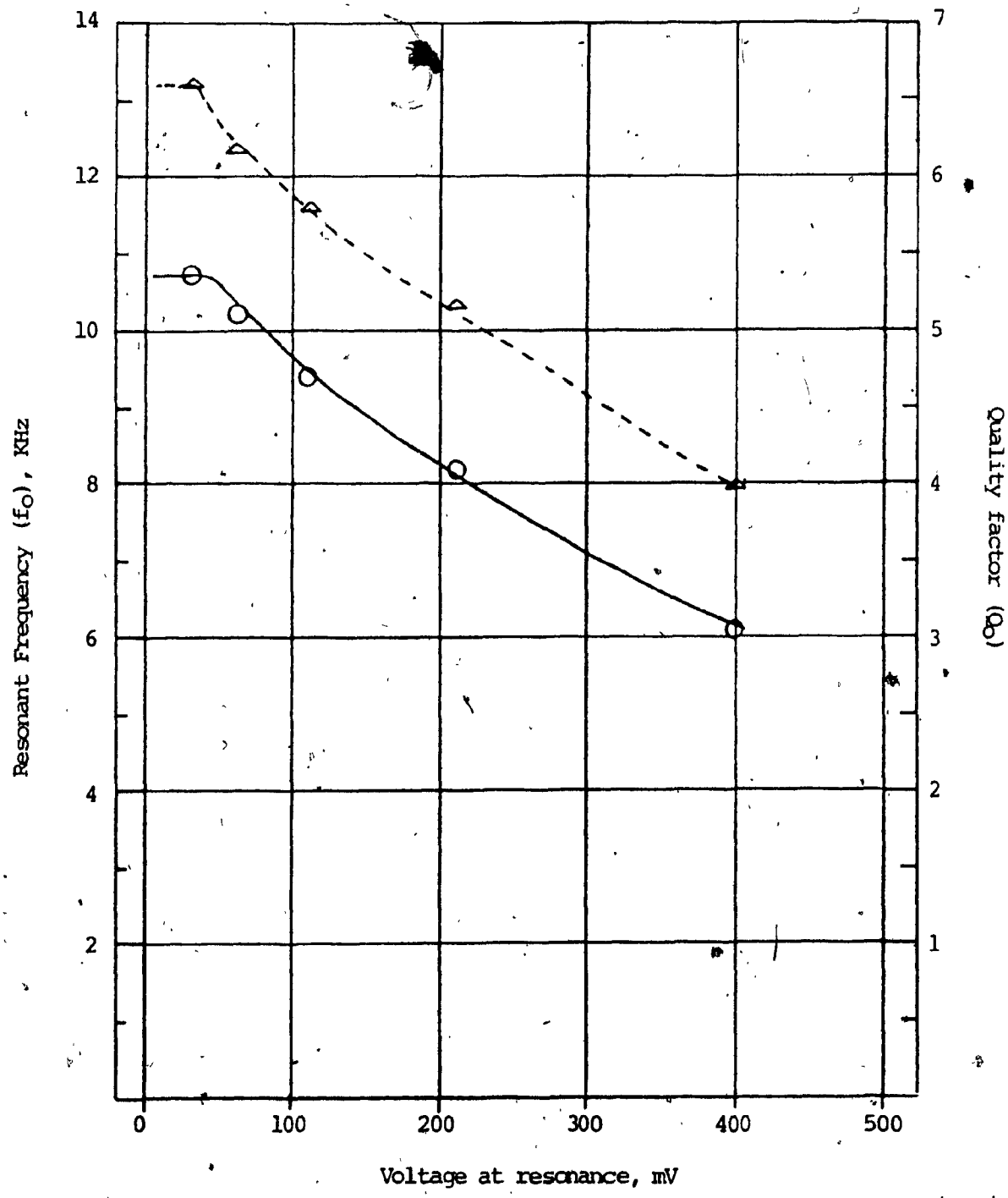

Figure 23.7: Simulated inductance in the non-linear region

measured f_o ————————

measured Q_o - - - - - - - - -

Test conditions: I_1 = 100 μA
I_2 = 500 μA
C = 0.1 μF
R_ℓ = 1 KΩ
C_T = 0.033 μF; D.F. = $5 \cdot 10^{-3}$

CHAPTER 4

A TECHNIQUE TO IMPROVE THE DYNAMIC RANGE OF THE OTA

4.1 General

In the previous chapter, the limitations imposed on the simulated inductance by the restricted dynamic ranges of the OTAs were pointed out. This chapter will present a new circuit configuration which increases the dynamic range of the OTA. Furthermore, an equivalent circuit for the inductor simulator circuit of chapter 3 employing this new configuration, is derived.

4.2 A VCCS with Extended Dynamic Range

Consider Fig. 24 shown below:

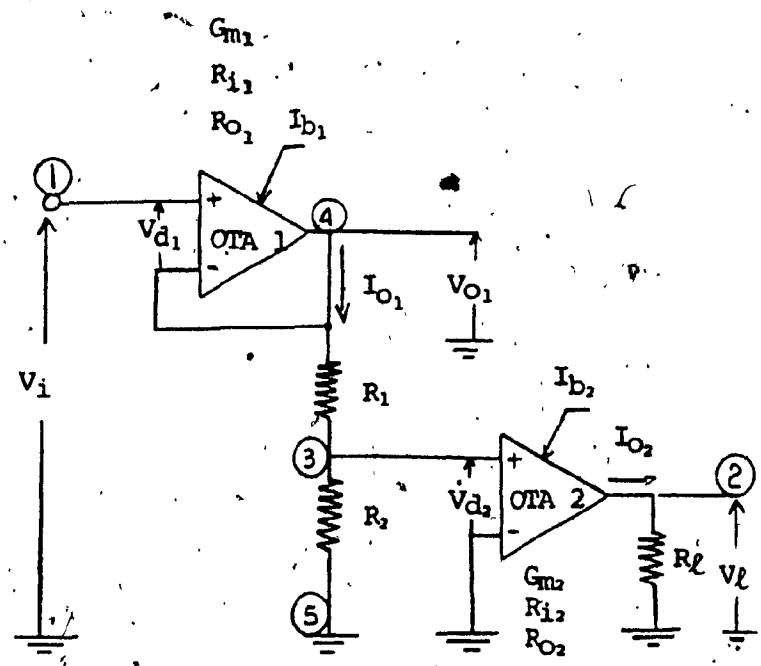

Figure 24: A new VCCS configuration

let $R = R_1 + R_2$

and, assume $R_{i_2} >> R_2$

$R_{i_1} >> R$

$$v_{0_1} = G_{m_1} R (v_i - v_{0_1}) \tag{4.1}$$

$$\text{Thus } v_{0_1} = v_i \left[\frac{G_{m_1} R}{1 + G_{m_1} R}\right] \tag{4.2}$$

$$v_{d_2} = v_i \left[\frac{G_{m_1} R}{1 + G_{m_1} R}\right] \frac{R_2}{R} \tag{4.3}$$

let $G_{m_1} R >> 1$

$$\text{and } \alpha = \frac{R_2}{R} \tag{4.4}$$

$$\text{Then: } v_{d_2} = \alpha v_i \tag{4.5}$$

$$v_{d_1} = v_i - v_{0_1} \tag{4.6}$$

Using 4.2 into 4.6, we obtain:

$$v_{d_1} = v_i \left[\frac{1}{1 + G_{m_1} R}\right] \tag{4.7}$$

$$\text{let } \beta = 1 + G_{m_1} R \tag{4.8}$$

$$\text{Therefore: } v_{d_1} = \frac{v_i}{\beta} \tag{4.9}$$

$$v_\ell = v_{d_2} G_{m_2} R_\ell \cong \alpha v_i G_{m_2} R_\ell \tag{4.10}$$

By designing a circuit with small values of α and large values of β, we can ensure that the linear input dynamic range of OTA 1 and OTA 2 are not exceeded. Thus the circuit configuration will act as a VCCS with a much larger dynamic range than the single OTA configuration.

Experimental measurements which were conducted on Fig. 24 are detailed in appendix VIII. Test results verified the correctness of the analysis which is outlined above.

4.3 Nodal Admittance Matrix of the New VCCS Configuration

A nodal admittance matrix for the new VCCS configuration shown in Fig. 24 can be obtained by writing the [5 x 5] augmented indefinite admittance matrix for nodes 1, 2, 3, 4, 5, grounding node 5 and eliminating nodes 3 and 4 by pivotal condensation. The resultant y parameters are:

$$y_{11} = \left[\frac{1}{R_{i_1}} - \frac{1}{y_{p_2}\,(R_{i_1})^2}\right] \tag{4.11}$$

$$y_{12} = 0 \tag{4.12}$$

$$y_{21} = -G_{m_2}\,\frac{1}{R_1 \cdot R_{i_1} \cdot y_{p_1} \cdot y_{p_2}} \tag{4.13}$$

$$y_{22} = \frac{1}{R_{0_2}} \tag{4.14}$$

where:

$$y_{p_1} = \left[\frac{1}{R_1} + \frac{1}{R_2} + \frac{1}{R_{i_2}}\right] \tag{4.15}$$

$$y_{p_2} = \left[\frac{1}{R_{i_1}} + \frac{1}{R_1} - \frac{1}{(R_1)^2\,y_{p_1}}\right] \tag{4.16}$$

Comparing the y parameters of the single OTA (Equation 3.4) with the y parameters of this new VCCS configuration, we can observe that:

(a) y_{12}, y_{22} are identical.

(b) y_{11} of the new configuration is given by y_{11} of the single OTA minus a constant.

(c) y_{21} of the new configuration is given by y_{21} of the single OTA divided by a constant.

4.4 An Inductance Simulator Circuit Using Four OTAs

Consider Fig. 25. This is an inductor simulator similar to the one studied in chapter 3, however, in this case, each OTA is replaced by the VCCS configuration presented in Fig. 24. Since the y parameters of the original OTA unit compared to the new two OTAs VCCS configuration differ only by a constant, we can conclude that its model circuit will be similar to the original model circuit derived in chapter 3 and presented in Fig. 20. However, the components values will change. Fig. 26, shows the model circuit for the configuration of Fig. 25. Parameters values are listed below.

R_{i_1}, R_{i_2}, R_{i_3}, R_{i_4} can be calculated from equation: 3.55

R_{0_1}, R_{0_2}, R_{0_3}, R_{0_4} can be calculated from equation: 3.57

G_{m_1}, G_{m_2}, G_{m_3}, G_{m_4} can be calculated from equation: 2.4

y_{p_1x} and y_{p_2x} can be obtained from 4.15 using R_{1x}, R_{2x}, R_{i_2}, R_{i_1}

y_{p_1y} and y_{p_2y} can be obtained from 4.15 using R_{1y}, R_{2y}, R_{i_4}, R_{i_3}

$$G_{m\,x} = G_{m_2} \frac{1}{R_{1x} \cdot R_{i_1} \cdot y_{p_1x} \cdot y_{p_2x}} \tag{4.17}$$

$$G_{m\,y} = G_{m_4} \frac{1}{R_{1y} \cdot R_{i_3} \cdot y_{p_1y} \cdot y_{p_2y}} \tag{4.18}$$

$$R_{i\,x} = \left[\frac{1}{R_{i_1}} - \frac{1}{y_{p_2x}\,(R_{i_1})^2}\right]^{-1} \tag{4.19}$$

$$R_{i\,y} = \left[\frac{1}{R_{i_3}} - \frac{1}{y_{p_2y}\,(R_{i_3})^2}\right]^{-1} \tag{4.20}$$

$$R_{0_x} = R_{0_2} \tag{4.21}$$

$$R_{0_y} = R_{0_4} \tag{4.22}$$

$$K_0 = \frac{1}{G_{m_x} \cdot G_{m_y}} \tag{4.23}$$

$$K_T = \frac{1}{K_1} + \frac{1}{K_2} \tag{4.24}$$

where:

$$K_1 = R_{0_x} \cdot G_{m_x} \cdot G_{m_y} \tag{4.25}$$

$$K_2 = R_{i_y} \cdot G_{m_x} \cdot G_{m_y} \tag{4.26}$$

$$R_A = R_{i_x} \tag{4.27}$$

$$R_B = R_{0_y} \tag{4.28}$$

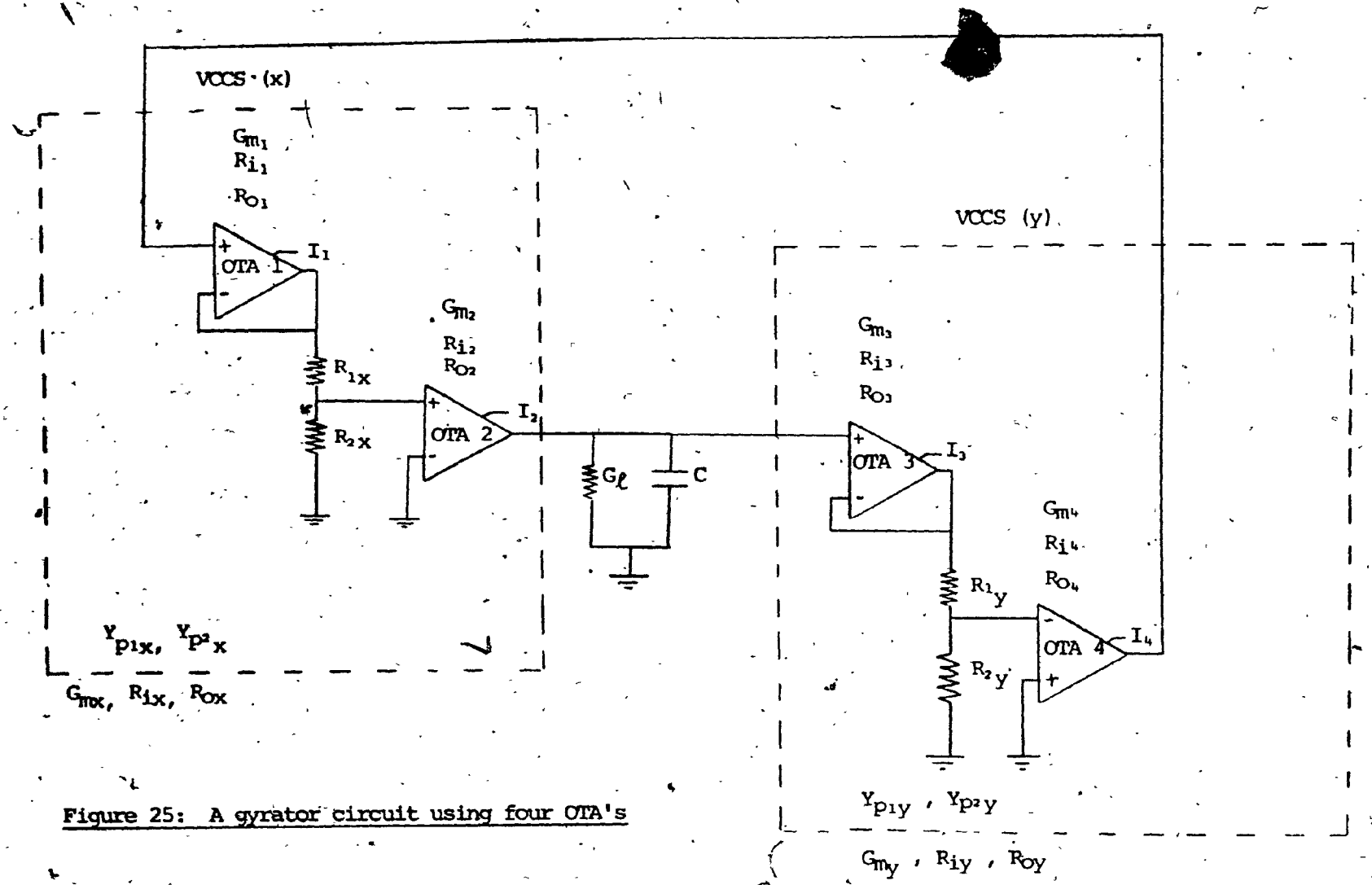

Figure 25: A gyrator circuit using four OTA's

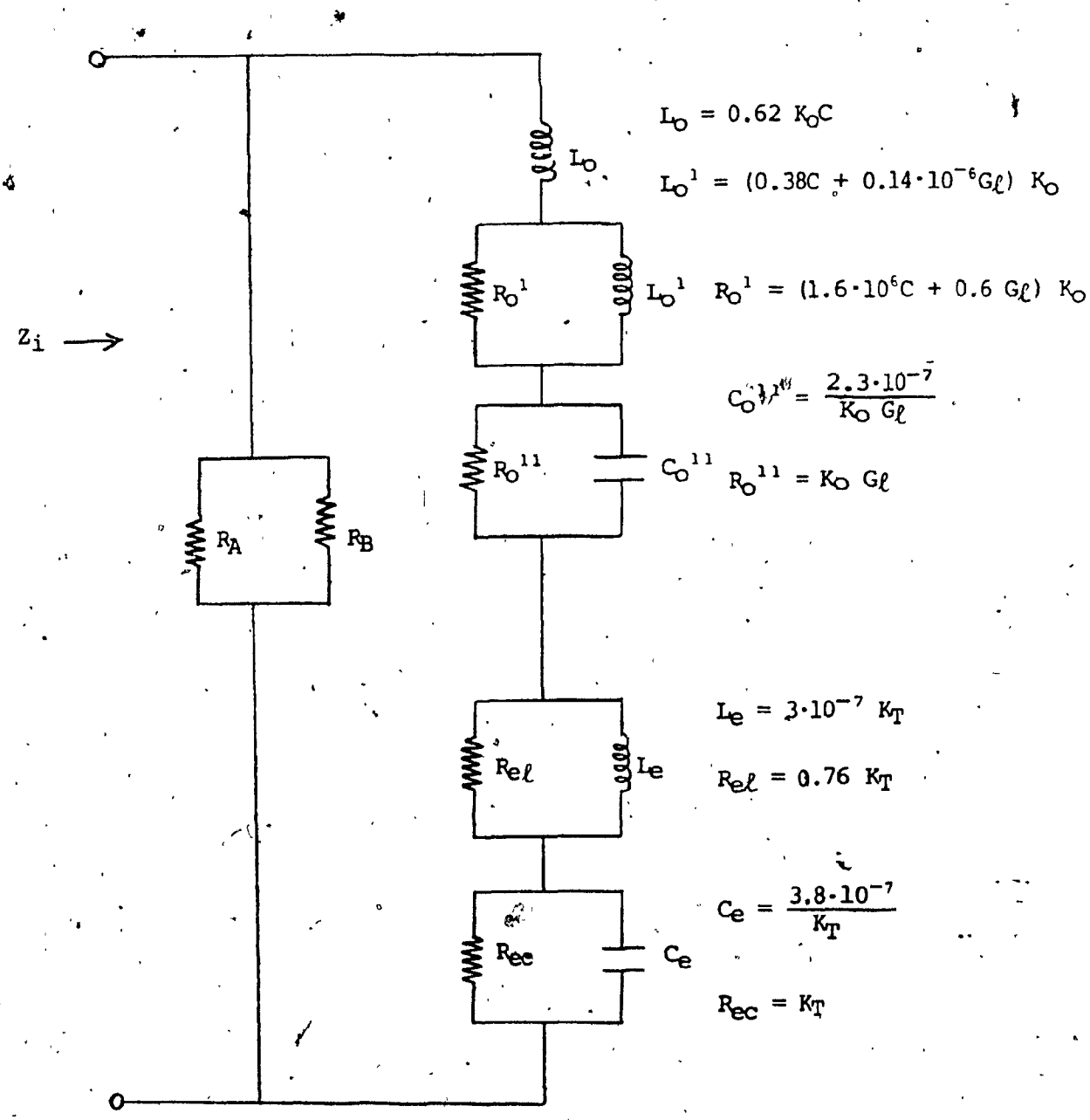

Figure 26: Model circuit for gyrator circuit of Figure 25

CHAPTER 5

SUGGESTIONS FOR FURTHER WORK AND CONCLUSION

5.1 Suggestions for Further Work

Chapter 4, has presented a new gyrator circuit which has the advantage of a much wider input dynamic range compared to the configuration studied in chapter 3. A feasibility study for this new gyrator circuit can be a subject for further studies. The major obstacles that the designer will face in this work can be predicted from the model circuit and the equations presented in section 4.2.3. There will be a decrease in the shunt equivalent resistence (equation 4.27 and 4.19) and an increase in the simulated inductance (equations 4.23, 4.17, 4.18). Further work could also be directed in investigating the feasibility of this configuration using the 3060 OTA and the feasibility of using the 3080 OTA in combination with the CA3046 transitor array as suggested by Kaplan and Wittlinger [6], in any of the two gyrator configurations which have been presented.

A gyrator circuit configuration using a single VCCS (hence, a single OTA unit) is presented in [11] and reported below in Fig. 27.

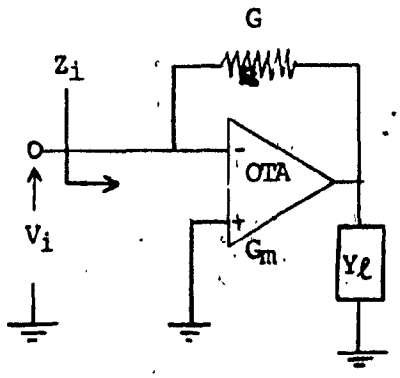

Figure 27: Impedance coverter circuit using a single OTA

assuming that the OTA has an infinite input and output impedance, we can derive:

$$Z_i = \frac{1}{G} \cdot \frac{G + Y_\ell}{G_m + Y_\ell} \tag{4.29}$$

If the inequalities $G << |y| << G_m$ are satisfied, then:

$$Z_i \simeq \frac{Y_\ell}{G \cdot G_m} \tag{4.30}$$

This configuration could also be a subject for further investigation.

Fugure designs could also consider increasing the input resistance of the OTA and its dynamic range by considering a hybrid OA/OTA configuration. The OA could be used as a unity gain buffer to replace OTA no. 1 in the circuit configuration shown in Fig. 24.

Improvements of the present work could also be a topic for further studies. We could attempt to derive frequency dependent models of the OTA by other methods and compare the accuracies of the different models thus obtained. Moreover, by adopting more sophisticated measuring instrumentation, we should be able to express the linear range in terms of the harmonic and intermodulation distortion percentages. Furthermore, we could attempt to obtain measurements relating the variation of the quality factor of the simulated inductance as a function of frequency. This type of data was difficult to obtain because of the limited dynamic range of the two OTA inductance simular circuit . A study of the simulated inductance performance with respect to temperature and supply voltage variations and a comparative study of the circuit with generalized impedance converter simulations such as Antoniou's [12] [18] [19] would also be desirable.

5.2 Conclusion

A series of experimental measurements in the open loop characteristics of the LM3080 OTA provided sufficient data to define the linear range of the OTA and to test the validity of the theoretical equations pertaining to its use as a VCCS with programmable transconductance. The dynamic range of the unit is ± 25 mV; however, if the choice of a bias current and load impedance is such that the output voltage reaches the value of the supply voltage before the output current reached the value of the bias current, then this dynamic range will be restricted.

Having defined the linear region, we proceeded to obtain, through experimental measurements, a frequency dependent model for the transconductance of the OTA. This model widens the horizon of the RC active filter designer by introducing a new active element (VCCS) with established frequency dependent characteristics. Due to this knowledge about the frequency dependent characteristics of the transfer gain of this OTA, the question of whether it could become a valid competitor to the OA in active filter design can now be more effectively tackled.

The model of the OTA was applied to investigate the feasibility of simulating a grounded inductance in a circuit configuration using two OTAs. An equivalent circuit for the two OTAs circuit was derived and experimentally tested. Model analysis and experimental results were found to be in close agreement. The investigation showed that inductances can be simulated over a wide range of values and over a wide frequency range. Simulated inductance values can be easily programmed through variations of bias currents. However, the practical range can be severely restricted by the limited dynamic range of the OTAs.

A new VCCS configuration using two OTAs was then presented. This configuration was theoretically and experimentally proved to extend the dynamic range of the single OTA. An equivalent circuit for the inductance simulator was also obtained using this new configuration. This equivalent circuit and a few other suggestions were presented as possible alternatives to the original inductance simulator circuit.

In conclusion, while it is obvious that further work on the subject is necessary, the author hopes that this study has triggered the interest of the reader and that his work may have contributed in a small way to increasing the wealth of human knowledge in electrical technology.

REFERENCES

[1] RCA Solid State, Corp., Linear Integrated Circuit, CA3060 and CA3080 files and Application Note ICAN-6668, (RCA, 1981).

[2] National Semiconductors, Corp., Linear Data Book, LM3080 file, (National Semiconductors, 1980).

[3] Deliyannis, T.: "Active RC Filters using an Operational Transconductance Amplifier and an Operational Amplifier", International Journal of Circuit Theory and Applications, Volume 8, January 1980, pp. 39-54.

[4] RCA Solid State, Corp., Linear INtegrated Circuits, file 537 (CA3060), figure 11, (RCA, 1981).

[5] Wheatley, C.F., and Wittlinger, H.A., "OTA obsoletes the Op Amp", Proceeding of the NEC, December 1969, pp. 152-157.

[6] Kaplan, L., and Wittlinger, H., An IC Operational Transconductance Amplifier with power capability", IEEE Trans. Broadcast and Television Receiver, BTR-18(3), August 1972, pp. 164-176.

[7] Miller, G.M., "Modern Electronic Communications", (Prentice-Hall, 1978), pp. 15-16.

[8] Dorf, R.C., "Modern Control Systems", (Addison-Wesley, 1967), p. 188.

[9] Valkenburg, M.E.V., "Introduction to Modern Network Synthesis", (John Wiley, 1960), chapter 8.

[10] Swamy, M.N.S., "Analysis of Linear Active and Passive Networks", Concordia University.

[11] Heinlein, W.E., and Holmes, W.H., "Active Filters for Integrated Circuits", (Prentice-Hall International, 1974), pp. 381-382.

[12] Antoniou, A., and Naidu, K.S., "Modelling of a Gyrator Circuit", IEEE Trans. Circuit Theory, volume CT-20, September 1973, pp. 533-540.

[13] Bhattacharyya, B.B., "Active Filters Design", Concordia University.

[14] Malvino, A.P., "Electronic Principles", (McGraw-Hill, 1973).

[15] Del Toro, V., "Principles of Electrical Engineering", (Prentice-Hall, 1965).

[16] Orchad, H.J., "Inductorless Filters", Electron. Letters, volume 2, 1966, pp. 224-225.

[17] Sharpe, G.E., "The pentode gyrator", IRE Trans., 1957, CT-4, pp. 321-323.

[18] Antoniou, A., "Realization of Gyrators using Operational Amplifiers and their use in RC-Active Network Synthesis", Proc. Inst. Elec. Eng., volume 116, November 1969, pp. 1838-1850.

[19] Antoniou, A., and Naidu, K.S., "A compensation technique for a Gyrator and its use in the design of a Channel-Bank Filter", IEEE Trans. Circuits and Systems, April 1975.

APPENDIX I

CIRCUIT DIAGRAM OF THE LM3080 OTA

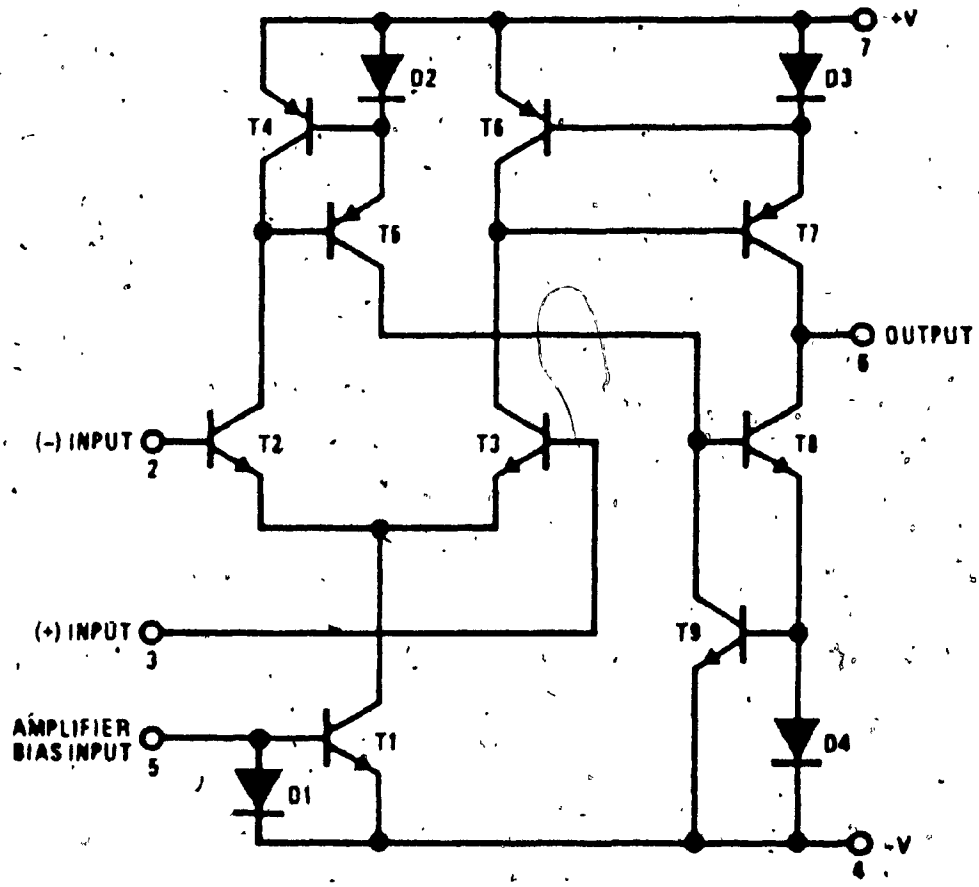

Dual-In-Line Package

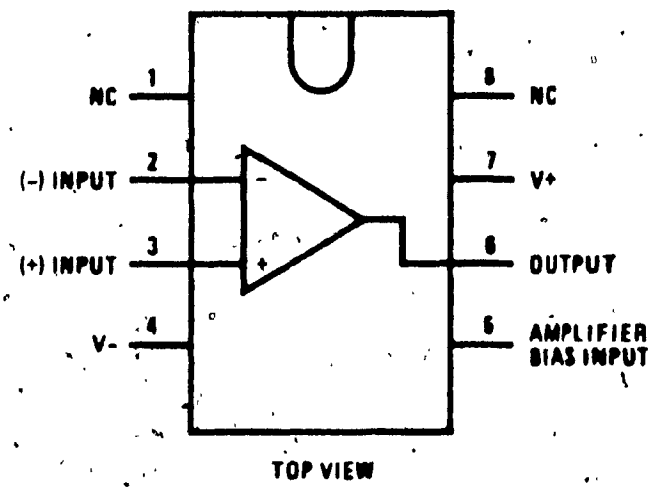

Figure A1.1: Schematic diagram of the LM3080 OTA

APPENDIX II

MEASUREMENT PROCEDURE UTILIZED TO OBTAIN DATA FOR FIG. 4, FIG. 6, FIG. 8 (CHAPTER 2)

Instrumentation

Ammeter: PM 2505 - Philips - (I_{abc} measurements)

Voltmeter: HP 3476A - Hewlett Packard (E_{in} measurements)

Power Supplies: LPD-422 FM - Lambda (V+, V-, Eb-)

Oscilloscope: PM 3226 - Philips (monitoring V+, V-, Eb-)

Probes: PM 8927, 10 M Ω 11 11 pF, 10:1

Oscilloscope: 7623A - Tektronics, equipped with the vertical module 7A26 and time base module 7853A

Probe: P6063B

1x, 1 M Ω, 105 pF

10x, 10 M Ω, 14 pF

Function generators: F34 - Interstate Electronics Corporation

HP 3312A - Hewlett Packard

HP - 8601A

Test Procedure

(1) Vary Eb- (or R_{abc}) until the ammeter reads the desired value of I_{abc}

(2) Ground the input of the OTA. Measure the output voltage. Annul this voltage by varying R_5.

(3) Ensure that V+ and V- have not changed; then, inject the desired input voltage.

(4) Measure the output voltage.

(5) Repeat steps 1 through 4 for each new value of I_{abc} and R_ℓ. Setting the bias current to values over 400 μA can be accomplished by grounding E_b and varying R_{abc}. Very small values of bias current

can be obtained by using large values of R_{abc} and moving E_b closer to -15 volts.

Practical Measurement Limitations

The maximum oscilloscope sensitivity is 5 mV/cm; thus, it is obvious that the data presented in Fig. 4.1a should be considered with a grain of salt. That is, output voltage readings of less than 0.5 mV corresponded to vertical deflections of less than 1 mm; therefore, it was impossible to obtain accurate readings in this range.

APPENDIX III

NOISE MEASUREMENTS

Noise was of highly random nature. The values of peak to peak average output noise which were taken on the circuit of Fig. 3 should be used only as a guideline to evaluate the test measurements accuracy presented in Fig. 4.1, Fig. 4.2, Fig. 4.3.

If more rigorous measurements of the rms intrinsic noise values are desired, the interested reader should consider using the "tangential method" technique described in reference [7].

Procedure Adopted for Noise Measurements

(a) Ground the input

(b) Set the desired value of I_{abc} using E_b or R_{abc}

(c) Use R_5 to zero the DC offset at the output of the OTA

(d) Measure the output average peak to peak noise level.

(e) Repeat (a) through (d) for each value while keeping the oscilloscope intensity unchanged from the setting which was used to obtain the data for Fig. 4.1, 4.2, 4.3.

Apparatus: see Appendix II

Data

I_{abc} →	1 μA	10 μA	100 μA	400 μA	600 μA	1000 μA
	V_0 (mV_{pp})	V_0 (mV_{pp})	V_0 (mV_{pp})	V_0 (mV_{pp})	V_0 (mV_{pp})	V_0 (mV_{pp})
R_ℓ						
1 K Ω	–	–	1	1.5	2	3
10 K Ω	–	1	10	12	15	17
100 K Ω	0.5	5	30	100	110	150

APPENDIX IV

MEASUREMENTS FOR $G_m(w)$

Basically the same apparatus presented in appendix II was utilized. In addition, the frequency counter: 5381A (Hewlett Packard) was employed to measure the input signal frequency. It was found that at high frequencies, the capacitative loading of this unit affected the magnitude of the input signal. Thus, the procedure used to avoid this loading effect consisted in measuring the frequency of the signal, hence, disconnecting the frequency counter from the circuit and then taking the input and output voltage readings with the counter removed from the circuit.

The Tektronics oscilloscope 7623A (vertical module: 7A26 and main time base module: 7A26) with probe P6063 in 10x position was employed to measure E_{in} and V_1. Phase shift between input and output was measured using the dual channel facility of the oscilloscope on CHOP (main was on magnitude x10).

The quoted capacitative loading of the P6063 is 14 pF; however, the exact capacitative loading which was experimentally calculated using an RC series circuit to be approximately 20 pF. Details of this measurement are given below.

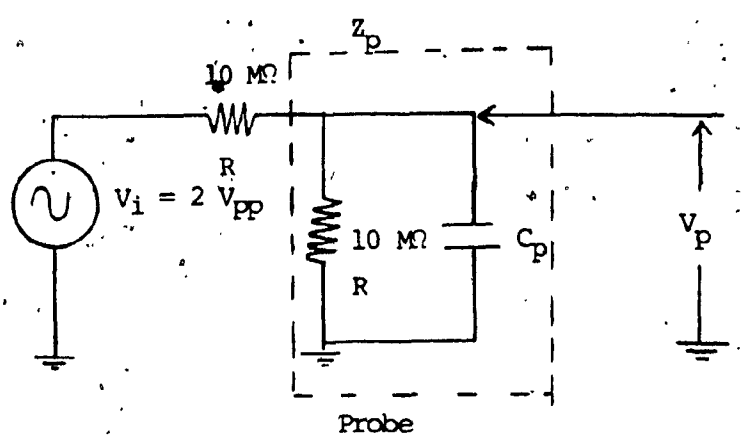

Figure A4.1: Probe capacitance measurement

From Fig. A2 we can write: $Z_p(s) = \dfrac{R}{1 + SC_pR}$

$$|Z_p(w)| = \frac{R}{[1 + (6.28)^2 f^2 C^2 R^2]^{\frac{1}{2}}}$$

at $f_1 = \dfrac{1}{2\pi RC_p}$, $|Z_p(w)| = \dfrac{R}{\sqrt{2}}$, $V_{p_1} = 0.828$ volts

at $f_2 = \dfrac{\sqrt{3}}{2\pi RC_p}$, $|Z_p(w)| = \dfrac{R}{2}$, $V_{p_2} = 0.666$ volts

Experimental measurements of f_1, f_2, V_{p_1}, V_{p_2} provided the data to calculate the value of C_p.

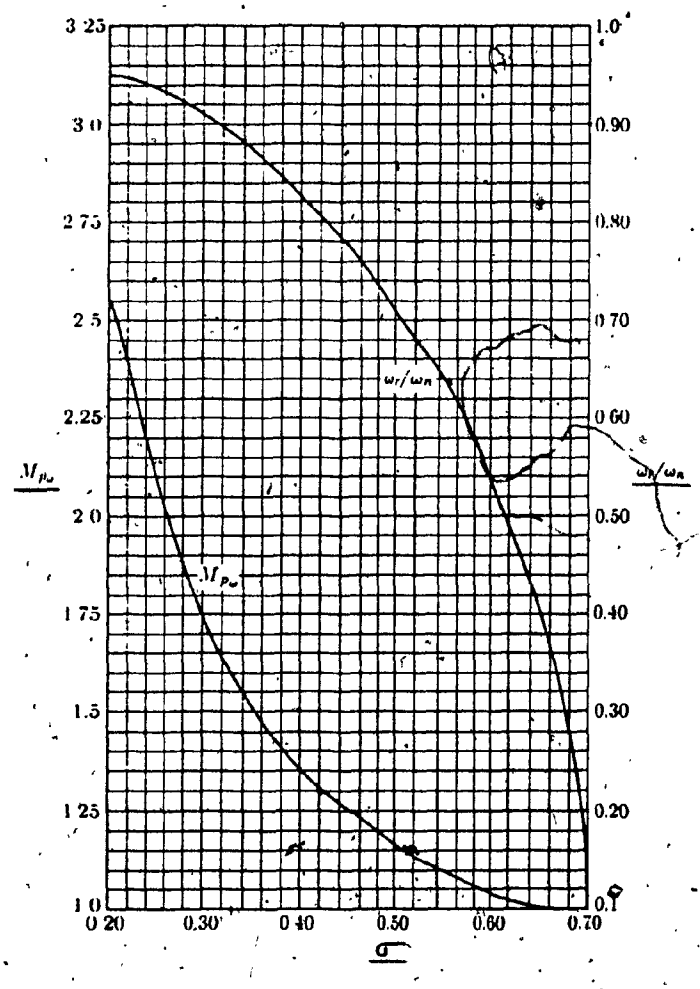

Figure A4.2: The maximum of the frequency response, M_{pw}, and the resonant frequency W_r, versus σ for a pair of complex poles [8]

APPENDIX V

COMPARISON OF THREE OTA UNITS

$R_\ell = 1\ K\ \Omega$, $I_{abc} = 400\ \mu A$, $E_{in} = \pm\ 25\ mV$

TABLE NO. 1

Frequency	Output Voltage Unit 1 mV_{pp}	Output Voltage Unit 2 mV_{pp}	Output Voltage Unit 3 mV_{pp}
10 Hz	360	360	360
100	"	"	"
1 KHz	"	"	"
10	"	"	"
100	"	"	"
250	"	"	"
500	400	400	420
750	480	480	500
1 MHz	560	540	570
1.25	590	560	600
1.5	600	550	590
1.75	550	500	540
2	480	450	470
2.25	425	390	400
2.5	360	360	360
2.75	330	320	320
3.0	280	280	280
3.23	254	255	260
3.5	240	235	235
3.75	230	210	200
4	200	190	190
5	150	130	130
6	110	100	100
7	85	80	75
8	70	65	65
9	60	55	50
10	47	48	45
11	40	40	40
12	30	30	35
13	25	25	25
14	20	20	20
15	10	10	10

TABLE NO. 2

Frequency	I/O Phase Shift Unit 1 degrees	I/O Phase Shift Unit 2 degrees	I/O Phase Shift Unit 3 degrees
10 Hz	0	0	0
100	0	0	0
1 KHz	0	0	0
10	0	0	0
100	0	0	0
250	0	0	0
500	0	0	0
750	4	7	6
1 MHz	14	14	13
1.25	32	36	32
1.5	48	52	52
1.75	61	63	65
2	75	76	79
2.25	80	80	80
2.5	89	90	90
2.75	100	100	100
3	108	106	105
3.23	114	110	110
3.5	117	118	116
3.75	120	123	120
4	122	128	126
5	127	134	134
6	144	145	144
7	148	150	148
8	160	156	153
9	168	160	160
10	176	176	177
11	180	178	180
12	180	180	180
13	180	180	180
14	180	180	180
15	180	180	180

APPENDIX VI

COMBINING AND SIMPLIFYING Z_{B_1} AND Z_{B_2}

The circuit shown below has the same configuration of Z_{B_1} and Z_{B_2}.

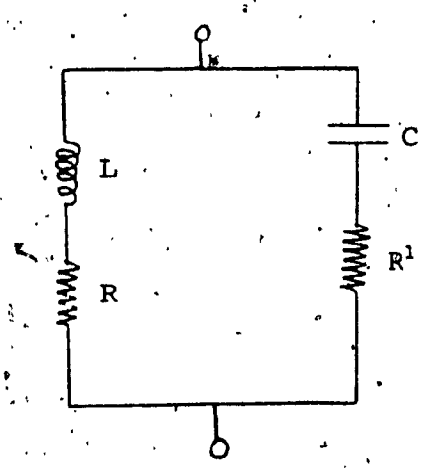

Figure A6.1: Configuration of Z_{B_1} and Z_{B_2}

Its input impedance Z(s) can be written as:

$$Z(s) = \frac{S^2\ (LR^1C) + S\ (L + RR^1C) + R}{S^2\ (LC) + S\ (RC + R_1C) + 1} = \frac{N(s)}{D(s)}$$

For the case of Z_{B_1} or Z_{B_2} (refer to Fig. 17), the components (L, C, R, R^1) can be written in terms of (σ, K_3 or K_2, W_n). Performing this substitution and considering that $W_n \gg w$, we obtain:

$$N(s) = S^2\ \frac{16\ \sigma^2}{K\ W_n^2} + S\ \frac{8\ \sigma}{K\ W_n} + \frac{1}{K} \simeq \frac{1}{K}\left[\frac{8\ \sigma\ S}{W_n} + 1\right]$$

$$D(s) = S^2 \frac{8\ \sigma}{W_n^2} + S\left[\frac{2 + 4\sigma}{W_n}\right] + 1 \simeq S\left[\frac{2 + 4\sigma}{W_n}\right] + 1$$

where K is equal to K_3 or K_2.

Using these two expressions for N(s) and D(s), we can write:

$$Z_{E(s)} = Z_{B_1(s)} + Z_{B_2(s)} = K_T \left[\frac{\frac{8\sigma S}{W_n} + 1}{\frac{S}{\phi}\left(\frac{2 + 4\sigma}{W_n}\right) + 1} \right]$$

where $K_T = \frac{1}{K_2} + \frac{1}{K_3}$

APPENDIX VII

MEASUREMENT PROCEDURE FOR TESTING THE INDUCTANCE SIMULATOR CIRCUIT

The basic inductor simulator circuit is shown in Fig. A7.1. Fig. A7.2 presents the symbolic representation of the basic circuit. Values for R_{X_1} and R_{X_2} were chosen to minimize the DC offset caused by the bias currents of the OTA. Nulling of any residual DC offset at the output of the OTAs was accomplished through R_{Y_1} and R_{Y_2}. Bias currents were set through a suitable selection of R_b and E_b combinations.

Instrumentation

HP3476A Multimeter - Hewlett Packard

Use: Monitoring DC offsets, measurements of R_1

PM2505 Multimeters - Philips

Use: Monitoring of bias currents

HP3312A function generator

Use: Generation of input voltage

7623A - Tektronics with 7A26 and 7853A modules and P6063B probe Oscilloscope

Use: Measurement of input and resonant voltage

HP4265B - Hewlett Packard - Universal Bridge

Use: Measurements of capacitances and dissipation factors

HP5381A - Hewlett Packard - Frequency Counter

Use: Measurement of resonant frequency

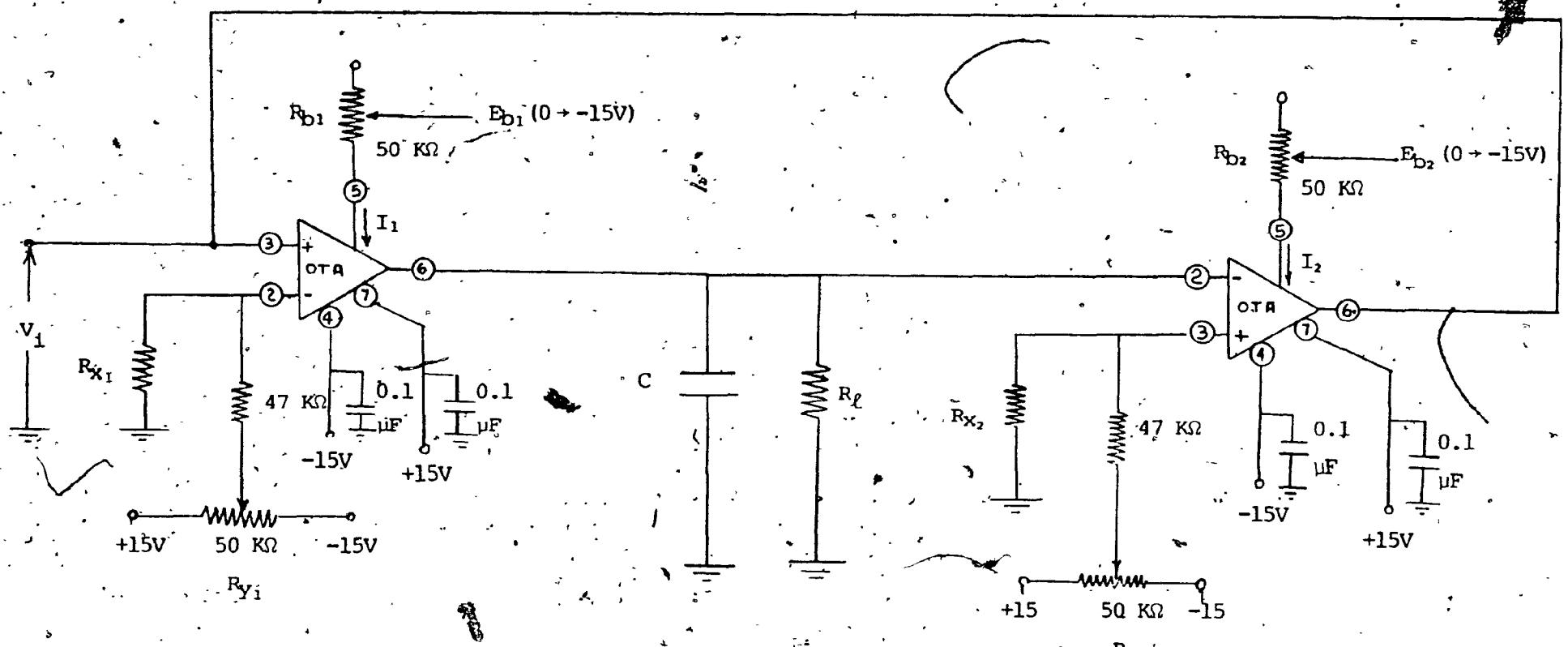

Figure A7.1: Inductance Simulator Circuit

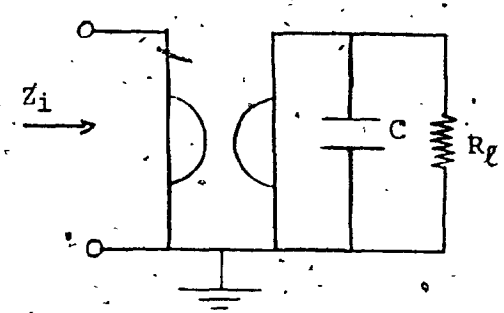

Figure A7.2: Symbolic representation of the inductance simulator circuit

Test no. 1: "L versus I_1"

The test circuit is shown in Fig. A7.3.

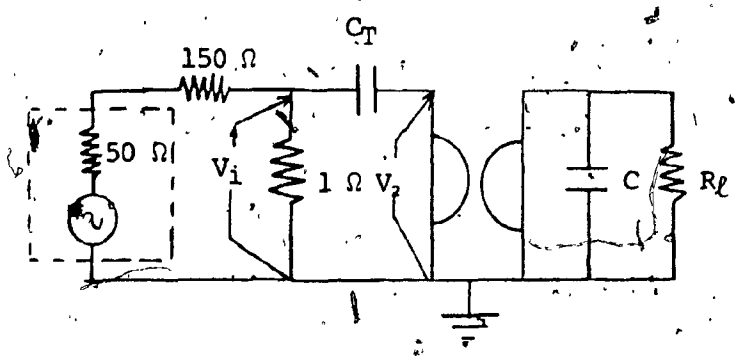

Figure A7.3: Test Circuit L versus I_1

Nominal components values/input voltage and bias currents.

$R_\ell = 100\ \Omega$

$C = 1\ \mu F$

$C_T = 0.033\ \mu F - I_1 = 100\ \mu A$

$= 0.068\ \mu F - I_1 = 200\ \mu A$

$= 0.15\ \mu F - I_1 = 400\ \mu A$

$V_1 = 10\ mV_{pp}, \quad I_2 = 500\ \mu A$

The parallel combination of the series (150 + 50) Ω resistances with the 1 Ω resistor presents a low impedance input into the series resonance circuit formed by C_T and the simulated inductor circuit.

Different values of C_T were used in order to generate resonant frequencies at approximately the same frequency ($f_0 \cong 3.8$ KHz) for different values of I_1.

Resonance was indicated by the peak value of V_2. The value of the resonant frequency was recorded.

R_ℓ was used to keep the Q of the circuit low in order to avoid non-linear operation of the circuit. Referring to Fig. 22, we observe that $R_p >> W_0L + R_s$; hence, the inductor simulator circuit is reduced to a series R_SL combination in series with C_T. We can calculate the measured simulated inductances from the relation:

$$L_{(meas.)} = \frac{1}{[2\pi f_{0(meas.)}]^2 C_T} \qquad \text{(A7.1)}$$

Components values were measured (C, C_T, R_ℓ) in order to take in consideration in the calculations of A7.1 the discrepancy between their actual and nominal values.

<u>Test no. 2</u>: <u>L versus I_2</u>

Procedure: similar to test no. 1; $f_0 \simeq 3.5$ KHz

Nominal components values/Input voltage and bias currents

$R_\ell = 100\ \Omega$

$C = 1\ \mu F$

$C_T = 0.033\ \mu F$ - $I_2 = 250\ \mu A$

$= 0.068\ \mu F$ - $I_2 = 500\ \mu A$

$= 0.15\ \mu F$ - $I_2 = 1000\ \mu A$

$V_1 = 10\ mV_{pp}$, $I_1 = 200\ \mu A$

Test no. 3: "L versus C"

Procedure: similar to test no. 1; f_0 was kept in the range 3.5 KHz to 10.5 KHz.

Nominal components values/Input voltages and bias currents

$R_\ell = 470\ \Omega$

$C_T = 0.033\ \mu F$

$C = 1\ \mu F$

$= 0.68\ \mu F$

$= 0.47\ \mu F$

$= 0.33\ \mu F$

$= 0.1\ \mu F$

$V_i = 5$ mV, $I_1 = 100\ \mu A$, $I_2 = 500\ \mu A$

Test no. 4: "L versus frequency"

The test circuit shown in Fig. A7.3 was used. Values of C_T and C were chosen in order to obtain resonance at different frequencies. Values for R_ℓ were chosen to keep the Q of the series circuit large enough to obtain measurable peak values of V_2 at resonance while at the same time allowing the circuit to operate within its linear region. The simulated inductance was calculated using equation A7.1. Variation of components values from nominal values were also taken in consideration. Bias currents were kept constant.

Nominal components values/Input voltages and bias currents

$C = 1\mu F$; $C_T = (47 \text{ to } 0.01)\ \mu F$; $R_\ell = 10\ K\ \Omega$ to $470\ \Omega$

$C = 0.33\ \mu F$; $C_T = (0.01)\ \mu F$; $R_\ell = 470\ \Omega$

$C = 0.1\ \mu F$; $C_T = (0.01 \text{ to } 0.022)\ \mu F$; $R_\ell = 470\ \Omega$

$C = 0.01\ \mu F$; $C_T = (0.1\ \mu F \text{ to } 470\ \mu F)$; $R_\ell = 2.7\ K\ \Omega$

$I_1 = 100\ \mu A$

$I_2 = 500\ \mu A$

$V_i = 5\ mV_{pp}$

Test no. 5: "Q versus R_ℓ"

The test circuit shown in Fig. A7.4 was used.

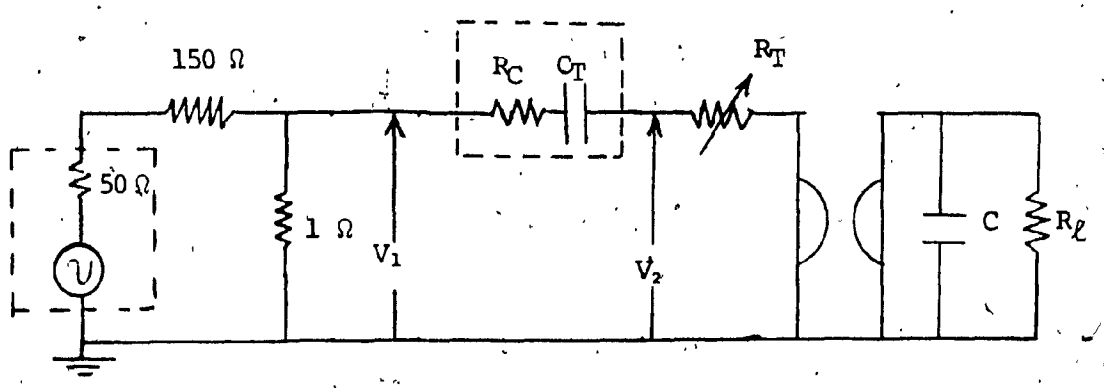

Figure A7.4: Test Circuit Q versus R_ℓ

Constant values for C, C_T, I_1 and I_2 were employed, thus the resonant frequency of the test circuit remained constant throughout the measurement. R_T was used to keep the voltage at V_2 within the linear dynamic range of the gyrator. Under the test conditions $R_p >> R_S + w_0 L$;

Hence, $$Q_{(model)} = \frac{W_{O(model)}\ L_{(model)}}{R_{S(model)}} \qquad \text{(A 7.2)}$$

$L_{(model)}$ and $R_{S(model)}$ can be obtained from Fig. 22; while, W_O can be calculated as follows:

$$W_{O(model)} = \frac{1}{\sqrt{L_{(model)}\ C_T}} \qquad \text{(A 7.3)}$$

At resonance,

$$\left|\frac{V_2}{V_1}\right| = \sqrt{\left(\frac{R_T + R_S}{R_T + R_S + R_C}\right)^2 + \left(\frac{W_O\ L}{R_T + R_S + R_C}\right)^2} \qquad \text{(A 7.4)}$$

Let Q_T be the quality factor of the test circuit:

$$Q_T = \frac{W_{O(meas.)}\ L_{(meas.)}}{(R_T + R_C + R_S)_{meas.}} \qquad \text{(A 7.5)}$$

R_C is the test capacitance resistance which can be obtained from the D.F. (dissipation factor) of the test capacitance: $R_C = D.F. / (2\ \pi\ f\ C_T)$.

$L_{(meas)}$ can be calculated as follows:

$$L_{(meas.)} = \frac{1}{[\ W_{O(meas.)}]^2\ C_T} \qquad \text{(A 7.6)}$$

Since $R_T + R_S \gg R_C$, from eq. (A 7.4) we can calculate Q_T from the measured values of V_2 and V_1 using the relation:

$$Q_T \cong \sqrt{\left|\frac{V_2}{V_1}\right|^2 - 1} \qquad \text{(A 7.7)}$$

From equation A7.5, we can obtain $R_{S(meas.)}$ as:

$$R_{S(meas.)} = \frac{W_{0(meas.)}\ L_{(meas.)}}{Q_T} - R_T - R_C \qquad (A7.8)$$

Thus, using A7.6 and A7.8, we can calculate the measured quality factor of the inductance simulator as:

$$Q_{(meas.)} = \frac{W_{0(meas.)}\ L_{(meas.)}}{R_{S(meas.)}} \qquad (A7.9)$$

Nominal components values/Input voltage and bias currents

R_ℓ = 100 Ω; 220 Ω; 470 Ω; 1 K Ω

C_T = 0.15 μF, D = $5 \cdot 10^{-3}$

V_i = 10 mV_{pp}; I_1 = 400 μA; I_2 = 500 μA

<u>Test no. 6a: R_{in} versus I_1</u>

The test circuit is shown in Fig. A7.5.

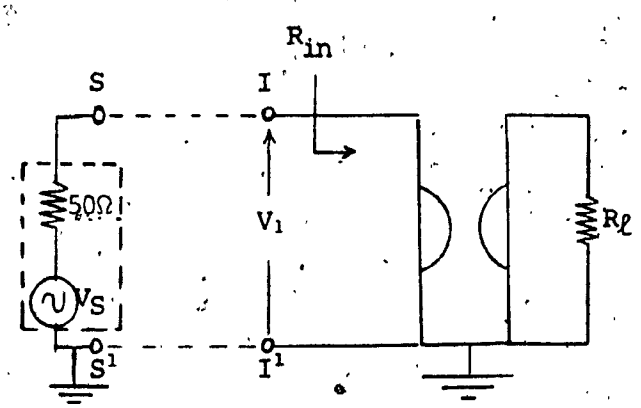

Figure A7.5: Test circuit R_{in} versus I_1

The bias current I_2 and the load resistor R_ℓ were kept constant throughout the measurements. When terminals S S^1 are connected with terminals 1, 1^1 we can write:

$$V_1 = V_S \left[\frac{R_{in(meas.)}}{R_{in(meas.)} + 50\ \Omega} \right] \qquad \text{(A7.10)}$$

V_S is the source voltage which is measurable between terminals S_1S^1 when these are disconnected from terminals 1, 1^1.

The 50 Ω resistor is the specified internal resistance of the function generator. This resistance value was also experimentally verified by measuring V_S; hence, terminating the generator with a precision 50 Ω resistor and noticing that the voltage between S S^1 had indeed dropped by one half of V_S.

V_1 is the voltage between terminals 1, 1^1 when these are connected to the voltage source.

Thus, by measuring V_1 for different values of I_1, and using equation A7.10, the measured values of R_{in} were obtained.

$$R_{in(model)} \simeq R_{S(model)} \qquad \text{(A7.11)}$$

<u>Test no. 6b: R_{in} versus I_2</u>

Procedure: similar to measurements for test no. 6a; however, this time I_1 was kept constant.

Nominal components values/Input voltage and bias currents

Test: 6a

$R_\ell = 100\ \Omega$, $I_1 = (100 \rightarrow 500)\ \mu A$

$V_i = 50\ mV_{pp}$, $I_2 = 500\ \mu A$

Test: 6b

$R_\ell = 100\ \Omega$, $I_2 = (250 \rightarrow 1000)\ \mu A$

$V_i = 50\ mV_{pp}$, $I_1 = 250\ \mu A$

Test no. 7: Circuit behaviour in the non-linear region

Test circuit: similar to Fig. A7.4, but with R_T shorted.

Constant values of bias currents (I_1, I_2), load capacitance (C), load resistance (R_ℓ), and test capacitance (C_T) were employed. The resonant frequency and the magnitude of the resonant voltage were recorded for various values of input voltages. $Q_{(meas.)}$ was obtained using the technique described in test no. 6.

Nominal components values/Input voltage and bias currents

$R_\ell = 1\ K\ \Omega$

$C = 0.1\ \mu F$

$C_T = 0.033\ \mu F$; $DF = 5.10^{-3}$

$V_i = (5 \text{ to } 100)\ mV_{pp}$; $I_1 = 100\ \mu A$; $I_2 = 500\ \mu A$

APPENDIX VIII

TEST MEASUREMENTS ON THE CIRCUIT CONFIGURATION OF FIG. NO. 24

The actual test circuit is shown in Fig. A8.1. The same instrumentation outlined in appendix VII was used. The 50 K Ω pot connected through the 47 K Ω resistor to pin 2 of OTA no. 2 was used to zero the DC offset across R_ℓ. It was not found necessary to employ any offsetting technique for OTA no. 1.

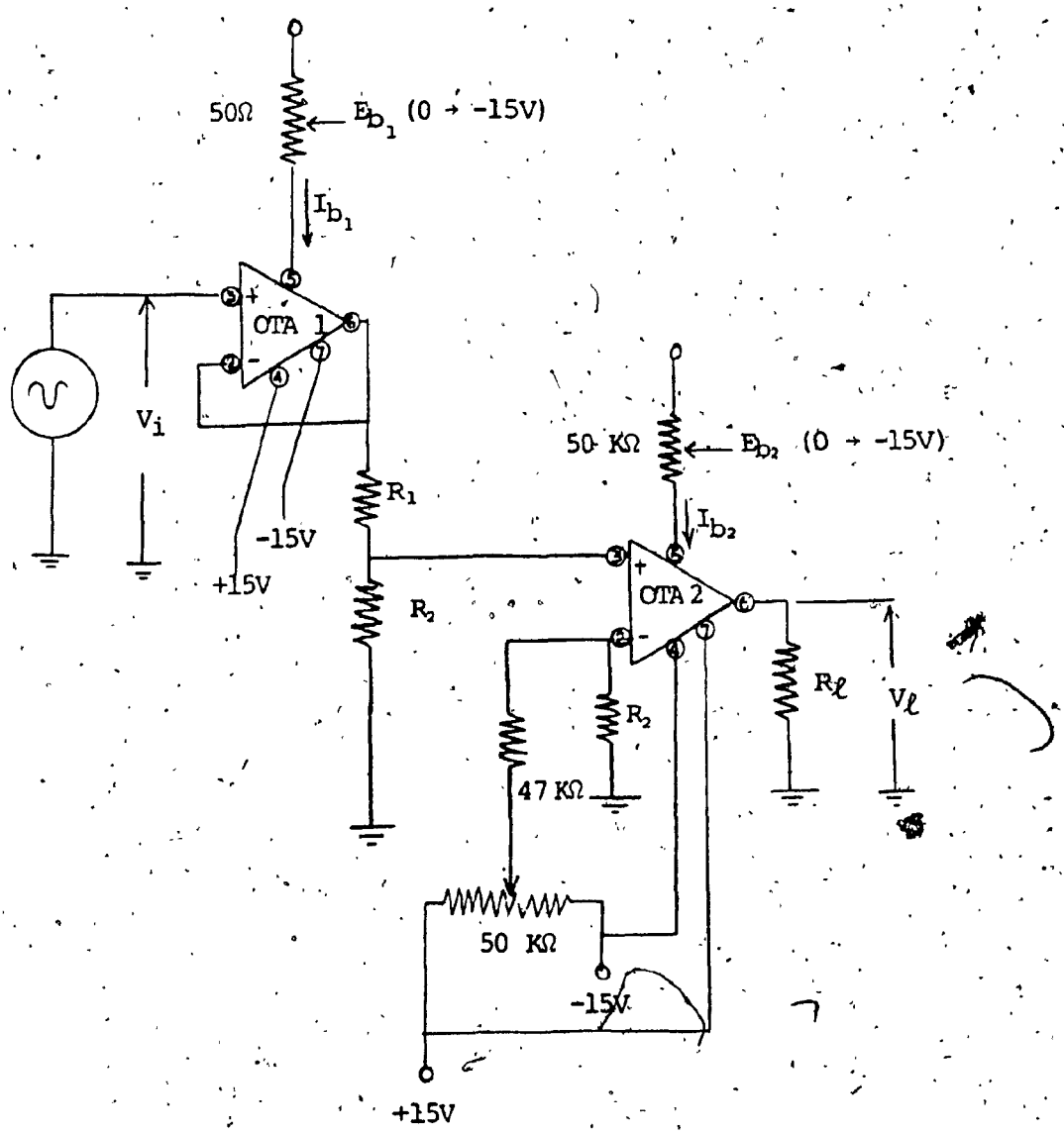

Figure A8.1: Test circuit. New VCCS configuration

Design for $v_i = 1\ V_{pp}$

From the analysis of chapter 2, we know that the maximum differential voltage for linear transconductance behaviour of the OTA is $50 \cdot 10^{-3}\ V_{pp}$.

Thus, for linear operation: $\beta \geq 20$ (from 4.9); and for a value of $I_1 = 500\ \mu A$, this value of β implies that: $R \geq 2000\ \Omega$ (from 4.8). Furthermore, from 4.4, for the condition $R = 2000\ \Omega$ and $I_1 = 500\ \mu A$, we obtain $R_2 \leq 100\ \Omega$.

A larger dynamic range will be obtained if $R > 2000\ \Omega$ or if $I_1 > 500\ \mu A$.

The results of the tests carried out on the circuit of Fig. A8.1 will now follow.

Test no. 1: "V_ℓ versus R_ℓ"

Test conditions:

$V_i = 0.5\ V_{pp}$

$I_{b_1} = 500\ \mu A$

$I_{b_2} = 100\ \mu A$

$R_1 = 2\ K\ \Omega$

$R_2 = 100\ \Omega$

$f = 1\ K\ Hz$

Test Results

R_ℓ (K Ω) (nominal)	V_1 (mV_{pp}) measured	V_1 (mV_{pp}) theoretical
1	45	45
5	190	208
10	440	450
50	2000	2120
100	4300	4500

Test no. 2: "V_ℓ versus I_{b_2}"

Test conditions:

$V_i = 0.5\ V_{pp}$

$I_b = 500\ \mu A$

$R_1 = 2\ K\ \Omega$

$R_2 = 100\ \Omega$

$R_\ell = 1\ K\ \Omega$

$f = 1\ KHz$

Test Results

I_{b_2} (μA)	V_ℓ (mV_{pp}) measured	V_ℓ (mV_{pp}) theoretical
10	5	4.5
100	45	45
200	90	99
400	170	180
600	250	270
800	330	360
1000	400	450

Test no. 3: "V_{0_2} versus R_2"

Test conditions:

$V_i = 0.5\ V_{pp}$

$I_{b_1} = 500\ \mu A$

$I_{b_2} = 100\ \mu A$

$R_1 = 2\ K\ \Omega$

$R_\ell = 10\ K\ \Omega$

$f = 1\ KHz$

Test Results

R_2 (Ω)	V_ℓ (mV_{pp}) measured	V_ℓ (mV_{pp}) theoretical
100	440	440
75	330	330
50	230	220
25	115	110
10	45	44

Test no. 4: "V_ℓ versus V_i"

Test conditions:

$I_{b_1} = 500\ \mu A$

$I_{b_2} = 100\ \mu A$

$R_1 = 2\ K\ \Omega$

$R_2 = 100\ \Omega$

$R_\ell = 10\ K\ \Omega$

Test Results

V_i (mV_{pp})	V_ℓ (mV_{pp}) measured	V_ℓ (mV_{pp}) expected	
100	88	88	
250	225	220	
500	440	440	
750	640	660	
1000	840	less than (880)	This is the expected non-linear range of the design
2000	1520	less than (1760)	
4000	1800	less than (3520)	

Test no. 5: Effect of I_{b_1} on linearity

Test conditions:

$V_i = 100\ mV_{pp}$

$I_{b_2} = 100\ \mu A$

$R_1 = 2\ K\ \Omega$

$R_2 = 100\ \Omega$

$R_\ell = 10\ K\ \Omega$

Test Results

I_{b_1} (μA)	V_ℓ (mV_{pp})	β
1000	90	38
750	90	29.5
500	90	20
250	90	10.5
100	87	4.8
10	50	1.38

Analysis:

Using 4.5, we have: $vd_2 = 4.7$ mV (within the linear range).

Using 4.9, we have: $vd_1 = \frac{100 \cdot 10^{-3}}{\beta}$. Thus for values of β less than 2, the circuit configuration will be in the non-linear region. Test results clearly confirm this expectation. In short, larger values of I_{b_1} tend to increase the dynamic range, whereas smaller values of I_{b_1} will tend to decrease it.